UNIVERSITÀ DEGLI STUDI FIRENZE

DOTTORATO DI RICERCA IN
SCIENZE CHIMICHE

CICLO XXIX

COORDINATORE Prof. PIERO BAGLIONI

MAGNETIC MOLECULES ON SURFACES: ASSEMBLING SINGLE MOLECULE MAGNETS AND MOLECULES WITH LONG SPIN COHERENCE

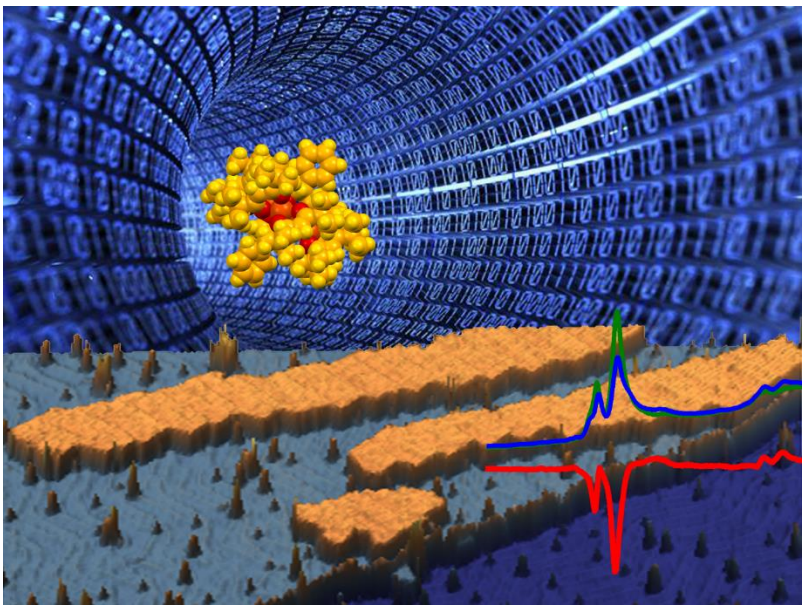

Dottorando
Dott. Irene Cimatti

Tutori
Dr. Matteo Mannini
Prof. Roberta Sessoli

UNIVERSITÀ
DEGLI STUDI
FIRENZE

DOTTORATO DI RICERCA IN SCIENZE CHIMICHE

CICLO XXIX

COORDINATORE Prof. PIERO BAGLIONI

MAGNETIC MOLECULES ON SURFACES: ASSEMBLING SINGLE MOLECULE MAGNETS AND MOLECULES WITH LONG SPIN COHERENCE

Settore Scientifico Disciplinare CHIM/03

Dottorando
Dott. Irene Cimatti

Tutori
Dr. Matteo Mannini

Prof. Roberta Sessoli

Coordinatore
Prof. Piero Baglioni

Anni 2013/2016

A mio nonno Eugenio

Summary

1 Introduction 1

2 Thermal deposition of Fe_4 SMMs 5

2.1 Introduction to the Fe_4 SMMs class 5

2.2 Evaporable Fe_4 SMMs 9

2.3 Study of Fe_4Ph films at sub-ML coverages 10

2.3.1 STM and XAS characterisation of sub-ML film of Fe_4Ph on Au(111) 10

2.3.2 Assembling Fe_4Ph molecules on surfaces with different reactivity .. 16

2.4 Deposition of $Fe(dpm)_3$ on gold: the study of a possible contaminant ... 21

2.4.1 UPS and XPS characterisation of $Fe(dpm)_3$ on gold 21

2.4.2 STM characterisation of $Fe(dpm)_3$ on gold 24

2.4.3 XAS characterisation of a drop-cast of $Fe(dpm)_3$ 27

2.5 Understanding the Fe_4 fragmentation: the back exposure experiment 28

2.6 Towards the study of the influence of dipolar field in Fe_4 SMM dynamics 33

2.6.1 STM and XPS characterisation of a submonolayer of Fe_4SMe 35

2.6.2 XAS characterisation of Fe_4SMe submonolayer film 38

3 Dy-based Single-Molecule Magnets 45

3.1 Introduction 45

3.2 Investigating the volatily of the $DyNOPyNO_2$ 46

3.2.1 Chemical characterisation of a thick film of $DyNOPyNO_2$ 47

3.2.2 Magnetic characterisation of bulk and film of $DyNOPyNO_2$ 52

3.3 Deposition on surface of a Dy-based single ion magnet 56

3.3.1 Investigating the volatility of $[Dy(tta)_3(L)]$ 57

3.3.2 Deposition of $[Dy(tta)_3(L)]$ from diluted solution 61

4 Assembling molecular qubit candidates on surface 67

4.1 Study of the processablity of $VO(dpm)_2$ 68

4.1.1 Deposition on Au(111) and *in situ* characterisation of $VO(dpm)_2$ 70

4.2 Towards the study of the quantum coherence at a single-molecule level 74
4.2.1 Characterisation of the graphene substrate 77
4.2.2 *In situ* characterisation of a submonolayer film of VOPc 79
4.2.3 STM and IETS characterisation of VOPc on graphene 82
5 Experimental methods 89
5.1 Standard magnetometry 89
5.1.1 *Ac* susceptibility 90
5.2 Photoelectron Spectroscopy 93
5.2.1 X-ray Photoelectron Spectroscopy 95
5.2.2 Ultraviolet photoelectron spectroscopy 97
5.3 Scanning Tunnelling Microscopy 98
5.3.1 Scanning Tunnelling Spectroscopy 100
5.4 Time of Flight Secondary Ion Mass Spectrometry 100
5.5 Use of synchrotron for the characterisation of magnetic molecules 101
5.6 Ultra-low temperature X-ray absorption end station 103
5.7 XAS characterisation 104
5.7.1 XMCD 105
5.7.2 XNLD 107
5.7.3 Measurements conditions 108
5.8 UHV platform 109
6 Conclusion 113
7 References 117

Abbreviation list

DFT	Density Functional Theory
DOS	Density Of State
IETS	Inelastic Electron Tunnelling Spectroscopy
LDOS	Local Density Of State
OMBE	Organic Molecular Beam Epitaxy
QCM	Quartz Microbalance
SMM	Single Molecule Magnet
STM	Scanning Tunnelling Microscopy
STS	Scanning Tunnelling Spectroscopy
TEY	Total Electron Yield
ToF-SIMS	Time of Flight Secondary Ion Mass Spectrometry
UHV	Ultra-High Vacuum
UPS	Ultraviolet Photoelectron Spectroscopy
XAS	X-ray Absorption Spectroscopy
XMCD	X-ray Magnetic Circular Dichroism
XNLD	X-ray Natural Linear Dichroism
XPS	X-ray Photoelectron Spectroscopy

1 Introduction

The use of magnetic molecules in molecular spintronics devices and as components of quantum computers are two challenging perspectives that nowadays are boosting the field of molecular magnetism.[1–7] Spintronics, or spin electronics, is an evolution of standard electronics that exploits spin properties instead of, or in addition to, charge degrees of freedom. *Molecular spintronics* is a field of research that combines the ideas and concepts developed in spintronics with the possibilities offered by molecules to perform electronic functions, to form self-organised nanostructures and to exhibit quantum effects.

Several studies have recently evidenced the interest in integrating Single Molecule Magnets in spintronics devices.[1,6,8,9] *Single Molecule Magnets* are metal complexes comprising one or more paramagnetic centres that at low temperature associate the magnetic bistability of classical magnets to the quantum properties of molecules.[10] The key ingredients of a SMM are the large spin and the large axial anisotropy. The SMM archetype is the Mn_{12} that has a large spin ground state of S = 10, given by the antiferromagnetic coupling of 8 Jahn-Teller distorted Mn^{3+} (providing the axial anisotropy to the molecule) and 4 Mn^{4+} ions. The effect of the magnetic anisotropy is the removal of the degeneracy of the (2S+1) states of the spin multiplet, even in absence of an external magnetic field, *i.e.* the Zero Field Splitting. This gives rise to the classical representation of the energy states of the SMM as two wells separated by the anisotropy barrier. Mn_{12} presents therefore magnetic bistability and slow relaxation of the magnetisation at cryogenic temperatures. The molecular nature of the magnetic bistability leads to observation of quantum effects in static and dynamic magnetic properties. In order to exploit this combination of molecular size with the properties of bulk material for applications, it is essential to control the magnetic state at the single molecule level, for instance in nanojunctions or by tunnel microscopies. This ambitious goal has motivated almost 15 years of essaying to transfer these molecules from the crystalline state to 2D environment.[4,11]

Initially, to follow this path the magnetism of hybrid surfaces containing Mn_{12} has been probed, unveiling a complex scenario. The Mn_{12} upon deposition on surface suffers of structural modifications that provokes the loss of the SMM behaviour.[12,13] These results evidenced that only a few of the known SMMs can be nanostructured, thus requiring a fine tuning of the SMM chemical structure and the selection of appropriate deposition methods in order to maintain the SMMs magnetic behaviour at the nanoscale.

Following this line, successful results have been obtained on a chemically grafted SMM containing four iron ions in the magnetic core, the Fe_4,[14,15] where the retention of the magnetic bistability has been demonstrated on a monolayer on

gold.[16,17] However, the deposition of an SMM by Self-Assembled Monolayer has some drawbacks: the grafting is restricted to some substrates and the technique does not allow a fine control of the molecular layer and of the surface quality. This last point hampers detailed investigations by Scanning Tunnelling Microscopy (STM) and Scanning Tunnelling Spectroscopy (STS), both techniques having revealed to be very informative in the characterisation of hybrid surfaces. A well-suited deposition technique for this type of investigations is the organic molecular beam epitaxy (OMBE) approaches. Also in this case, however, only few SMMs can be successfully employed. Part of this PhD thesis has actually been devoted to shed light on the thermal deposition in ultra high vacuum conditions of two volatile SMMs of the Fe_4 family.

Despite the positive results obtained, the exploitation of Fe_4 SMMs in spintronics devices remains rather challenging because of its very low energy barrier and the subkelvin temperatures required to observe the typical magnetic bistability. Another widely studied evaporable SMM is the bis(phthalocyaninato)terbium, $TbPc_2$,[18] because of its huge magnetic anisotropy associated to a very good stability of the system face to sublimation.[19,20] The $TbPc_2$ retains its magnetic bistability up to 8 K on surface, a great advantage with respect to the Fe_4 family that is bistable only below 1 K. However, the drawback is that the molecule is prone to strong hybridisation with metallic surfaces (the most commonly used substrates for UHV preparation protocols) leading to the disappearance of the SMMs behaviour.[21–23] Even if alternative decoupling strategies can be developed for stabilising or enhancing the SMM character of $TbPc_2$ on surface,[24–26] the community of molecular magnetism is always in search of new systems that preserve the bistability at the nanoscale. Recently new lanthanide-based SMMs were synthesised with appropriate chemical structure to promote the surface deposition.[27–29] In this PhD thesis we studied two different classes of Dy-based SMM systems evaluating the feasibility of their deposition on surfaces.

Together with the magnetic bistability, some magnetic molecules feature long coherence times that suggest the possibility of using them as *qubit* (quantum bit) for quantum computation. While in a classical system, a bit would to be in state $|0>$ or $|1>$, in quantum mechanics the qubit can be prepared in a superposition of both states, $|\varphi\rangle = \alpha|0\rangle + \beta|1\rangle$, a property that is fundamental to quantum computing.

Several systems have been explored as possible qubits, such as atomic ionic traps,[30] quantum dots in semiconductors,[31,32] photons,[33] and superconducting circuits.[34] Spins, either nuclear[35,36] or electronic,[37–39] are among the most efficiently addressable targets to build these logical units, as their initialization and read-out can be performed by well-established magnetic resonance techniques. In the search of new qubit *two key parameters* are the longitudinal relaxation time T_1, corresponding to the lifetime of a classical bit that can assume either |0> or the |1> value and the coherence time, T_2, the characteristic time in which the spin loses the memory of the phase of the superposition state in which it has been prepared. The ratio of T_2 over the time necessary for an individual quantum operation has to be larger than 10^4 to allow for

fault tolerant quantum computing. Moreover, the interaction of several qubits in order to have collective superposition state (entanglement) is essential for most quantum algorithms. Interactions with the environment tend however to provoke a shortening of the coherence time and need to be accurately controlled.

In the field of electron spin-based qubits nitrogen vacancies in diamond[40,41] and impurities in silicon and silicon carbide[42] exhibit long-lived quantum coherence but present major challenges in the control of their organization and coupling to perform quantum logic operations. Molecular spin based qubits, on the contrary, can be organised on surfaces and the interaction between them tuned at will through a rational synthetic design. Therefore, in the exploration of the long-lived molecular qubit, volatility of the complex is a key property we explored by studying two molecular qubit candidates based on the vanadyl (V=O) unit stabilised with specific ligands.

In this thesis, we present the study of the deposition on surface of three classes of magnetic molecules. **Chapter 2** is devoted to the investigation of hybrid surfaces containing Fe_4 SMM deposited by thermal sublimation in UHV. Two molecular systems have been investigated: Fe_4Ph and Fe_4SMe. A detailed Scanning Tunnelling Microscopy (STM) characterisation of monolayer and submonolayer of Fe_4Ph on gold single crystal has evidenced the presence of intact molecules together with smaller fragments, while the magnetic characterisation of the film carried out by X-ray Magnetic Circular Dichroism (XMCD) confirmed the successful retention of the bistability of the Fe_4Ph after the grafting. We will also highlight issues related to the reactivity of the Fe_4Ph with different substrates based on a combined STM and X-ray Photoelectron Spectroscopy (XPS) analysis supported by the Density Functional Theory (DFT) calculation that unravelled the chemical nature of the fragment observed on surfaces upon deposition of Fe_4Ph.

Chapter 3 is dedicated to test the deposition on surface of two SMMs based on dysprosium. The first compound we studied is a new dysprosium dimer. Time of Flight Secondary Ion Mass Spectrometry (ToF-SIMS) and XPS characterisations of a thick film of this compound demonstrated that the chemical structure of the complex is retained after the sublimation. Moreover, the *ac* susceptibility characterisation showed the magnetic bistability of the molecular film. A dysprosium monomer is the subject of the second part of this chapter. The Dy(III) derivative has been functionalised with sulphur-containing ligand to promote grafting on metallic substrates. We will show that this promising SMM unfortunately cannot be sublimated while wet chemistry protocols seems partially successful, preventing the complete fragmentation of the molecules and thus letting potential perspectives for the use of this system at the nanoscale.

Chapter 4 describes the assembling of molecules with long spin coherence time on different substrates. We will describe the assembling of $VO(dpm)_2$ system, a qubit candidate, on gold single crystal demonstrating the retention of the electronic structure after thermal deposition. In the second part of the chapter, we will describe analogously the deposition of VOPc, a more stable system, on a graphene substrate.

The final aim of this project is measuring the fingerprint of the $S = 1/2$ of individual molecules on this inert substrate using scanning inelastic electron tunnelling spectroscopy. This has been the subject of the last part of this PhD thesis that has been carried out at the Max Plank Institute of Hamburg.

The investigation of magnetic molecules at the nanoscale, indeed the object of this thesis work, has required the use of many different characterisation tools, including those based and synchrotron radiation, and a brief description of them is proposed in **Chapter 5**.

2 Thermal deposition of Fe4 SMMs

2.1 Introduction to the Fe_4 SMMs class

The tetranuclear iron (III) SMM, Fe_4 hereafter, was synthesised and characterised for the first time in 1999.[14] The Fe_4 family has since then been extensively studied, despite a blocking temperature below 1 K, because of its versatility in terms of chemical functionalization[43] as well as because of the stability of the *propeller-like* structure due to the four Fe^{3+} ions coupled by oxo bridges.[10]

The original system, the $Fe_4(OCH_3)_6(dpm)_6$ (where Hdpm = dipivaloylmethane) has a magnetic core where a central high spin Fe^{3+} ion is surrounded by three high spin Fe^{3+} ions (see Figure 2.1). Each peripheral iron is connected with the central one by two μ-methoxide ligand. The central Fe^{3+} ion is antiferromagnetically coupled with the external ones giving rise to a ground state multiplet with $S = 5$. The three peripheral metal ions coordinates two dpm^- ligands each one. The molecule presents a C_2 symmetry plane and the central and one of the peripheral ions sit on this plane.

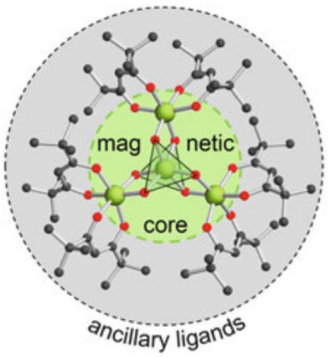

Figure 2.1 Structure of heteroleptic tetrametallic propellers viewed along the idealized threefold axis. Colour code: C= grey, O = red, Fe = green.[44]

The $Fe_4(OCH_3)_6(dpm)_6$ has a uniaxial magnetic anisotropy and the effect of this anisotropy on the spin states is the removal of their degeneracy even in absence of a magnetic field, affording the zero field splitting. This contribution is described in first approximation by the spin Hamiltonian:

$$\widehat{\mathcal{H}}_{zfs} = D\left[\hat{S}_z^2 - \frac{1}{3}S(S+1)\right] \qquad (1)$$

where D is the axial anisotropy factor, with a value of -0.21 cm^{-1} for the $Fe_4(OCH_3)_6(dpm)_6$, and $\hat{S}_z^2$ is the projection of the total spin operator along the easy axis. The effect of a negative D is that the system can be magnetised much more easily

when the field is applied along the principal, *i.e. z*, axis. The ground doublet of the molecule is characterised by $m_s = \pm 5$, where m_s are the eigenvalues of $\hat{S}_z^2$. The Hamiltonian of the system corresponds to two potential wells separated by an energy barrier, as illustrated in Figure 2.2.

The energy of the anisotropic barrier is defined as:

$$\Delta E = DS^2 \qquad (2)$$

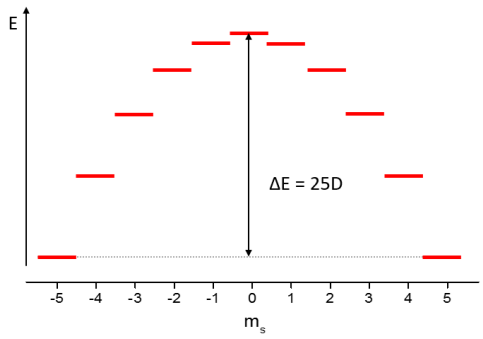

Figure 2.2 Energy level diagram in Zero Field of the S=5 state of Fe_4 reported as a function of the m_s states.

The dynamics of the magnetisation of such a system is expected, and experimentally found, to follow the Arrhenius law of a thermally activated process as the coupling with lattice vibrations, *i.e.* phonons, induces transitions among levels characterised by $\Delta m_s = \pm 1$ and ± 2.[45] If this multi-Orbach process takes place at moderate temperature, the very low temperature behaviour is characterised by under-barrier mechanisms that can be seen as a tunnelling process through the energy barrier.[46] They are originated by transverse terms in the spin Hamiltonian, either intrinsic of the system such as transverse magnetic anisotropy, or associated to external perturbations (external transverse magnetic fields, dipolar or hyperfine fields).

A peculiar feature of SMM is that the quantum nature of these objects and the under-barrier (tunnel) process of relaxation manifests itself in a classical property: the magnetic hysteresis loop. In fact, tunnelling is particularly efficient when level on opposite sides of the barrier generated by the magnetic anisotropy are at the same energy and are therefore more admixed by perturbing terms. Energy coincidence occurs at zero field and for other selected values of the longitudinal applied field:

$$H = n\frac{|D|}{g\mu_B} \qquad with\ n = 1,2,S \qquad (3)$$

where g is the gyromagnetic factor and μ_B is the Bohr magneton, giving rise to abrupt steps in the magnetisation when acceleration in the spin dynamics occurs. [10]

The *D* parameter of the Fe_4 SMMs can be modified by replacing the μ-methoxide ligands with the tripodal ligands H_3L (with L = R-C(CH_2OH)$_3$). Among this vast

number of heteroleptic systems with the formula $[Fe(L)_2(dpm)_6]$,[43,44,47] spectroscopic characterisations have shown that the *D* parameter varies in the range -0.41/-0.45 cm^{-1}, depending on the nature of R. The same trend is observed also for the anisotropy barrier. The different helical pitch and the more closely axial symmetry imposed by tripodal ligands are responsible of the improved magnetic bistability while the modification of the structure of R does not alter significantly the crystal packing of the complex, which is mainly influenced by the dpm^- ligands.

The stability in solution of the Fe_4 species with the tripodal ligand has also allowed to dilute this SMM in a diamagnetic crystalline matrix constituted by diamagnetic Ga_4 analogues. In Figure 2.3 the low temperature magnetic hysteresis of a single crystal comprising 1% of Fe_4 SMM clearly shows the steps originated by the resonant quantum tunnelling of the magnetisation, confirming the pure molecular origin of the phenomenon.

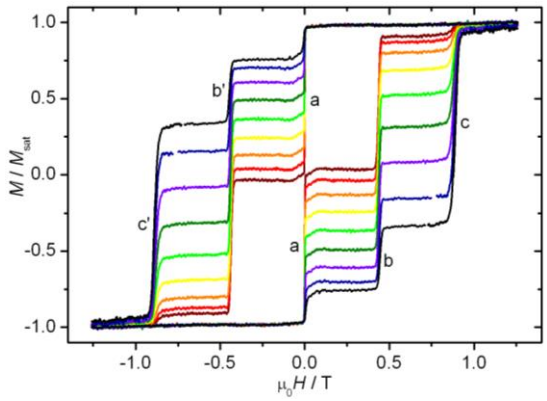

Figure 2.3 Hysteresis loop of a Fe_4 with a tripodal ligand diluted (1%) in a Ga_4 crystalline matrix recorded at 40 mK for different field sweep rates ranging from 1 (brown) to 280 (black) mT/s.[48]

More than fifteen complexes with different tripodal ligands have been synthesised and studied.[15,43,44,47] Among them, ligands made up of an aliphatic chain and terminated by a thio-acetyl group (named Fe_4C_9 and Fe_4C_5 depending on the length of the aliphatic chain)[15–17] result particularly relevant for the surface science field. The Fe_4 molecules containing these ligands can be chemisorbed on gold surfaces as monolayer deposits thanks to the great affinity of the sulphur moiety with gold. In the obtained film, an opening of the hysteresis at the nanoscale has been observed for the first time.[17] A reduction of the length of the aliphatic chain makes the molecules of the monolayer preferentially oriented with their easy axis of magnetisation out of the plane.[16] The magnetic characterisation of these Fe_4 monolayers (see Figure 2.4) has been possible by profiting of the extreme surface sensitivity of X-ray Absorption Spectroscopy carried out in TEY mode and operating with circularly polarised light under a strong magnetic field (see Paragraph 5.7). In these conditions, by applying a strong and variable magnetic field to the sample, it has possible[11] to measure the dichroism of the absorption and from this detect the magnetisation curves of the

monolayer sample as standard magnetometer techniques are not sensitive enough. This has provided the first demonstration that this technique is suitable to probe the magnetic behaviour of molecular systems at the nanoscale.

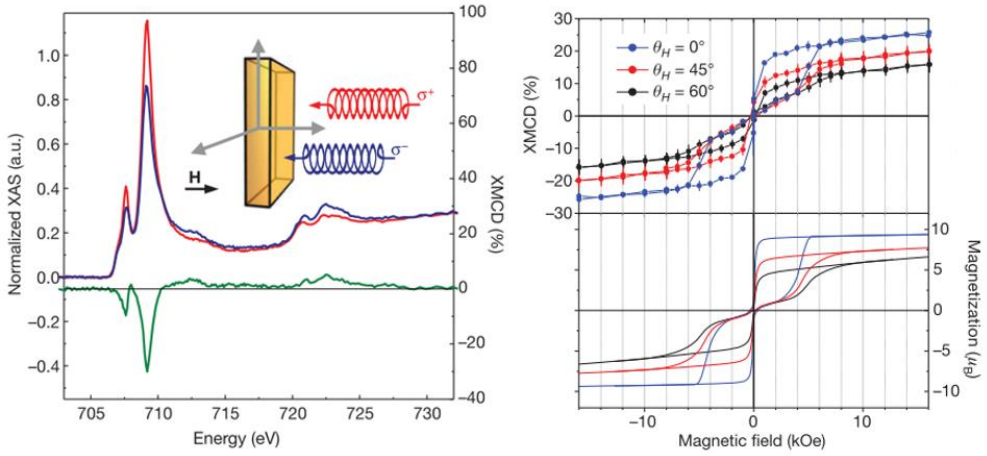

Figure 2.4 (Left) XAS and XMCD spectra of a monolayer of Fe_4C_5 on gold at the iron $L_{2,3}$ edges. (Right) Angle-resolved hysteresis loops for the Fe_4C_5 monolayer obtained from the XMCD at 709.2 eV and T = 650 mK. The experimental and calculated hysteresis loops are reported respectively in top and bottom part of Figure.[16]

These breaking findings turned a nightmare into a vision, to cite H. Wende, [49] giving the proof of concept that, after such discouraging studies on Mn_{12} on surfaces (see Chapter 1),[50,51] the SMMs can retain their properties on the surface and in particular at the monolayer scale.

Though extremely powerful, the use of XMCD to characterise a monolayer of molecules does not provide all the details that a study of a single crystal can provide. First of all, only relatively long relaxation times can be measured, thus requiring to reach very low temperatures for this class of SMM. This is particularly demanding in UHV conditions under a photon flux, providing also a large incertitude in the actual temperature of the investigated molecules. Nevertheless, hysteresis curves recorded by changing the angle of incidence of the photons and of the magnetic field have been particularly useful to evaluate the degree of orientation of the molecules in the film. To do that a numerical simulation of the hysteresis was performed, starting from the generally accepted assumption that the dynamics of the magnetisation of such a system follows a Markov process.[10] The time evolution of the population *p(t)* of each of the eleven states of the Fe_4 system can be described by the master equation:

$$\frac{d}{dt}p_p(t) = \sum_q [\gamma_q^p p_q(t) - \gamma_p^q p_p(t)] \qquad (4)$$

where γ_q^p is the probability of transition from the q state to the p state. With this approach the tunnelling mechanism is directly taken into account by the nature of $|\phi_p\rangle$ and $|\phi_q\rangle$ states which are no more pure eigenstates of S_z but rather a superposition of

them. Though many adjustable parameters need to be introduced, *i.e.* the spin-phonon coupling, higher order anisotropy terms leading the very low temperature behaviour, the angular dependence of the hysteresis resulted to be sensitive to geometrical factor, like the amplitude of the cone where the easy axis of Fe_4 molecules can reside, with respect to the normal to the plane. Figure 2.4 shows the simulated hysteresis curve obtained by calculating the population of all the $2S+1$ states at different fields and allowing at each field the population to relax according to equation 4. An acceptable agreement when the hysteresis is calculated as the sum of the contributions estimated for the molecular easy axis distributed within an angle of about 35° from the normal to the surface.

2.2 Evaporable Fe_4 SMMs

These pioneering studies based on the SAM approach did not allow for a wide flexibility in the choice of the substrate. Moreover, other techniques, such as organic molecular beam epitaxy (OMBE) performed in UHV, make possible to obtain a larger control on the molecular deposition. For these reasons, many efforts have been subsequently devoted to the synthesis of volatile analogues of $Fe_4(OCH_3)_6(dpm)_6$. In the Fe_4 family, the firstly introduced sublimable SMM is the $[Fe_4(L)_2(dpm)_6]$ (Fe_4Ph) where L = 2-hydroxymethyl-2-phenylpropane-1,3-diol which structure is illustrated in Figure 2.5.[43] The synthesis and the characterisation in bulk phase of this complex was reported Accorsi *et al*.[43]

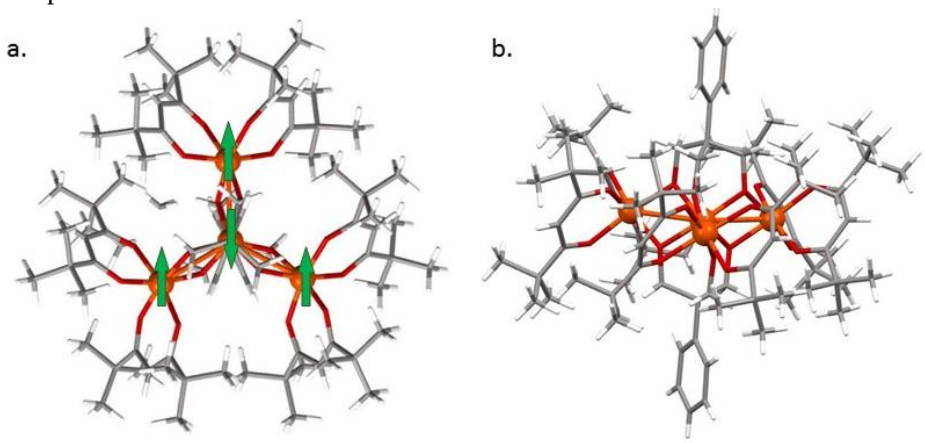

Figure 2.5 (a) Fe_4Ph molecular structure viewed along the idealized C_3 axis with arrows depicting the ferrimagnetic arrangement of the Fe^{3+} spins in the ground S = 5 state; (b) Fe_4Ph molecular structure viewed from the side; colour code: Fe = orange, O = red, C = grey, H = light grey.

The study of thick films of Fe_4Ph obtained by sublimation in High Vacuum was reported by Margheriti et al.[52] The ToF-SIMS characterisation proved the integrity of the molecule after the sublimation, while EPR and *ac* magnetometry studies

demonstrated that thick sublimated films of Fe_4Ph preserve the SMM behaviour of the molecular powders.

In order to investigate more deeply the system, the deposition at the monolayer and submonolayer level has been performed and illustrated in the following of this chapter. The *in situ* characterisation of the thin films by XPS, UPS and STM unveiled a complex scenario. With the support of the DFT calculation, we obtained a clear picture of the hybrid surface. Thanks to the experience acquired on the Fe_4Ph UHV deposition and characterisation, we decided to move to another sublimable tetranuclear iron (III), the $[Fe_4(L)_2(dpm)_6]$ where L = $H_3CS\text{-}C(CH_2OH)_3$ (Fe_4SMe). Since the STM characterisation shows that the molecules form a more ordered pattern on the substrate, the Fe_4SMe has been used to study the contribution of the dipolar field in the relaxation of the magnetisation of the Fe_4.

2.3 Study of Fe_4Ph films at sub-ML coverages

The first step of the study has been the deposition of monolayer and submonolayer coverages of Fe_4Ph on substrate with different reactivity, *i.e.* Au(111), Cu(100) and Cu_2N/Cu(100). An *in situ* STM characterisation of all these samples have been carried out using the CeTeCS platform described in Paragraph 5.8. Subsequently the slow relaxation of the magnetisation of the Fe_4Ph deposited on Au(111) have been evaluated by an XMCD carried out at the SIM beamline of the SLS synchrotron in Switzerland.

For all the experiments, a crystalline batch of freshly prepared Fe_4Ph has been degasses for two days at a temperature lower than the sublimation temperature, in order to eliminate possible volatile impurities. The Fe_4Ph powders sublimate in a temperature range from 480 to 510 K, depending on the experimental conditions. The synthesis of the Fe_4Ph crystals used in this thesis has been carried out in the lab of Prof. Andrea Cornia in the University of Modena and Reggio Emilia. Sublimation of the system has been carried out using a resistively heated quartz crucible in UHV ($P < 5 \times 10^{-9}$ mbar) with a K-thermocouple buried into the grinded molecular crystals. The nominal thickness of the molecular films has been measured by oscillating quartz microbalance. The Fe_4Ph molecules have been deposited on the freshly treated substrates (see below) held at room temperature, by using a deposition rate of about 0.04 ML/min.

2.3.1 STM and XAS characterisation of sub-ML film of Fe_4Ph on Au(111)

To investigate the Fe_4Ph growth process on the gold substrate at sub-ML coverages, an *in situ* STM study has been performed using the CeTeCS platform described in Section 5.8. Au(111) single crystals have been used as substrates for this first study. Before each preparation, the gold crystal has been freshly cleaned with

sputtering (2 μA, 1 keV) and annealing (720 K) treatments. The desired coverage of molecules has been estimated using QCM indications and than confirmed by STM. The scanning probe measurements has been performed cooling down the sample at 30 K. Low temperatures facilitate the imaging making the molecules less mobile on the surface. In fact, with respect to molecules such as phthalocyanines or $TbPc_2$, the imaging of Fe_4 is much more complex because of its three dimensionality, lower conductivity, and weaker interaction with the substrate.

A first sample featuring a coverage of 0.8 ML is discussed in the following. The wide-range image in Figure 2.6 shows a *quasi* layer-by-layer growth: a homogeneous first layer with few second-layer islands and hollows. The enlarged view in Figure 2.6 demonstrates that the round-objects are monodispersed. They have a lateral dimension of 1.63 ± 0.24 nm and form densely packed domains with hexagonal short-range order. The size (evaluated from a statistical analysis of Figure 2.6) results in good agreement with the DFT-based STM calculated image where *ca.* 1.8 nm[1] is found for the largest dimension (see Figure 2.8). The DFT-based simulations presented in this chapter are part of the PhD thesis of Dr. Silviya Ninova.[53] The interaction of Fe_4Ph with the Au(111) surface has been investigated by a periodic-DFT approach based on the rev-PBE functional[54] plus D3 dispersion corrections.[55]

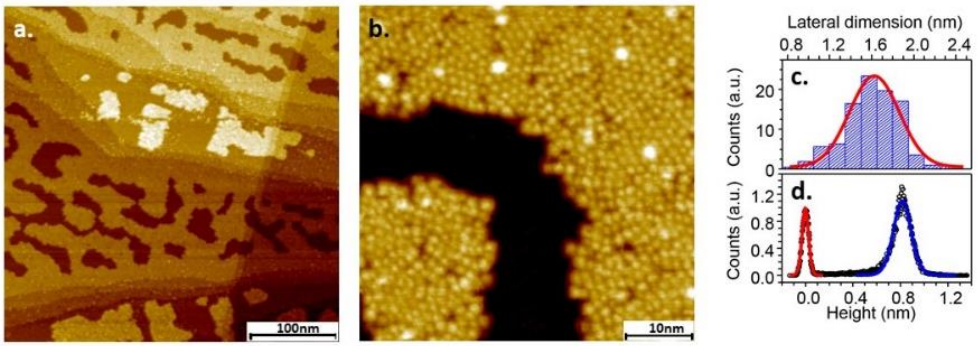

Figure 2.6. (a) STM image of Au(111) surface after sublimation of 0.8 ML of Fe_4Ph (389 × 389 nm^2, 10 pA, 3.5 V). (b) Enlarged view of the same surface (50 × 50 nm^2, 10 pA, 3.5 V). (c) Lateral size distribution of Fe_4Ph extracted from image (b) along with its Gaussian fit. (d) Height distribution in (b) with the red and blue Gaussian fits reproducing the height distribution of the substrate and of the Fe_4Ph layer, respectively.

Additional information can be extracted, neglecting the approximation due to the different conductivity of the molecular layer and the gold substrate, from the height distribution evidencing a Gaussian centred at 0.82 ± 0.12 nm, compatible with the height the Fe_4Ph molecules expected from the X-ray structure. Moreover, a second layer is also visible (0.96 ± 0.13 nm) in good agreement with the first layer. Objects observed in STM investigation are in line with shape and the dimension of the Fe_4Ph

[1] The dimension has been estimated as the largest intramolecular distance, corresponding to a pair of H atoms of the dpm^- ligands, increased by the corresponding Van der Waals radii.

simulated morphology represented in Figure 2.6. It has not been possible to reach a good resolution in the dark zone of the image, where the gold substrate is supposed to be, and in order to investigate deeply the system, a 0.2 ML coverage sample has been also studied.

The zoom in Figure 2.8 evidences a densely packed Fe_4Ph island. The lateral size of the spherical objects is 1.66 ± 0.20 nm, analogous to that obtained for the 0.8 ML coverage, confirming the common nature of the objects. In addition to the Fe_4Ph, B-domains with a height of 0.30 ± 0.05 nm are observed. Although the value is determined by STM and therefore convolved with density of states, suggests that they cannot be associated with Fe_4Ph molecules but rather with smaller units, either contaminants or fragments. The B-domains cover a significant portion of the substrate, probably part of the Fe_4Ph molecules lie on them. A demonstration is given by the height distribution of A domains that presents two peaks centred at 0.82 ± 0.11 and 1.05 ± 0.11 nm, respectively (Figure 2.8). The difference between the two is in line with the height of the fragments, confirming that a part of the intact molecule is in contact with the gold while a fraction of them is located on top of the B layer. Observing other areas of the sample, a similar height distribution have been observed with a ratio between the two components ranging from 1:4 to 1:1.

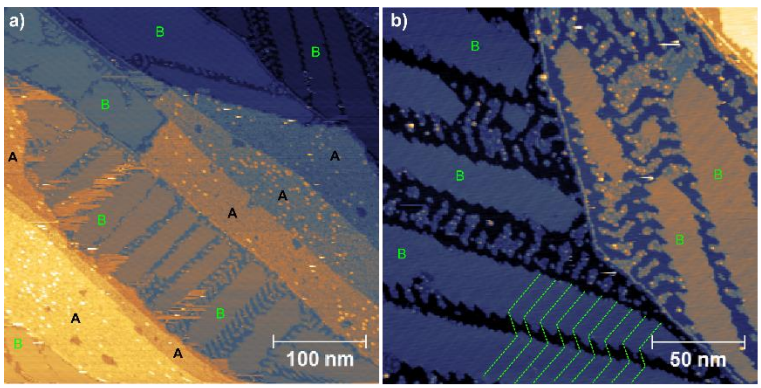

Figure 2.7 (a) STM image of sub-ML of Fe_4Ph sublimated on Au(111) (400 × 400 nm^2, 3 pA, 2 V). (b) Enlarged view of a region containing only B-domains (200 × 200 nm^2, 3 pA, 2.5 V).

In order to understand the nature of the B layer, it must be taken into account that the Fe_4Ph powders have been degassed for some days before the deposition, in order to eliminate volatile contaminants like Et_2O, the crystallisation solvent, or traces of free ligands. On the other hand, the Fe_4Ph has a sublimation temperature rather close to the decomposition one, so a partial decomposition cannot be excluded. Moreover, a decomposition can be favoured by the Au(111) reactive sites. In particular, in a previous study,[52] the $Fe(dpm)_3$ has been suggested as a possible contaminant in Fe_4Ph sublimated thick film.

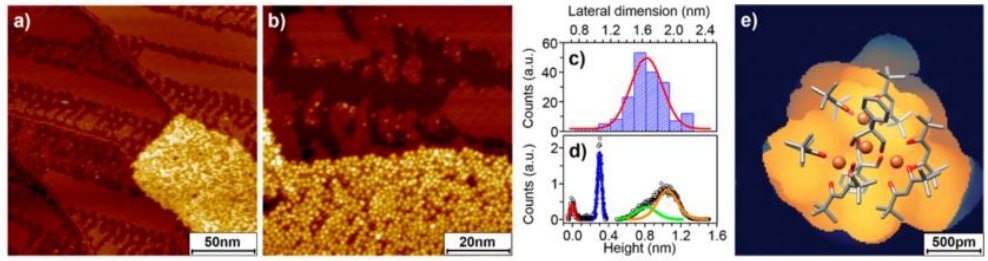

Figure 2.8 STM images acquired at 30 K for Fe_4Ph sublimated on Au(111) single crystal. (a) Large scale image of the 0.2 ML sample (135 × 135 nm^2, 3 pA, 2.5 V). (b) Same sample investigated at higher magnification (80 × 80 nm^2, 10 pA, 2.0 V). (c) Lateral size distribution of the Fe_4Ph molecules extracted from image (b) along with its Gaussian fit. (d) Height distribution in (b); the red and blue Gaussians reproduce the roughness of the bare gold surface and the height distribution of the contaminant domains, respectively; two Gaussian curves are used to reproduce the broad height distribution associated to the Fe_4Ph molecules (green and orange lines). (e) Calculated STM image of Fe_4Ph adsorbed on Au(111) at 2 V bias (occupied states), superimposed on the DFT-optimized structure.

Before studying in more detail the nature and origin of the B-domains, it is important to verify if the SMM behaviour of the Fe_4Ph is preserved after the thermal deposition. In order to check the magnetism of a sub-ML of SMMs, X-ray Absorption Spectroscopy study in TEY mode, similarly to those described in the previous section, have been performed on a setup dedicated to sub-Kelvin XMCD experiment, the Très Bas Température (TBT, see Section 5.6) end-station that was installed at the X11MA-SIM beamline of the Swiss Light Source (PSI, Switzerland).

This setup has been used for the experiments reported below using as substrate for the Fe_4Ph an *ex situ* flame annealed evaporated gold film on mica being the sputtering and annealing treatments not available on the cryomagnetic set-up. A sub-ML coverage sample of *ca.* 0.5 ML of the SMM has been sublimated *in situ*.[56] The estimation of the coverage has been obtained by a XAS calibration of the deposits based on the edge jump of the sample.[57] The edge jump is defined as the ratio between the intensity at the maximum of the iron L_3 edge with respect to the background and the intensity of the background (see Figure 2.10b). This value has been referred to the edge jump of chemical grafted dense monolayer of Fe_4C_9 (edge jump 13.6%). The sample measured at low temperature has been then prepared accordingly to this calibration (edge jump *ca.* 7%) in order to have a submonolayer coverage (about 0.5 ML). The XAS spectra at the Fe $L_{2,3}$ edges of this sample features the expected fine structure of the Fe_4 family with an L_3 structure characterised by two main contributions while the L_2 feature a very small contribution.[16,17,56] Moreover the amplitude and shape of the XMCD spectrum are similar to those found for the chemically grafted Fe_4C_5 and Fe_4C_9.[16,17] In particular, one can evidence, in agreement with earlier reports, a null dichroism in between the two main peaks of the L_3 edge as fingerprint of the intact Fe_4 magnetic core and a maximal intensity of the dichroism in that edge close to 40%.[58]

The magnetisation curve featuring at the base temperature (0.68 K) a broad hysteresis reported in Figure 2.10 has been obtained by monitoring the field dependence of the XMCD signal at the energy of its maximum absolute amplitude. The temperature dependence is in good agreement with previous study on Fe_4 molecules in bulk phase and as chemisorbed monolayers.[16,17,44,59]

At the lowest achievable temperature, the hysteresis loop has been recorded at two different orientations of the magnetic fields, $\theta = 0°$ and $\theta = 45°$, with respect to the normal at the surface, as illustrated in the scheme in Figure 2.10. The loop recorded at $\theta = 0°$ has the expected butterfly shape with a quantum tunnelling of the magnetisation (QTM) step at zero field and at ± 5 kOe. Since the QTM occurs when the longitudinal component of the field is $H = \pm|D|/g\mu_B$ (see equation 3),[60,61] the experimental values are in in good agreement with those expected when the magnetic field is applied along the easy axis (z), that is, $H = 0$ and $H = \pm|D|/g\mu_B = \pm 4.5$ kOe. Moreover, the energy of these steps is shifted to higher magnetic field for $\theta = 45°$ suggesting a preferential orientation of the molecule on the surface, in agreement with what has been found by Mannini *et al*.[16] Finally, the XMCD signal at $\theta = 0°$ levels off at low field, while a more gradual increase at higher fields is observed for $\theta = 45°$. The sublimated system therefore exhibits a behaviour similar to that previously found for the Fe_4C_5 derivative[16] and briefly described above. A preferential orientation of the molecules with their easy axis perpendicular to the surface seems to occur for Fe_4Ph in line with the *ab initio* calculations performed by Dr. S. Ninova.[53] Indeed, DFT calculations evaluated for the Fe_4Ph an angle of 34.4° with respect to the normal to the surface (see Figure 2.9), a similar value to that found for the sulphur-functionalized Fe_4 derivative.[16]

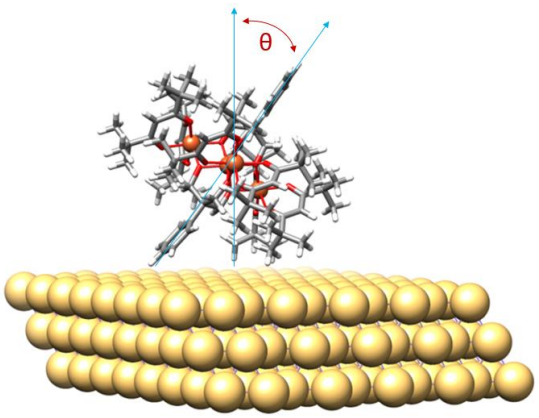

Figure 2.9. DFT optimized geometry of the Fe_4Ph molecules deposited on Au substrate, showing that the idealised C_3 axis forms an angle of ca. 35° with the normal to the surface. Colour code: Fe = orange, O = red, C = grey, H = light grey.

To confirm the dynamic nature of the magnetic hysteresis, a novel methodology developed in our research group and now widely used, based on following the time decay of the XMCD signal after a field change has been applied here (See Section

5.7.3). With respect to standard magnetometry, it must be taken into account that the decay of the remnant magnetisation (*i.e.* in zero applied field) cannot be directly measured in this system for two reasons. First, the Fe_4Ph has a very efficient quantum tunnelling at zero field, requiring very fast measurements and second, the TEY detection mode has a low signal to noise (S/N) ratio in zero applied field. So, we directly probed the time dependence of the magnetisation at 0.68 K by first magnetizing the system in a +16 kOe magnetic field, fast sweeping the field to −2.5 kOe and then monitoring the time evolution of the XMCD signal at 709.1 eV. This particular field was chosen as it lies in between the resonant QTM steps and consequently affords the slowest magnetic relaxation. The investigation has been carried out at both θ angles and the characteristic time of the decay, that is, 1400 ± 100 s and 1100 ± 100 s, for θ = 0° and θ = 45°, respectively, has been evaluated by a monoexponential fit to the experimental data.

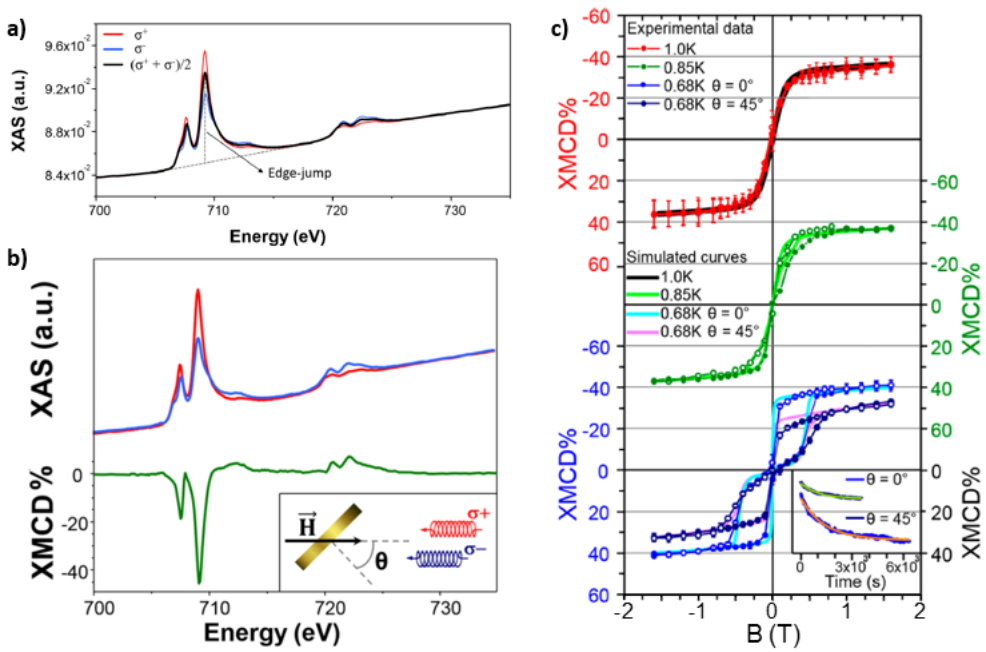

Figure 2.10 (a) XAS spectra at the Fe $L_{2,3}$ edges acquired for 0.5 ML of Fe_4Ph on Au/mica (0.68 K, 30 kOe field and θ = 0°). (b) XAS and XMCD% of a 0.5 ML sample of Fe_4Ph on gold on mica. (c) Magnetic hysteresis curves obtained by monitoring the field dependence of the XMCD signal at the energy of its maximum amplitude (709.1 eV). In the insert relaxation times at θ = 0° and θ = 45°.

The magnetic hysteresis loops have been simulated using the numerical approach previously described (Section 2.1) and again taking into account a preferential orientation of the molecular easy axis inside a cone of 35° from the normal to the surface. This XMCD-based magnetic characterisation demonstrates that the Fe_4Ph retains the slow relaxation of the magnetisation after the deposition on gold featuring alteration of this behaviour due to the peculiar arrangement of the molecules on the

specific surface we studied here. Both the bidimensional (2D) organization and the role of the substrate have been for these reasons studied more in detail by changing both the nature of the substrate as well as the structure of the molecules (influencing the packing on the surface) as well as the kind of substrate used for the deposition

2.3.2 Assembling Fe_4Ph molecules on surfaces with different reactivity

In the previous chapter, it has been demonstrated by the STM analysis that the submonolayer deposition of Fe_4Ph on Au(111) shows the presence of intact molecules, together with smaller units, named B-domains. In order to go a step forward in the investigation of the thermal deposition of the Fe_4Ph, we have deposited the molecules on other substrates with different reactivity, *i.e.* Cu(100) and Cu_2N growth *in situ* on Cu(100), and we have characterised these films by STM at 30 K.

Fe_4Ph on Cu(100)

Before the preparation of the sample, the copper has been freshly cleaned with sputtering (2 μA, 1 keV) and annealing (720 K). The STM characterisation of a submonolayer deposition of Fe_4Ph on Cu(100) is reported in Figure 2.11. In analogy with the deposition on Au(111), two different species can be detected and differentiated for their structure and height: islands of large spherical objects and flat smaller domains, now disposed in a dendritic fashion. The height analysis (Figure 2.11d) has been performed on the upper step region of Figure 2.11b. The flat layer shows a height of 0.18 ± 0.02 nm, *i.e.* lower with respect to the B-domains on the gold substrate.[62] The higher objects, attributed to Fe_4Ph, present a very broad distribution of heights between 0.7 and 1.1 nm, centred at 0.9 nm. We can assess that most of the Fe_4 molecules (height ≈ 0.7-0.8 nm) lay on the fragments (height ≈ 0.16 nm in this image), or on a bridge position on the B-holes. The lateral dimension has been measured to be 1.8 ± 0.2 nm, a value fully consistent with the Fe_4Ph on Au(111). The order in the Fe_4Ph-islands is significantly reduced, as a consequence of the expected lower molecular mobility on this surface, which seems to affect both Fe_4Ph molecules and smaller fragments.

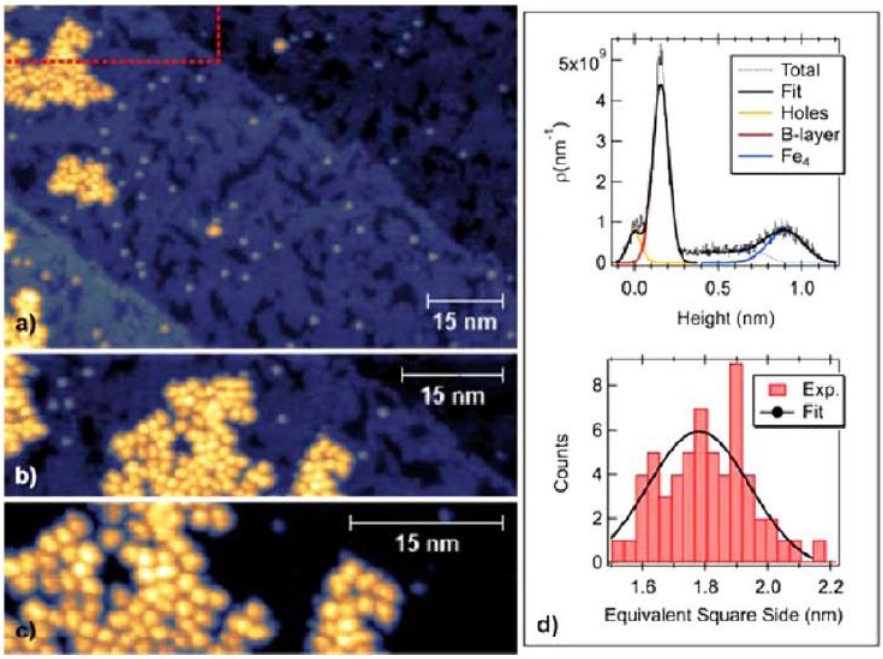

Figure 2.11 (Left) STM images acquired at 30 K of subML of Fe_4Ph sublimated on Cu(100) single crystal; I = 3pA, V = 2.1 V (a) 100 × 67 nm² (b) 75 × 21 nm² (c) 50 × 15 nm². (Right, top d) height distribution of the upper terrace of the (b) image with the fit. (Right, bottom d) lateral size distribution of Fe_4Ph in (c).

Fe_4Ph on Cu_2N

In order to avoid the presence of these domains of smaller species, attributed tentatively to strongly reactive fragments of Fe_4, we have also deposited the Fe_4Ph SMM on a semi-insulating layer of Cu_2N grown on the Cu substrate. This substrate is known to reduce the electronic coupling of atoms and molecules with the surface and for this reason it has been also used for several Scanning Tunnelling Spectroscopy and Inelastic Electron Scanning Tunnelling (IETS) experiments.[63–67]

A saturated Cu_2N layer has been prepared *in situ* on a Cu(100) single crystal. In a complete layer of Cu_2N, the nitrogen absorbed atoms occupy only half of the available hollow generating a $c(2\times2)$ reconstruction, as illustrated in Figure 2.12. This figure displays the modification of the Cu(100) substrate for growing N-coverage. A 0.2 ML N-coverage shows N-containing square islands disposed along [001] and [010] directions. The subsequent image, corresponding to an N coverage of around 0.3 ML, displays islands organised in a grid-like array. The saturation coverage (0.5 ML) image (Figure 2.12d) presents a continuous N-containing layer with trenches along the [110] directions. This coverage has been obtained by nitrogen bombardment of the Cu(100) at room temperature for 10 min (E = 1 keV, P_{N2}= 2 x 10^{-6} mbar) and subsequent annealing up to 600 K. The growth of Cu_2N on Cu(100) is self-limited to

one monolayer. The substrate used for the molecular deposition on the decoupling layer is a saturated coverage of Cu_2N.

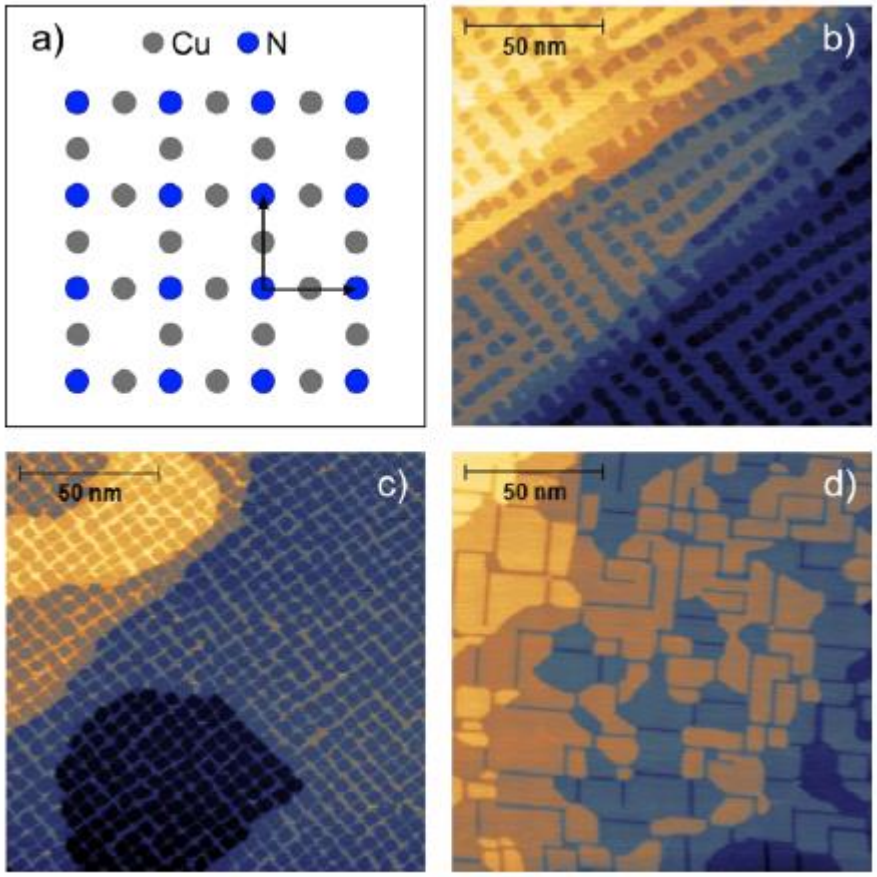

Figure 2.12 (a) a scheme of Cu_2N c(2x2) reconstruction. The arrows indicates the unit cell vectors. (b-d) 150 × 150 nm^2 STM images of growing doses of N_2 on a Cu(100) single crystal. (b) θ_N = 0.2 ML, V = 2 V, I = 200 pA. (c) θ_N = 0.3 ML, V = 1.5 V, I = 400 pA. (d) θ_N = 0.5 ML, V = 0.8 V, I = 600 pA.

The STM image of a sub-ML of Fe_4Ph on Cu_2N (Figure 2.13), shows that the decoupling layer does not prevent the presence of the lower domains. Nevertheless the trench like Cu_2N reconstruction hampers the formation of large islands of these fragments.

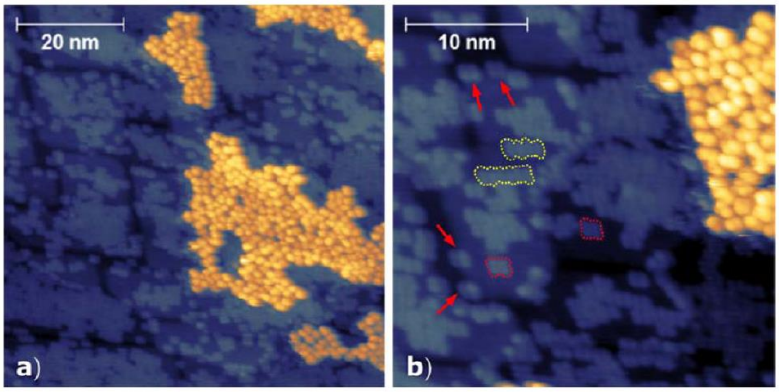

Figure 2.13 STM images recorded at 30 K of a sub-ML coverage of Fe_4Ph on Cu_2N; V = 2.5 V, I = 3 pA. (a) Size = 70 × 70 nm² (b) Size = 31 × 31 nm².

These fragments form small aggregates that features a bilobed unit mainly ordered in small even-member chains (highlighted in yellow and red in Figure 2.13b). The smaller isolated structures, in red in the image, have a tetralobed shape indicating the formation of a superstructure, which does not split even on the trench sites (highlighted by red arrows in Figure 2.13b) where the two halves are at two different heights. The height distribution of these objects on a single Cu_2N domain (i, ii in Figure 2.14) is 0.25 ± 0.05 nm, in line with what has been found on Au(111) and Cu(100) single crystals.

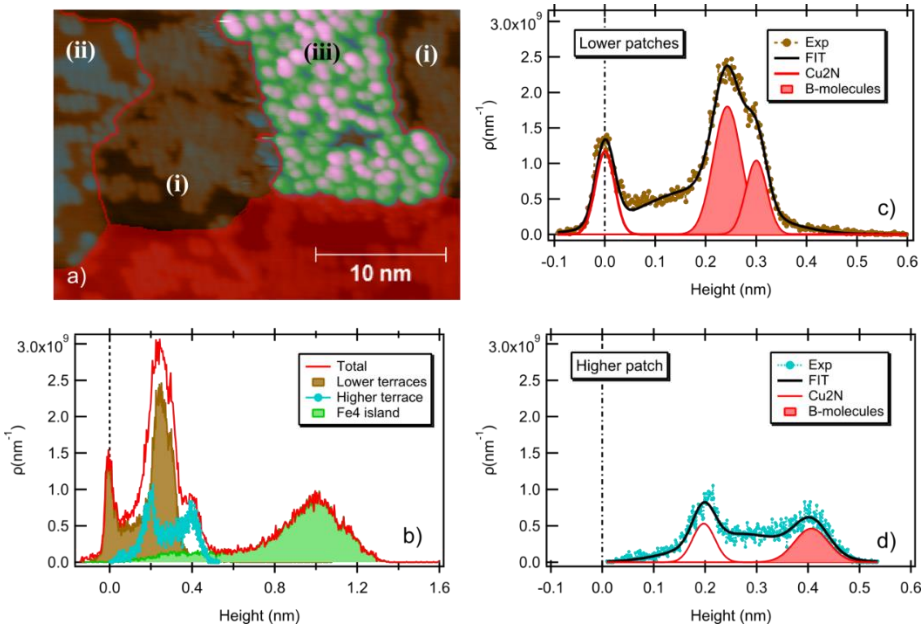

Figure 2.14 STM image of sub-ML deposition of Fe_4Ph on Cu_2N with a size = 31 × 22 nm², V = 2.5 V, I = 3 pA. (b) Total height distribution of the not-hidden areas of the (a) STM image. (c,d) Partial height distribution and relative fitting.

The height distribution of Fe_4Ph reported in Figure 2.14, is centred at ≈ 0.8 nm, in line with the expected value. However, the distribution is very broad demonstrating that the Fe_4Ph lay on top of clean surface, edge trenches and lower-domains. The lateral dimension of Fe_4Ph has been evaluated by Figure 2.15, which is significantly affected by the thermal drift. For this reason both scan directions have been taken into account. The up scan has a broad distribution centred at 1.6 ± 0.2 nm, while the down one is narrower and centred at 1.4 ± 0.1 nm. The average of the two values is 1.5 ± 0.3 nm, still consistent with that expected for Fe_4Ph.

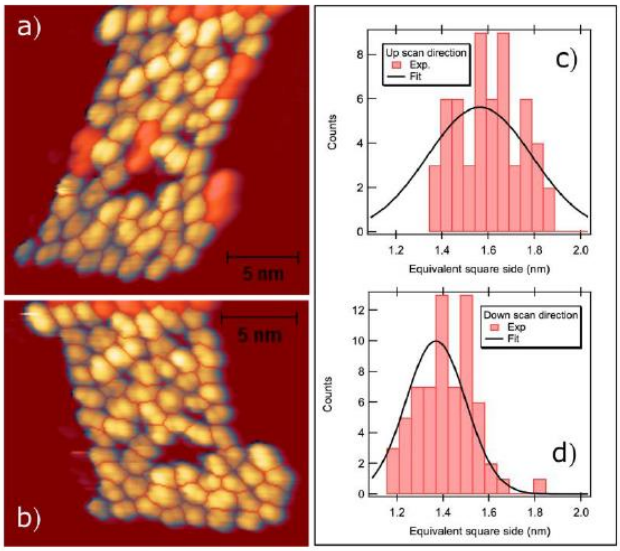

Figure 2.15 Subsequent up and down STM images of a Fe_4Ph island on CuN. I = 3 pA, V = 2.5 V. (a) Up; Size = 21 × 20 nm^2. (b) Down; Size = 19.7 × 15.8 nm^2. Statistical analysis of the Fe_4Ph lateral size for the up (c) and down (d) STM image.

On the basis of STM results, a common scenario emerges from all the investigated surfaces. Fe_4Ph molecules, appearing as brighter spherical objects (height ~ 0.7 - 0.8 nm), can adsorb on the clean substrate or on top of smaller species (height ~ 0.2 - 0.3 nm) which organise differently according to the nature of the surface; *i.e.* ordered domains on Au(111), dendritic layers on Cu(100) and sequences of tetra-lobed units on Cu_2N. On the other hand, the presence of lower species has been quite unexpected and variable from one deposition to the other. However, the surface area covered by these fragments is not negligible at all, rather comparable (Au) or even larger (Cu) than that covered by Fe_4Ph (for more details Lanzilotto *et al.*[62]). Extensive degassing of the Fe_4Ph powder before deposition does not affect the extent of these lower domains. The analysis of the available data indicates a great affinity of these objects for the bare substrates. Indeed, there is no evidence that these objects form multi-layered structure (*i.e.* they do not stick on top of themselves or on Fe_4Ph molecules).

2.4 Deposition of $Fe(dpm)_3$ on gold: the study of a possible contaminant

With the purpose of shedding some light on the chemical nature of the domains of smaller species, we have focused our attention on a very volatile molecule which is known to be a common contaminant in Fe_4Ph sublimated thick film: $Fe(dpm)_3$.[52] We therefore decided to perform a detailed *in situ* study of the deposition of the $Fe(dpm)_3$ molecule on the Au(111) single crystal.[52] In this paragraph it is reported the characterisation of a thin films of the aforementioned complex by UPS, XPS, STM, XAS and the obtained experimental results have been compared with DTF calculations.

The structure of $Fe(dpm)_3$ is illustrated in Figure 2.16. The three dipivaloylmethanide ligands chelate a high-spin (HS) Fe^{3+} ion, producing a distorted octahedral coordination environment.

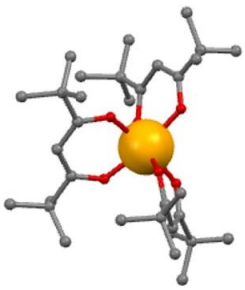

Figure 2.16 Ball and stick representation of the $Fe(dpm)_3$ structure. Colour code: grey = C, red = O, yellow = Fe.

The $Fe(dpm)_3$ has been synthesised by Dr. L. Rigamonti and Prof. A. Cornia (Dipartimento di Scienze Chimiche e Geologiche, UNIMORE).[68] As for the Fe_4Ph deposition, an Au(111) single crystal has been used as a substrate. Considering that $Fe(dpm)_3$, like most of β-diketonates, shows high volatility,[69,70] the sublimation has been performed in a dedicated preparation chamber (see Section 5.8) with a base pressure of 1×10^{-7} mbar. For the sublimation process, a home-made evaporator has been used. Low deposition rates has been obtained by keeping the molecular powders, hosted in the quartz crucible, at room temperature. In order to achieve higher deposition rates, the powders have been heated to a temperature of about 338 K. During the sublimation, the substrate has been kept a room temperature.

2.4.1 UPS and XPS characterisation of $Fe(dpm)_3$ on gold

The UPS spectroscopy has been used to extract the first information on the growth process. Several samples, named $t_1 \ldots t_4$, have been obtained exposing the substrate for growing times, from 30' to 13 h, to the $Fe(dpm)_3$ vapours, *i.e.* keeping the molecular powder at room temperature. Their UPS spectra are reported in the left

panel of Figure 2.17, together with the exposure time of each sample. The UPS spectra have been recorded in normal emission with circular 5 mm entrance and exit slits and a pass energy to 10 eV.

The UPS features of the t_1 sample are very similar to those of the gold substrate, only the appearance of a small peak near −15.7 eV and a slight attenuation of the Au(111) features can be observed. Starting from the coverage t_2, the peaks of the deeper molecular states are visible and the intensity of the gold valence band decreases noticeably. However, passing from an exposure time of 90 min (t_3) to 13 hs (t_4), no evolution of the features is observable. This result suggests a self-limiting adsorption mechanism of $Fe(dpm)_3$ on Au(111) surface.

In order to obtain a thicker film, the growing rate have been increased heating the powders at about 338 K (high rate, HR). In this case for shorter exposure time (t_5 = 1 min) the same features noticed in the t_4 sample are visible. However, the spectra corresponding to longer exposure times shows the same features, so it is has not been possible to dose a greater amount of molecule. This confirms the hypothesis of a saturation coverage for the $Fe(dpm)_3$ on Au(111). The behaviour is not surprising, in fact it has been reported for other metal β-diketonate complexes. For instance, $Cu(hfac)_2$ has been found to chemisorbs with a self-limiting reaction on the TiO_2(110) surface,[71] while multilayers of $Pd(hfac)_2$ can be obtained by cooling Cu surfaces at 120 K.[72]

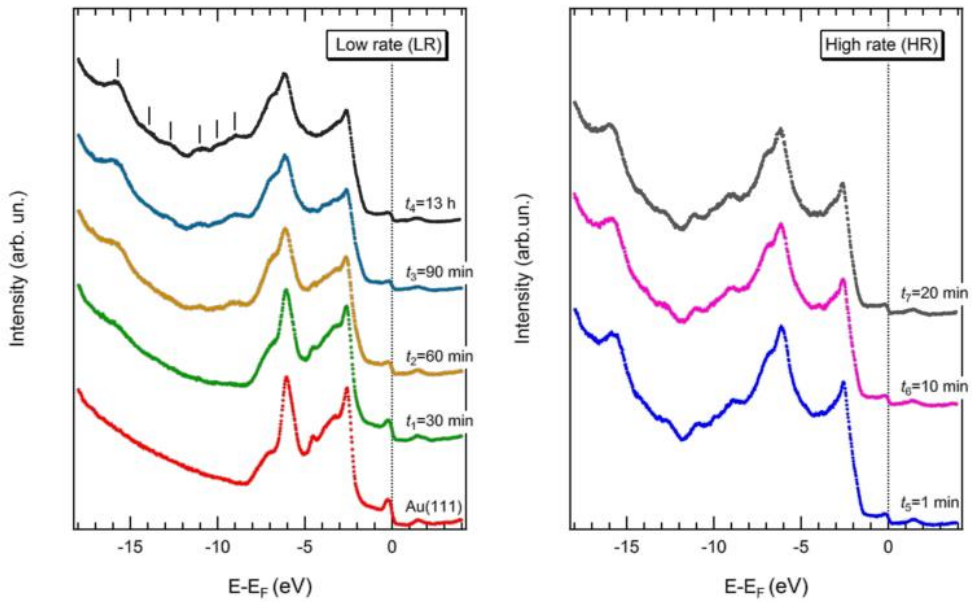

Figure 2.17. UPS spectra acquired for the Au(111) using a He II line (40.8 eV) of samples exposed to increasing doses of $Fe(dpm)_3$ with low (left) and high (right) deposition rates.

The UPS experimental spectra of the gold substrate and the $Fe(dpm)_3$ film are compared with their calculated analogues in Figure 2.18. The density of states (DOS)

for the Fe(dpm)$_3$@Au(111) system has been computed through a periodic density functional approach (see details in ref. 68).

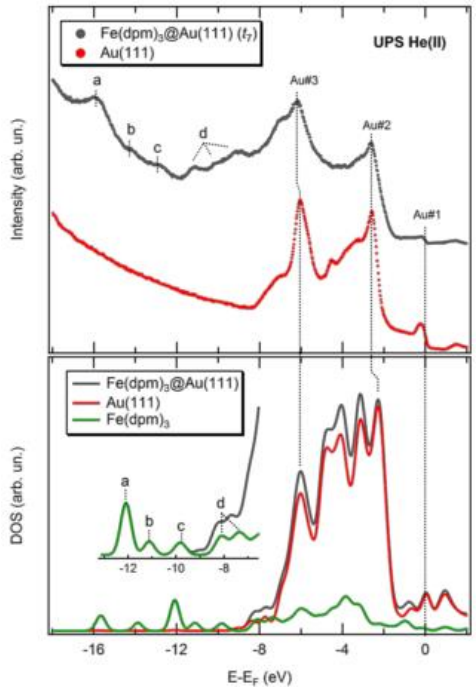

Figure 2.18 (Top) UPS spectra relative to the Fe(dpm)$_3$ saturation coverage (grey curve) and the clean substrate (red curve). (Bottom) Theoretical density of states for the system Fe(dpm)$_3$@Au(111) (grey curve) and decomposition into Au and Fe(dpm)$_3$ contributions.

In the spectrum of the saturation coverage some Au(111) features are still visible: the Fermi edge (Au#1) and between −2 and −7 eV the most prominent peaks (Au#2 and Au#3). On the other hand, the deeper molecular states are visible and labelled as a, b, c and d. The comparison of the experimental and computed spectra of Fe(dpm)$_3$@Au(111) shows a good agreement in the main features. In the computed spectra too the region between −2 and −7 eV is strongly dominated by the gold features while few molecular states are clearly visible only at higher binding energies (at more negative values of $E - E_F$). The observed slight mismatch between experimental and theoretical energy scale can be related to possible deficiencies in the used exchange-correlation functional/basis sets combination.[68,73]

The UPS spectra give some useful information about the growth process of the Fe(dpm)$_3$ on Au(111) demonstrating that no more than one or two ML could be deposited on gold. However, they are not informative on the molecular structure of the objects on the surface because of the strong signal of the substrate.

Additional information can be gained by exploiting the element specificity of XPS. The XPS spectra for the t_1, t_6 and t_7 deposition have been reported in Figure 2.19. As expected, the intensity of the signal for the two saturation coverages t_6 and t_7

is the same. No difference in shape or in binding energy is visible in the C *1s* and O *1s* spectra of the three samples. The signal of the Fe *2p* region is detectable but very noisy for t_6 and t_7 depositions and almost negligible for t_1. This impedes to obtain useful information such as the oxidation state of iron.

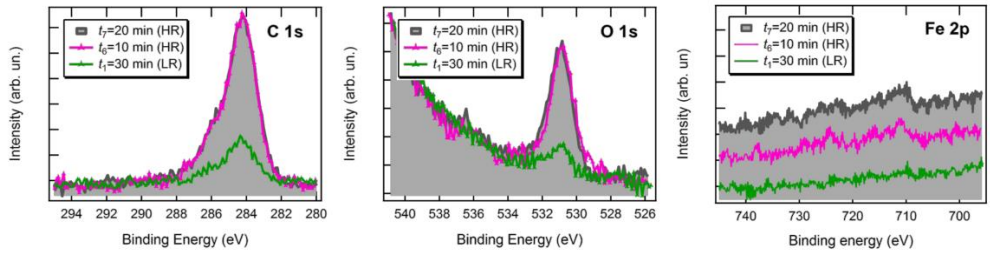

Figure 2.19 C 1s, O 1s and Fe 2p XPS spectra for the Au(111) substrate exposed to increasing doses of Fe(dpm)$_3$. Spectra acquired with a monochromatic Al K_α source.

2.4.2 STM characterisation of Fe(dpm)$_3$ on gold

In order to get more insight in the growth of Fe(dpm)$_3$ we characterised some of the already discussed samples by STM. A large-scale image of the t_1 coverage sample is shown in Figure 2.20a.

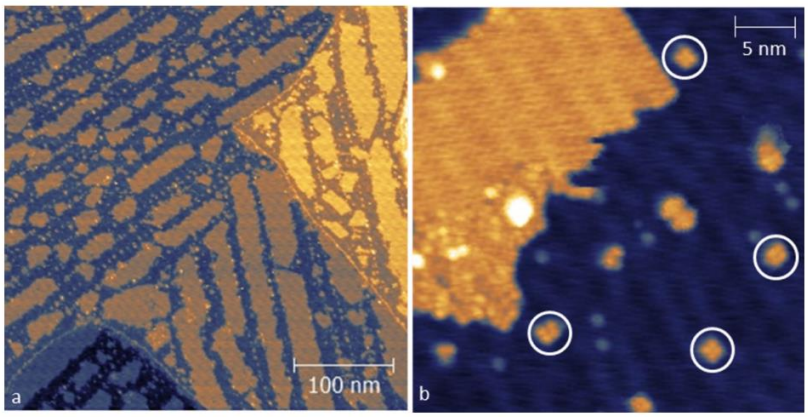

Figure 2.20 (a) STM image of Au(111) surface after exposure to Fe(dpm)$_3$ for t_1 = 30 min (LR) at T = 30 K. (a) Size = 400 × 400 nm^2, bias = −2 V (empty states), I = 10 pA. (b) Size = 34 × 34 nm^2, bias = −2 V (empty states), I = 5 pA.

The Au(111) surface is covered by a sub-ML of regular islands. Reactive sites on the gold substrate, such as the kinks of the herringbone reconstruction and terrace steps, seem to be necessary for the nucleation of molecular domains. In the zoom of Figure 2.21b, the island appears flat and ordered. While the ordering inside the molecular domain cannot be resolved, some isolated objects with a tetralobed structure can be identified. These could be the constituents of the island because the height of the isolated objects (0.29 ± 0.02 nm) is identical to that of the island. The

height of these islands and their arrangement on the substrate in a regular pattern following the herringbone reconstruction recall the B-domain found when Fe_4 molecules are sublimated on gold. Moreover, similar tetralobed isolated objects were also observed on Cu_2N.

A few zones with a second layer has been found and shown in Figure 2.21. The morphology of a part of the second layer is flat and ordered, while some zones are dendritcs. The height of the two domains is comparable suggesting that they are formed by the same objects with different arrangement.

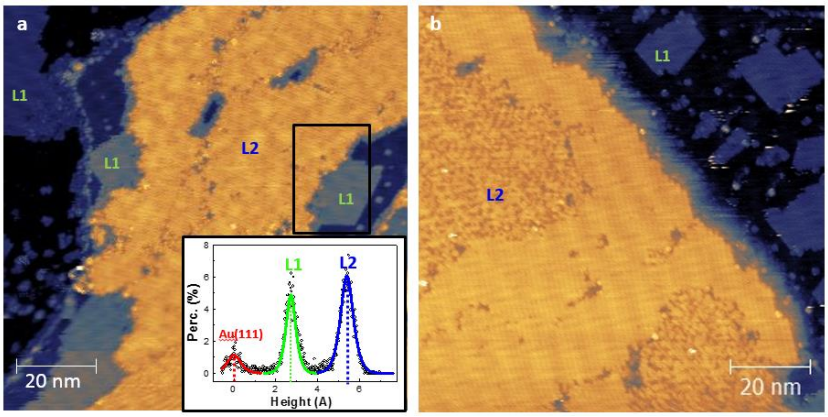

Figure 2.21. STM images of the Au(111) surface after exposure to $Fe(dpm)_3$ for t_1 = 30 min (low rate). First and second layer are indicated as L_1 and L_2, respectively. (a) Size = 100 × 100 nm², Bias = −2 V, I = 3 pA. (Inset) Enlarged view of L2, Size = 18 × 41 nm².

The situation in the high-rate sample t_6 is fairly different. Figure 2.22 shows a gold substrate fully covered with a homogenous dendritic wetting layer. On top of it, isolated quasi-spherical objects with height of 0.35 ± 0.06 nm and a diameter of 1.57 ± 0.21 nm are scattered.

In order to shed some light on the complex scenario revealed by our detailed STM characterisation, a comparison with the STM image of $Fe(dpm)_3$ simulated by DFT calculations has been necessary. The DFT-simulated $Fe(dpm)_3$ is an almost spherical multi-lobed object with a height of about 0.92 nm and a lateral dimension approximately 1.37 nm (see Figure 2.23a). The simulated image resemble the isolated quasi-spherical objects in Figure 2.22. However, the limited experimental resolution and the approximation in the calculation approach do not allow for an unambiguous conclusion. Because of the low resolution, it is even more difficult to find correlations with the features observed within the dendritic regions.

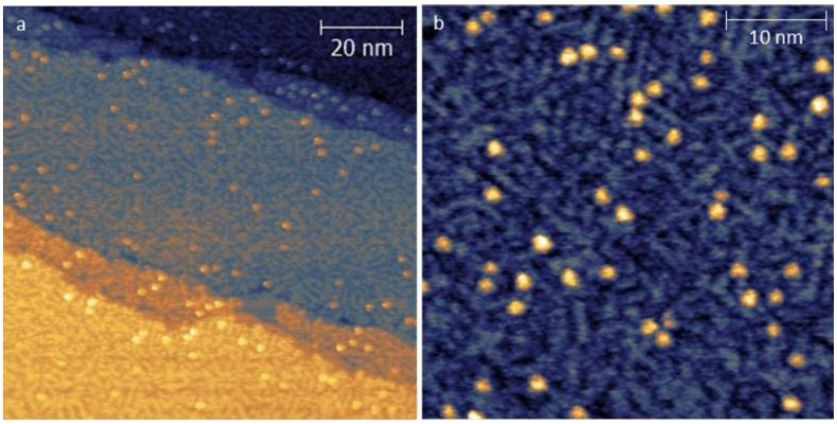

Figure 2.22 STM images for saturation coverage of $Fe(dpm)_3$ on Au(111) at T = 30 K. (a) t_6 = 10 min (HR); size = 100 × 100 nm^2, bias = 1.5 V (filled states), I = 10 pA. (b) t_7 = 1 min (HR); size = 45 × 45 nm^2, bias = 1.5 V (filled states), I = 10 pA.

Passing to the sub-ML coverage, where a better resolution has been achieved, the structure of the simulated STM image for $Fe(dpm)_3$ does not fit with the observed tetralobed features. This suggests a fragmentation of the iron complex when is in contact with the substrate. To comprehend the nature of the tetralobed structures, two possible fragments have been investigated: $FeOH(dpm)_2$@Au(111) and $Fe(dpm)_2$@Au(111). The first represents a partial fragmentation of the pristine complex, while in the second Fe^{3+} ion could experience reduction via $Fe(d_z^2)$–Au(s) interaction giving rise to the low spin (LS) $Fe(dpm)_2$ species. The STM simulated image for the $FeOH(dpm)_2$@Au(111) presents four peripheral lobes and a central one (Figure 2.23b), so it is significantly different from the tetralobed features observed experimentally in Figure 2.23c. On the contrary the STM simulated image of $Fe(dpm)_2$ is similar to the observed structures.

In conclusion, combining STM and DFT techniques it has been possible to partially rationalise the absorption of $Fe(dpm)_3$ on gold. The complex probably is subject to a "dissociative absorption process" when it encounters the gold substrate, giving rise to $Fe(dpm)_2$ fragments. The height of the fragments observed on $Fe(dpm)_3$ and on Fe_4Ph samples on Au(111) is the same, suggesting the same chemical nature of the objects. The observation of similar tetralobed objects in submonolayer of both Fe_4Ph deposited on Cu_2N, and $Fe(dpm)_3$ on Au(111) further supports the hypothesis of the same chemical nature of these objects.

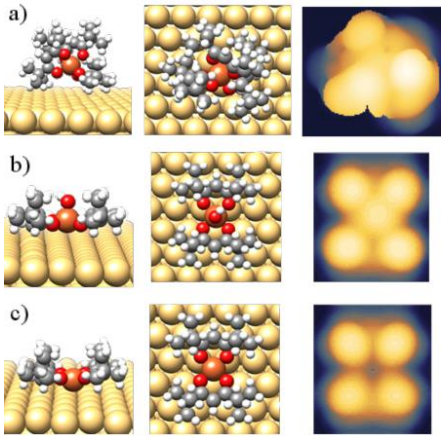

Figure 2.23 Optimized geometries of the three theoretical models Fe(dpm)$_3$@Au(111) (a), FeOH(dpm)$_2$@Au(111) (b), and Fe(dpm)$_2$@Au(111) (c) presented as side (left column) and top views (middle column). Simulated STM images at experimental bias are also reported in the right column. (a) Bias = −1.5 eV (filled states); size = 17.31 × 14.99 Å^2. (b), (c) Bias = 2 eV (empty states); size = 14.44 × 14.99 Å^2.

2.4.3 XAS characterisation of a drop-cast of Fe(dpm)$_3$

Given the interest in Fe(dpm)$_3$ as a potential contaminant of evaporable Fe$_4$Ph, the magnetic characterisation of an *ex situ* sample has been also attempted. Considering that the high coverages compatible with an *ex situ* prepared sample cannot be achieved by UHV sublimation, a thick film sample of Fe(dpm)$_3$ was prepared by drop-casting using a 2 mM dichloromethane solution on a gold film grown on mica. The XAS characterisation has been performed in the Elettra synchrotron in Trieste at the BACH beamline. The XAS spectra at the $L_{2,3}$ edge of iron have been acquired at a temperature of 4 K and a magnetic field of 3 T. The structure of the XAS spectra (illustrated in Figure 2.24) is typical of a HS Fe^{3+}, as indeed expected for a thick film if the reduction is induced by the reaction with the metal surface.[74,75] The amplitude of the XMCD% signal reaches approximately 80% of the isotropic contribution $(\sigma- + \sigma+)/2$, as expected for a set of independent HS Fe^{3+} ions with their magnetic moment fully aligned in the direction of the externally applied magnetic field.[74,75] Interestingly, this value is comparable to the one recorded at the Fe $L_{2,3}$ edge on the heteronuclear Fe_3Cr systems,[58] the isostructural chromium centred analogues of Fe_4 SMMs. On the other hand, the XMCD% intensity observed here is almost twice as large as in Fe_4 SMMs. It is important to recall that in star-shaped Fe_4 SMMs, the field-opposing contribution of the central spin halves the average magnetic polarization per iron site. Full polarization is instead achieved in these conditions for non-interacting Fe^{3+} ions, as in the present case, or for the peripheral and parallel aligned Fe^{3+} spins of Fe_3Cr. To resume, the features of XMCD

spectrum of the $Fe(dpm)_3$, in particular its intensity, are significantly different with respect to the ones of the Fe_4Ph.

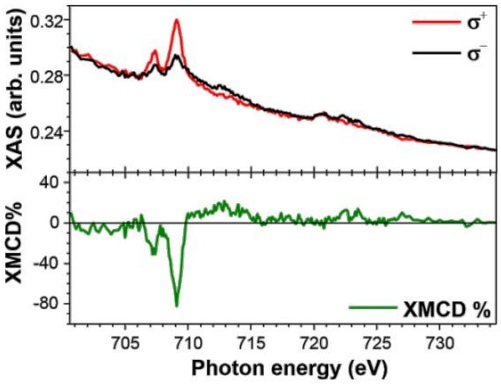

Figure 2.24 X-ray absorption spectra for a bulk sample of Fe(dpm)3 acquired using the left (σ+) and right (σ−) circular polarisation (upper panel) and the derived XMCD% spectrum (lower panel).

2.5 Understanding the Fe_4 fragmentation: the back exposure experiment

From the study of the sub-ML deposition of $Fe(dpm)_3$ it has been hypothesised the common nature of the fragments of $Fe(dpm)_3$ and Fe_4Ph. However, to confirm this hypothesis, we need to have more information on the fragmentation process. To discern between the release of fragments after the interaction of Fe_4Ph with the bare substrate and a collateral degradation process occurring during sublimation, we have devised a "back exposure" experiment.

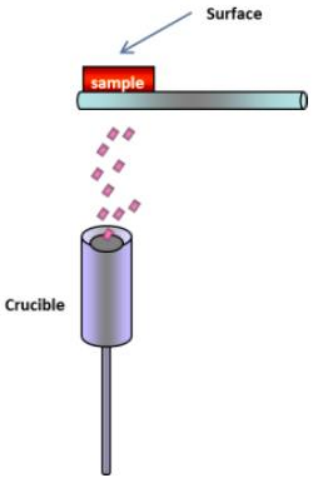

Figure 2.25 Back exposure geometry. The sample is not directly exposed to the molecular flux coming from the crucible

For this investigation the freshly cleaned Au(111) crystal has been set in the sublimation chamber without facing the evaporator heated at the sublimation temperature of Fe_4Ph (see Figure 2.25). After an exposure of t = 30', the Au(111) is covered by a sub-ML coverage of domains of lower species (see Figure 2.26a). Increasing the dose (t = 45' and t = 60', Figure 2.26b and Figure 2.26c), the islands enlarge until they form a complete wetting layer. There is no evidence of formation of a second layer of B-domains, confirming great affinity of these objects for the bare metal surface. More importantly, none of these samples shows any evidence of larger round objects associable to Fe_4Ph molecules.

A high-resolution image of an island on Au(111) is presented in Figure 2.27a. The domain is composed by bilobed structures (#1) that arrange in tetralobed pairs (#2). The latter presents a maximum (diagonal) and a minimum (across the two lobes) of 1.32 ± 0.05 nm and 1.00 ± 0.04 nm, respectively. Similar features have been obtained when the $Fe(dpm)_3$ has been sublimated at subML coverage on Au(111) (see Figure 2.20).

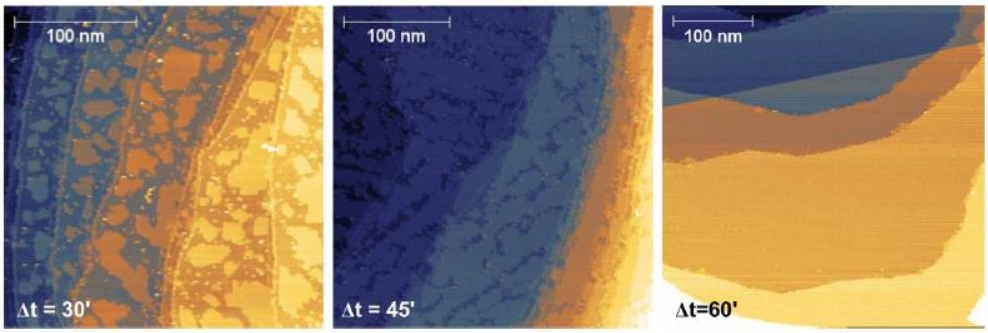

Figure 2.26 STM images of Au(111) substrate exposed for different time intervals (t) to the Fe_4Ph "back exposure". From left to right: t = 30 min, size = 260 × 260 nm² V = - 2 V, I = 3 pA; t = 45 min, size = 300 × 300 nm², V = - 2.1 V, I = 3 pA; t = 60 min size = 400 × 400 nm²; V = - 2.2 V; I = 3 pA.

The STM image of the back exposure on the Cu(100) substrate shown in Figure 2.27b evidence the presence of several bilobed objects. They organise in small dendritic domains as has been observed for the B-domains in the Fe_4Ph deposition. Differently to what has been found on Au(111) and Cu_2N, the bilobed objects do not necessary arrange in tetralobed structures, but some are lone-standing. Moreover, the small chains in Figure 2.27b are both odd and even membered. We can thus suppose a further fragmentation in the case of the copper substrate.

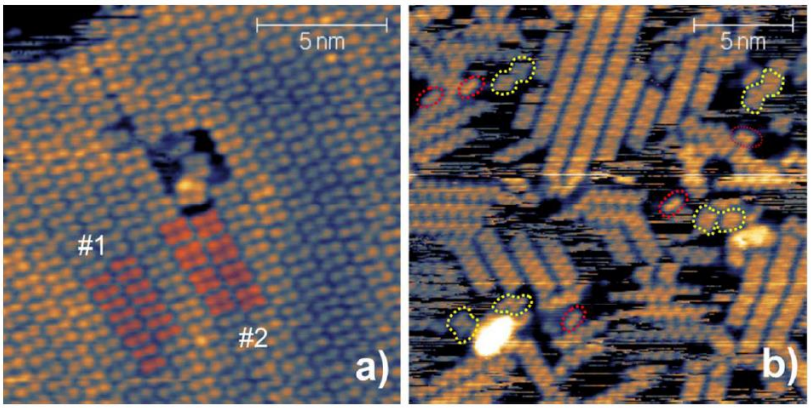

Figure 2.27 High resolution STM images of the B-domains on Au(111) (a) and Cu(100) (b). (a) Size = 15 × 15 nm^2, V = 2.7 V, I = 200 pA; (b) Size = 20 × 20 nm^2, V = 0.7 V, I = 200 pA.

In order shed some light on the chemical nature of the fragments, we performed a spectroscopic characterisation of the fragments. We started with the UPS characterisation of a monolayer of the lower-domain (back exposure t = 60', the sample characterised by STM in Figure 2.26, right) on Au(111). The spectrum has been compared with those of a Fe_4Ph and of $Fe(dpm)_3$ in Figure 2.28. Spectra of $Fe(dpm)_3$, Fe_4Ph front and back exposure (coverage below or close to 1 ML) are very similar to each other, being mainly characterised by the intense peaks of the gold valence band that is "contaminated" by a weak molecular "bumps" in the deeper energy region (*i. e.* inelastic electron tail) between 7 and 16 eV.

DOS calculation evidenced that these deeper states (indicated with the dashed lines) are mainly due to the molecular states localised on the dpm^- ligands that are common to all the species.[68] The similarity between the spectra of the $Fe(dpm)_3$ and the back exposure (see asterisks in Figure 2.28) are even stronger, confirming the common nature of the adsorbed species.

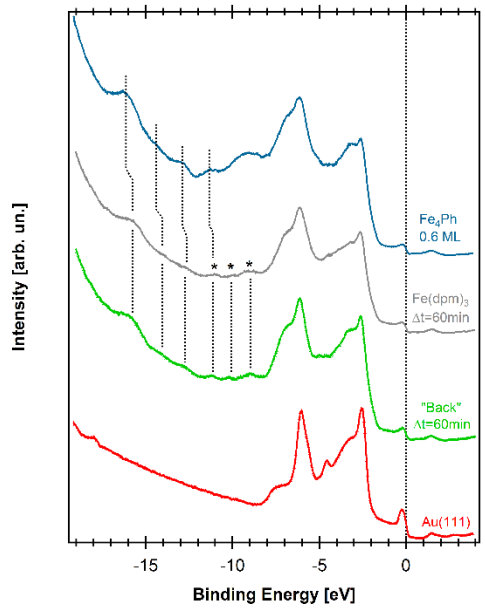

Figure 2.28 Comparison of HeII spectra of Fe_4Ph (both front and back exposure), $Fe(dpm)_3$ and bare gold. The dashed lines indicates the contribution of the dpm^- ligands, while the asterisk indicates the β-diketonates states that in Fe_4Ph are covered by the states of the tripodal ligand.

To gain element selectivity, XPS on the back exposure sample (t = 60 min) on Au(111) has been performed. The spectra of the different regions are compared with the one of a 1.1 ML of Fe_4Ph on Au(111) in Figure 2.29. It must be noted that the spectra illustrated in this section has been acquired with the new analyser (see Section 5.8) thus they are more informative with respect to that in Section 2.4.1. C *1s* and O *1s* peaks, which are normalised to their own intensity maximum, do not differ significantly in the two samples, as we could expect, indicating that the adsorbed molecules are chemically similar. After a proper scaling, the Fe *2p* peak reveals much more information. The Fe $2p_{3/2}$ peak of the 1.1 ML of Fe_4Ph shows a dominant signal above 710 eV attributed to the Fe^{3+} and a small shoulder at *ca.* 708.5 eV. The latter constitutes the main feature observed in the sample obtained with the back exposure. The lower energy of the peak allows attributing this contribution to Fe^{2+} ions.

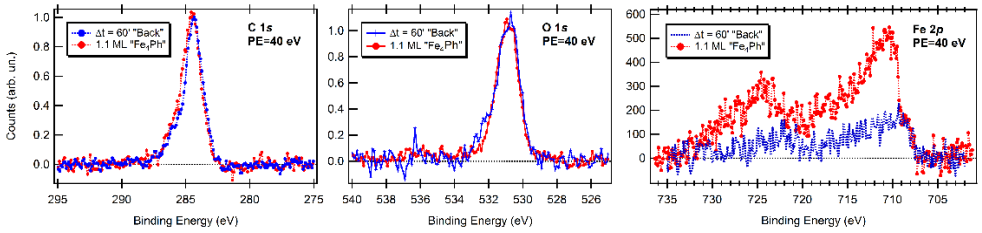

Figure 2.29 XPS spectra region for the 1.1 ML of Fe_4Ph and back exposure on the Au(111) substrate. The spectra are acquired with P.E. = 40 eV. The binding energy scale has been calibrated by locating the substrate Au $4f_{7/2}$ peak at 84.0 eV. All spectra are shown after a proper background subtraction.

Performing a reliable quantitative analysis of the XPS spectra in Figure 2.29 (acquired at P.E. = 40 eV) is far from trivial, mainly because of the small S/N ratio in the iron region, especially for the back exposure. For this reason we have acquired the XPS spectra using a P.E. = 100 eV known to have a better S/N. The semi-quantitative analysis is reported in Table 2.1. The atomic ratios for Fe_4Ph and $Fe(dpm)_2$ are very similar, so it is not surprising that the semi-quantitative analysis of the 1.1 ML do not deviate strongly from the expected values of pure Fe_4Ph.

In conclusion, both topographic and spectroscopic features of B-domains/Au(111) are very similar to those obtained when sublimating the mononuclear complex $Fe(dpm)_3$ on Au(111) at subML coverage.

Table 2.1 Semi-quantitative analysis from XPS data taken with PE = 100 eV for 1.1 ML of Fe_4Ph and a wetting layer of B-contaminants, both on the Au(111) surface. The results are compared with the theoretical values expected for the species involved in the sublimation and adsorption process.

	C/Fe	**O/Fe**	**C/O**
1.1 ML Fe_4Ph	22	4.1	5.4
Back exposure	23	3.8	6.1
Fe_4Ph (theoretical)	22	4.5	4.8
$Fe(dpm)_2$ (theoretical)	22	4.0	5.5

In this chapter, thanks to the XMCD characterisation, we demonstrated that the Fe_4Ph can retain the slow relaxation of the magnetisation after the UHV sublimation on gold surface. However, the thermal deposition of Fe_4Ph submonolayers studied *in situ* with STM, UPS and XPS unravels a complex scenario. Three surfaces with different reactivity have been employed to fully understand the growth process. In addition to intact Fe_4Ph molecules, domains of smaller molecular entities (so called B-domains) have been clearly detected even on the semi-insulating Cu_2N substrate, suggesting that they do not originate from on-surface decomposition but rather from thermal degradation of the compound. This hypothesis is further corroborated by the observation of B-domains in back-exposure experiments with no traces of Fe_4Ph, suggesting that the substrates are polluted by very volatile species present in the chamber. However, these species are not generated by reaction of Fe_4 with the substrate. Interestingly no contaminants have been observed in experiments where Fe_4Ph has been deposited by electro-spray,[76] though the hexagonal boron nitride (BN) substrate employed could also have a lower affinity for the fragments. It is thus likely that partial thermal degradation of Fe_4Ph yields $Fe(dpm)_3$, which in turn decomposes in different ways depending on the type of surface. According to STM, photoemission and DFT studies, the tetralobed structures observed on Au(111) and Cu_2N are $Fe(dpm)_2$ complexes. On-surface decomposition is much more effective on Cu(100), where it leads to further fragmentation.[62] Since all these contaminant species originate from a very volatile complex produced during sublimation, it is not surprising that the

geometry of the preparation chamber, the deposition rate and temperature, the pumping efficiency, and other parameters significantly affect surface coverage by B-domains. This could justify why no significant amount of Fe^{2+} has been detected in synchrotron experiments. In this respect, an appropriate design of the deposition chamber can, in principle, mitigate these problems. However, I want to point out that the gold used for the low temperature XAS-XMCD experiments was not a single crystal cleaned *in situ* and this could have reduced the sticking coefficient of the fragments. In order to check this point, further synchrotron experiments have been performed and they are subject of the following section.

2.6 Towards the study of the influence of dipolar field in Fe_4 SMM dynamics

The study of the Fe_4Ph led to important insights in the growth of film of evaporable molecular complexes. We therefore decided to explore another volatile Fe_4 SMM, Fe_4SMe, and the structure of this molecule is illustrated in Figure 2.30. Also the synthesis of this complex has been performed by Prof. A. Cornia at the University of Modena and Reggio Emilia. As the synthesis and magnetic properties of this novel derivative are not yet published we briefly describe them here.

The ligand H_3L has been prepared in 23% yield by refluxing a water solution of 3-(methylsulfanyl)propanal, excess paraformaldehyde (4.5 equivs.) and triethylamine (1.5 equivs.) for several hours.[77] After complete evaporation of all volatiles, the crude product has been purified by column chromatography (SiO_2 gel, $CHCl_3$:MeOH gradient). He obtained the $[Fe_4(L)_2(dpm)_6]\cdot 0.5Et_2O$ compound as large, X-ray quality orange crystals by reaction of $[Fe_4(OCH_3)_6(dpm)_6]$[43] and H_3L (4.8 equivs.) in anhydrous diethylether and subsequent slow evaporation of the solvent in a methanol trap. The identity of the product has been confirmed by elemental analysis, Electrospray Mass Spectrometry and single-crystal X-ray diffraction.[77] The structure of Fe_4SMe is analogous to that of Fe_4Ph (see Figure 2.31), except for the tripodal ligand. The presence of the methanethiolate moiety in the tripodal ligand suggests a more selective affinity of the molecule with the gold substrate.

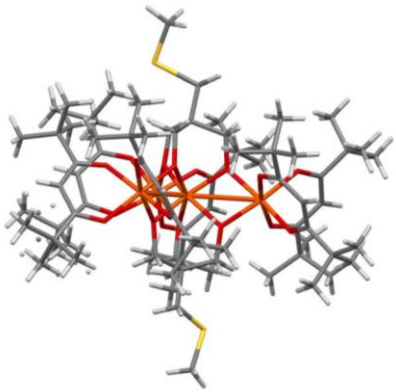

Figure 2.30 Fe_4SMe structure; colour code: C = grey, Fe = orange, O = red.

The bulk magnetic properties of the Fe_4SMe have been investigated by SQUID magnetometry. The molar magnetic susceptibility and the magnetisation of the Fe_4SMe are reported in Figure 2.31 left. In the χT *vs.* T (where χ is the magnetic susceptibility) plot the characteristic Fe_4 behaviour is observed, the dominant antiferromagnetic interaction between the central and the peripheral Fe^{3+} generates a ground $S = 5$ state.[14,15,43] The χT value firstly decreases when cooling down from room temperature going through a minimum, around 100 K, and then reaches a maximum at *ca.* 15 K. Further cooling results again in a decrease of the magnetic moment. Quantitative fitting of the data using a Heisenberg spin Hamiltonian with nearest-neighbour (J) and next-nearest-neighbour (J') gave the following parameters: $J = 15.0$ (4) cm^{-1} and $J' = -0.1$ (3) cm^{-1} (for the definition of J and J' parameters see insert in Figure 2.31 right).[43] Fitting the magnetisation data using the Zero-Field Splitting plus Zeeman Hamiltonian resulted in a $D = -0.41$ (8) cm^{-1}.[43] The Fe_4SMe presents a magnetic behaviour similar to that observed for other Fe_4 analogue and in particular of the Fe_4Ph.[14,43]

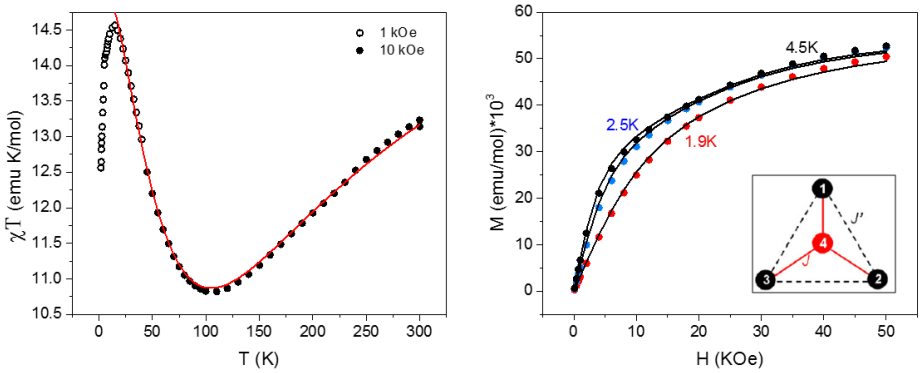

Figure 2.31 (Left) temperature dependence of the χT of the Fe_4SMe in 1 and 10 applied kOe. The solid lines provide the best fit to the experimental data, as described in the text. (Right) Magnetisation curve reported for three different temperatures. The caption schematise the J and J' parameters. The solid lines provide the best fit to the experimental data, as described in the text.

It has been previously demonstrates that thick films of Fe_4SMe can be grown on different substrates using thermal deposition in High Vacuum without inducing changes in the chemical structure and in the magnetic properties of the molecule.[78] In the following section, we present the results of thorough (STM, XPS, XMCD) characterisation of an *in situ* prepared submonolayer of Fe_4SMe.

2.6.1 STM and XPS characterisation of a submonolayer of Fe_4SMe

As for the Fe_4Ph, the grinded powders of Fe_4SMe have been degasses for two days slightly below the sublimation temperature, in order to eliminate possible volatile impurities. The Fe_4SMe powders sublimate in a temperature range between 480 and 510 K.

After the sputtering and annealing of the Au(111) single crystal, a 0.7 monolayer coverage of Fe_4SMe has been sublimated on the substrate, which has been subsequently cooled down to 30 K for the STM investigation. A large scan area of the 0.7 ML of Fe_4SMe molecule is presented in Figure 2.32a. The several islands that spread on the stepped Au(111) strongly resemble the ones of Fe_4Ph observed on gold single crystal (see Section 2.3). The zoomed image of Figure 2.32b shows that these islands are constituted by quasi-spherical Fe_4SMe molecules forming a regular hexagonal pattern. This pattern is clearly highlighted by calculating the bidimensional Fourier transform of the region included in the black square in Figure 2.32b; the distance between the bright hexagonal spot is 1.39 ± 0.09 nm, a value in line with the expected lateral size of these molecules when closely packed.

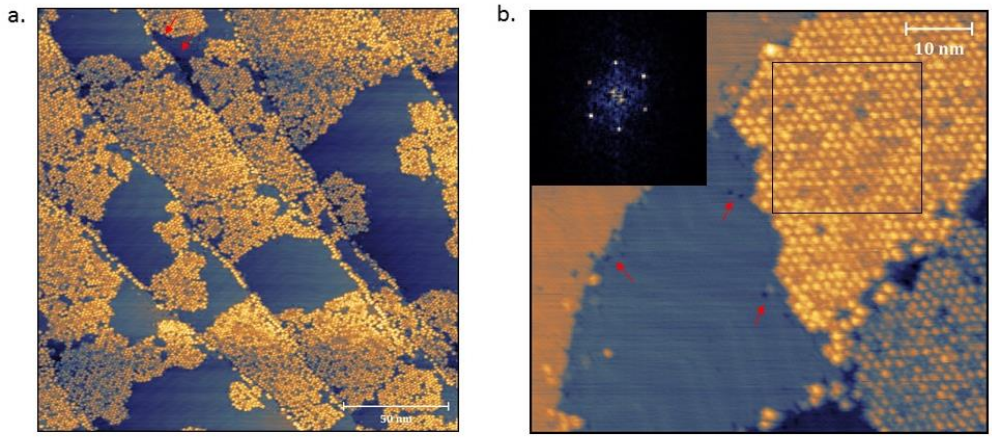

Figure 2.32 STM images of a 0.7 ML deposition of Fe_4SMe on Au(111).
(a) Size =200 × 200 nm^2; I = 5 pA; bias = -3 V; (b) size = 100 × 63 nm^2; I = 3 pA; bias = -2 V.

In analogy to Fe_4Ph, Fe_4SMe molecules, at this coverage, are not directly in contact with the Au(111) surface, but lay mainly on fragments. In fact some defects, indicated in Figure 2.32b by the red arrows, are present on the wetting layer of

fragments. A clearer evidence is given in Figure 2.33a, where the underlying gold substrate is visible. The height distribution extracted from Figure 2.33 shows the presence of two populations. The peak at 0.53 ± 0.08 nm is the one of Fe_4SMe, which appears to be less tall than Fe_4Ph (≈ 0.82 nm). This difference could be explained by the fact that the tripodal ligand of the Fe_4SMe is more flexible and less bulky with respect to the Fe_4Ph, giving rise to a more efficient stacking.

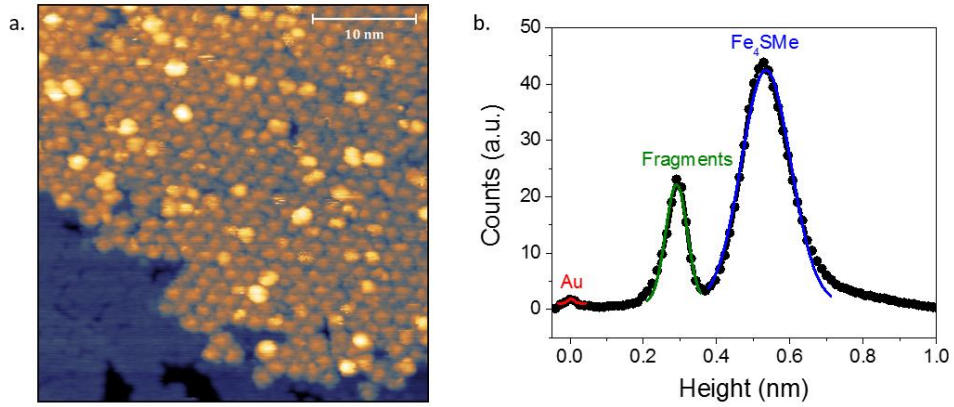

Figure 2.33 (a) STM image of a 0.7 ML deposition of Fe_4SMe on Au(111); dimension = 38 × 38 nm^2, I = 5 pA, V = -2.5 V. (b) Height distribution of the STM image in (a), the fitting has been performed including three Gaussian components attributed respectively to the substrate level, to fragments and to the Fe_4 layer.

The peak in the height distribution of Figure 2.33b fitted with the green line is related to fragments and has a mean value of 0.29 ± 0.04 nm, which is in good agreement to what has been found for the fragments in the submonolayer film of Fe_4Ph on Au(111). The shape of the fragments (see Figure 2.34) is analogous to what has been previously observed: bi-lobed features organised into rows, which stack laterally to give a periodic structure. The quality of the data is not good enough to give a precise value of the distance between the lobes, which is estimated to be around 1.3 nm. We have previously shown that the fragments are most likely $Fe(dpm)_2$, thus containing the β-diketonate ligands present in both Fe_4Ph and Fe_4SMe. For this reason, the concurrency of the same fragments in the Fe_4SMe sub-monolayer is not surprising.

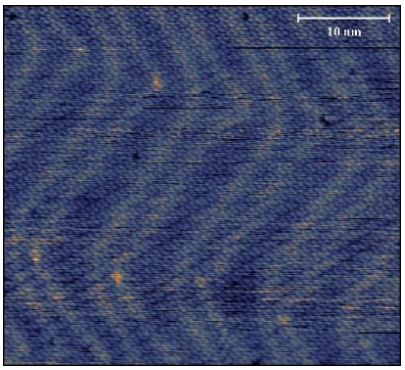

Figure 2.34 STM image of B-domains in a 0.7 ML deposition of Fe_4SMe on Au(111); dimensions = 40 × 43 nm^2, I = 5 pA, V = -3 V.

The XPS characterisation of the 0.7 ML sample has been performed in order to check the intactness of the Fe_4SMe on the surface. The elements constituting the molecule are all visible in the XPS characterisation shown in Figure 2.35. The binding energy scale has been calibrated by setting the Au $4f_{7/2}$ peak at 80.0 eV. The C *1s* region presents two peaks; the main one (284.4 eV) is constituted by the aliphatic carbons and the shoulder at 286.0 eV by the carbonylic and alcoholic carbons. The main O *1s* peak is observed at 530.8 eV. The Fe *2p* region has been fitted with three components for each of the two spin orbit peaks. The main component is found at 710.9 eV, thus iron is mainly present in the Fe^{3+} state. It is not possible to exclude a small content of Fe^{2+}, since a small shoulder at lower binding energy can be glimpsed. This contribution at smaller binding energy can be attributed to the fragments observed in the STM images, the $Fe(dpm)_2$. However, the low coverage and the small signal-to-noise ratio of the measurements, do not allow unambiguous conclusions.

A semi-quantitative XPS analysis has been performed. Since only two sulphur atoms are present for each Fe_4SMe molecule and being the cross section of the S *2p* peak small, the signal-to-noise ratio in this region is low and the sulphur contribution was not measurable and cannot be included in the semi-quantitative analysis. A linear background has been subtracted to the different regions. However, the choice of the background subtraction resulted critical for the O *1s* region, which is in the descending slope of the Au $4p_{3/2}$ peak. The linear background in fact gives an under-estimation of 17% of the oxygen abundance, while the Tougaard background gives a value inside the error bar (assumed to be 5%).

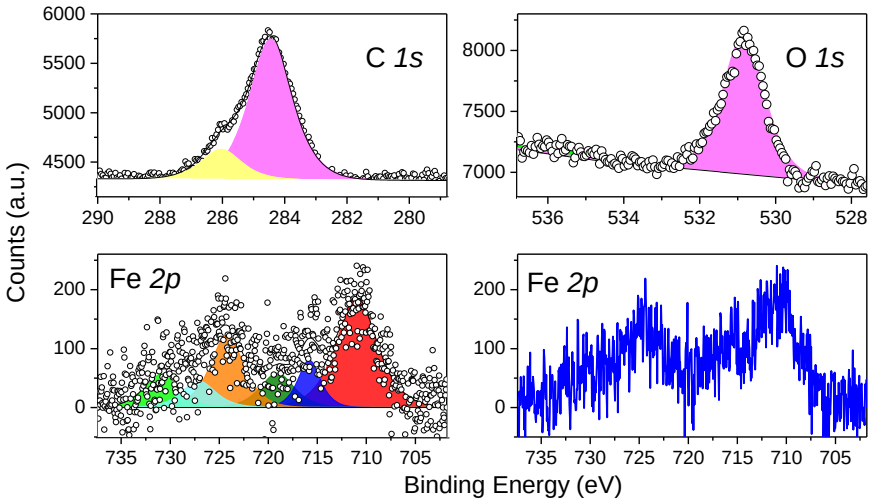

Figure 2.35 XPS spectra regions for the 0.7 ML of Fe_4SMe on the Au(111) substrate. The C 1s, O 1s, Fe 2p peaks are reported with the appropriate fitting, after a linear background subtraction. The Fe 2p region has been reported also without the fitting and as a line graph in order clarify the structure of the spectrum.

A similar treatment has been earlier used for other Fe_4 molecules in order to take in to account the presence of the Au 4s signal at 763 eV.[79] The semi-quantitative analysis of this sample resulted in agreement, within the experimental error, with the theoretical expected values (see Table 2.2), thus the presence of fragments does not modify the semi-quantitative analysis. This is in line with what we observed for Fe_4Ph.

Table 2.2 Semi-quantitative analysis of the XPS data of a 0.7 ML Fe_4SMe on Au(111).

	% Fe *2p*	**% C *1s***	**% O *1s***	**C/Fe**	**C/O**	**O/Fe**
Fe_4SMe **O *1s* Linear baseline**	4.2	80.9	14.9	19.4	5.4	3.6
Fe_4SMe **O *1s* Tougaard baseline**	4.0	78.4	17.5	19.4	4.5	4.3
Fe_4SMe theoretical	4.0	78.0	18.0	19.5	4.3	4.5

2.6.2 XAS characterisation of Fe_4SMe submonolayer film

A submonolayer of Fe_4SMe has been investigated using synchrotron radiation already described above using again TBT as end station (see Section 5.6) at the X11MA-SIM beamline of the Swiss Light Source (PSI, Switzerland).

The substrate used for this characterisation has been, in contrast to previous studies, an Au(111) single crystal. In order to accurately reproduce the preparation

performed in the CeTeCS lab, we have improved the end-station in order to clean *in situ* the substrate by sputtering and annealing. Being the geometry of the preparation chamber in the TBT completely different with respect to that in Florence, we have also calibrated the thickness the film by growing *in situ* the Fe_4SMe film and monitoring by XAS the edge jump as earlier described for Fe_4Ph. The edge jump of the sample also in this case has been compared with the edge jump detected in the same conditions on two chemically grafted monolayers of Fe_4C_9, a dense and a sparse monolayer film (an edge jump of 13.6 % and 9.3%, respectively). Since the comparison of the packing of a sublimated and a chemically grafted film is not ease, we estimate the intermediate values of the two calibrations a good coverage evaluation of the Fe_4SMe film (see Figure 2.36). The film has been then prepared in several steps, in order to carefully evaluate the coverage and not exceed the monolayer. This is of crucial importance in order to obtain a 2D pattern, as the one observed by STM, and properly evaluate the dipolar contribution. After four evaporation steps, a submonolayer coverage showing an edge jump of 6.3 % has been obtained on the Au(111), which with the previous calibrations suggests a coverage of 0.55 ± 0.10 ML.

The 0.55 ML sample has been subsequently transferred into the TBT cryostat and cooled down to *ca.* 0.7 K, the temperature at which we performed both XNLD and XMCD characterisations. The XAS spectra acquired at the Fe $L_{2,3}$ edge, shown in Figure 2.37, are typical of the Fe_4 family.[16,17,56] The presence of a relevant amount of Fe^{2+} contribution has not been detected from the recorded XAS spectra. This confirms that no fragments are sticking on the surface with this experimental set-up. The substrate preparation for this XAS experiment was analogous to that used for the STM and XPS analysis. Therefore, the chamber geometry and the pumping system seems to play the major role in the contamination of the surface by the fragments.

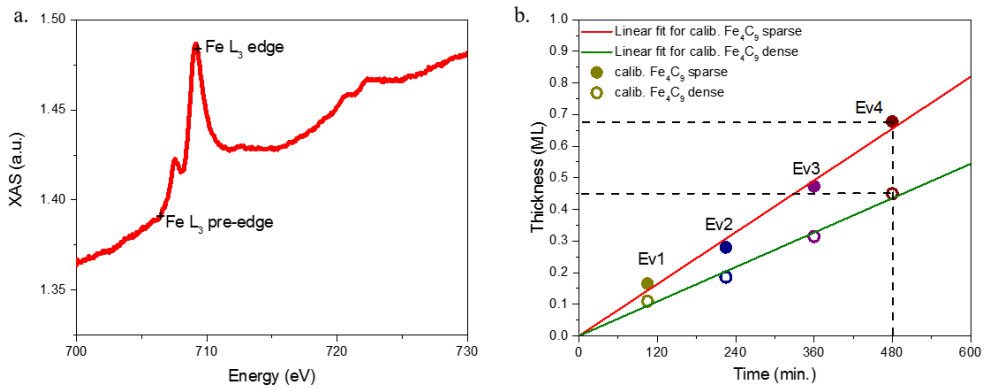

Figure 2.36 (a) X-ray absorption spectra at the Fe L_3 edge acquired for 0.55 ML of Fe_4SMe on Au(111) (300 K and $\theta = 0°$). (b) Thickness versus time of growing coverage films; two calibration are reported, as discussed in the text.

We have done an XNLD characterisation of the film to gain more insight in the organisation of the molecule on the substrate. The XNLD spectrum is illustrated in Figure 2.37 left. The experiment has revealed well-defined spectral features with an overall shape similar to what has been obtained, both experimentally and by calculations, for the Fe_4 systems chemically grafted on gold.[16] The total XNLD signal of the Fe_4SMe film is around 13%. The value is rather strong compared to the 3.5 % of the Fe_4C_5 Self-Assembled Monolayer. The Fe_4SMe molecule presents therefore a preferential orientation on the gold substrate.

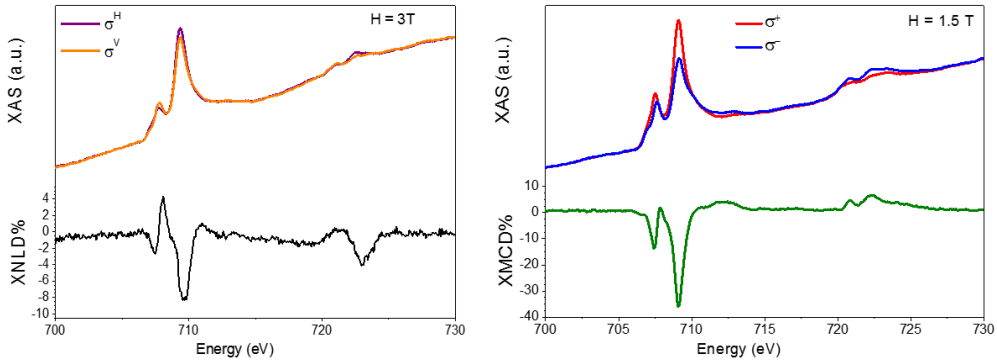

Figure 2.37 XAS, XMCD (a) and XNLD (b) spectra of a sub-ML coverage of Fe_4SMe on Au(111) recorded at 0.68 K.

The results of the XMCD investigation are shown in Figure 2.37 right. The amplitude and the shape of the XMCD signal with a null dichroism in between the two main peaks of the L_3 edge are comparable to those found for the evaporable Fe_4Ph (see Section 2.3.1.) and the Fe_4C_9, Fe_4C_5 chemisorbed on gold,[16,17,56] confirming the intact structure of the tetranuclear clusters.

The hysteresis curves reported in Figure 2.38 have been obtained by monitoring the field dependence of the XMCD signal at the energy of its maximum amplitude, *i.e.* 709.1 eV. The hysteresis loop has been recorded at two different orientations of the magnetic field, $\theta = 0°$ and 45°, with respect to the normal at the surface (see Figure 2.10). The measurements performed at $\theta = 0°$ revealed the expected butterfly shape with a quantum tunnelling of the magnetisation (QTM) step at zero field and at ± 0.48 T, a value similar to that of in the Fe_4Ph and in good agreement with the calculated values (Section 2.3).[56] Moreover, the XMCD signal at $\theta = 0°$ increases rapidly to the saturation value, while a more gradual slope is observed for $\theta = 45°$. This phenomenon, already observed for the Fe_4Ph sublimated film, is attributed to a preferential orientation of the molecules, which is here expected to be more pronounced given the larger natural dichroic signal.[56]

We also measured the relaxation time of the Fe_4SMe that are reported in Figure 2.38. Also in this case the system has been prepared by applying a 1 T magnetic field perpendicular to the surface of the sample, then the magnetic field has been quickly

swept to a final value (-0.45 T, -0.25 T, -0.025 T for black, pink and green curves in Figure 2.38) where the time evolution of the XMCD signal at 709.1 eV is recorded. In the three cases we found a characteristic decay time of 721 ± 13 s, 1254 ± 32 s, 548 ± 90 s, respectively, by fitting the XMCD data with monoexponential curves. The exponential decay clearly shows that the slower relaxation time is found for the intermediate curve (from 1 T fast sweeping to -0.25 T) as it lies in between the resonant QTM steps. The time-decay curve recorded near-zero field (from 1 T fast sweeping to -0.025 T) resulted more noised because of the low signal-to-noise quality of the response of the TEY detector. On the basis of these indications also for this sample we can infer that the magnetisation dynamics of the Fe_4SMe deposits is in a first approximation similar to that found on Fe_4Ph monolayers.

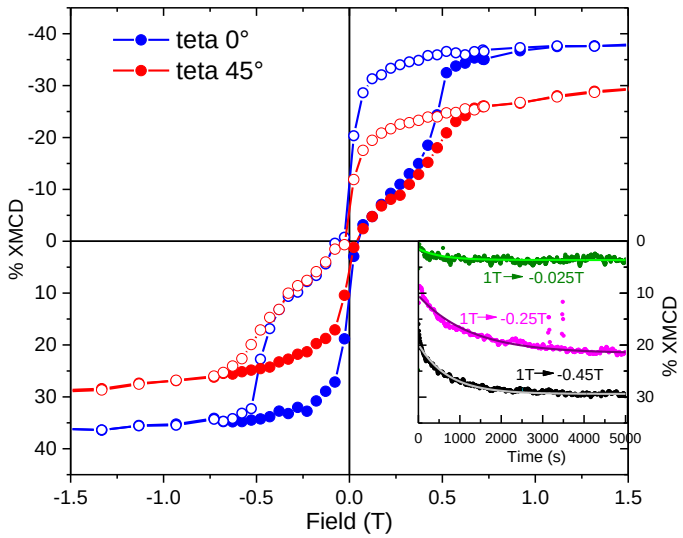

Figure 2.38 Magnetic hysteresis curves obtained at 0.68 K by monitoring the field dependence of the XMCD signal at the energy of its maximum amplitude. A complete hysteresis loop (starting at 1.525 T) is acquired in around one hour. In the insert are reported the relaxation times recorded at θ = 0°.

Dipolar field contribution

The sample described in the previous paragraph obtained by the deposition of Fe_4SMe on gold is a good model system to study the influence of the dipolar interaction in a 2D system. The Fe_4SMe forms densely (hexagonal) packed submonolayer film where the Fe_4 has an out-of-plane magnetisation and the distribution of the easy axis of the magnetisation was evaluated to form an angle analogous of that of Fe_4Ph with the normal to the surface.[56] The orientation of the Fe_4SMe molecules on the surface is confirmed also by the strong XNLD signal.

The total spin of each molecule interacts through the space *via* dipolar interactions. This interaction is due to the local magnetic field produced by each

Fe_4SMe on the neighbour ones. The dipolar interaction between two dipoles (1, 2) is described as follows:

$$J_{1,2} = \frac{\mu_B^2}{R^3}\left(\overrightarrow{\mu_1}\cdot\overrightarrow{\mu_2} - 3\frac{(\overrightarrow{\mu_1}\cdot\vec{R})(\vec{R}\cdot\overrightarrow{\mu_2})}{|R|^2}\right)$$

where R is the distance between the 1 and 2 dipole with magnetic moment μ_1 and μ_2.

The contribution of the local dipolar field is particularly evident for the system that we are considering. In a crystal, the magnitude and orientation of local dipolar contribution are crucially dependent on the crystal structure. In a tridimensional cubic lattice when the sample is fully magnetised the dipolar field generated by the surrounding spins is fully compensated. In general very weak, the dipolar interaction can have significant effects in the dynamics of SMM when the tunnelling mechanism of relaxation is dominating. In fact, the reversal of a magnetic moment strongly modifies the local field on neighbouring spins and the resonant condition necessary to have an efficient tunnel relaxation can be either approached or pushed away. This phenomenon of dipolar shuffling has been investigated in crystalline materials,[48,80,81] but should manifest itself in a more pronounced way in strictly 2D lattices.

In a 2D lattice with a magnetisation out of plane, the interaction between the magnetic moments via the dipolar interaction is always antiferromagnetic. Thus, when the Fe_4 film is at the saturating magnetic field (*e.g.* $B_{ext} = -1.5\ T$), the demagnetising field due to the dipolar contribution should corresponds to the entire magnetisation of the sample, thus is maximum. When the field is swept from -1.5 T, approaching to zero, the spin would feel the local demagnetising field (that is always opposite to the external field, thus is positive), and the condition for the resonance would not be met when $B_{ext} = 0\ T$ but when $B_{ext} + B_{loc} = -1.5\ T$, where B_{loc} is the local field. Since the local demagnetising field is always opposite to the external field, positive in this case, the QTM would appear before zero field. We also expect to see the "dipolar shuffling" in the region near to zero.[48,82] When the magnetic moments of the individual spin start to flip, the local field experienced by each molecule would be different from site to site, and this provokes a broadening of the magnetisation step. A schematic representation of the interaction is reported in Figure 2.39.

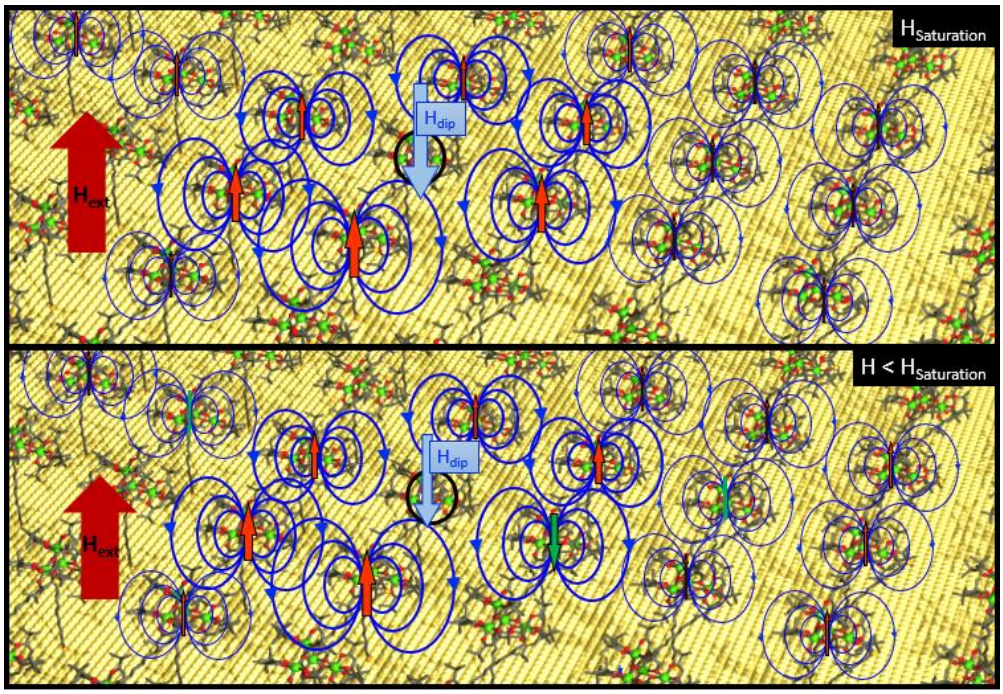

Figure 2.39 Representation of the effect of local dipolar field on the Fe_4 molecule inside the black ring.

In order to calculate the dipolar field contribution we have to study a system of coupled spin. However, the complexity of the numerical approach scales exponentially with the number of spin taken into account. Thus, a new approach has been developed by Dr. A. Vindigni from ETH (Zurich) using the kinetic Monte Carlo (MC).[83,84] The classical Metropolis Monte Carlo investigates the property of a system at the equilibrium, *i.e.* when the system follows the Maxwell-Boltzmann statistic. No information on the dynamics of the system is given. The kinetic MC allows to obtain information on the time evolution of the investigated system. The method presupposes a good knowledge of the system, described in this case with the master equation, and of the transition rates between the different m_S levels. Thus, the kinetic MC describe the probability of the spin transition of the molecule, transferring this information in a dynamic information. For instance if we consider a transition from an $m_S = |5>$ to an $m_S = |4>$, if the probability of the transition is elevated, the dynamic of the transition will be fast and if the probability of the transition is low, the dynamic of the transition will be slow as well. The calculated hysteresis loops are reported in Figure 2.40: the green and the red lines represent the hysteresis for the model with and without the dipolar field, respectively. Coming from strong negative fields, the QTM around zero appears at higher negative fields for the green line (-0.0171 T) with respect to the red one (0.0016 T). As we expected, the dipolar field influences the quantum tunnelling around zero field. No significant effects are instead observed on the steps observed around 0.3 T.

Though this theoretical investigation is still incomplete and almost unusable for a direct comparison with the experimental data, since a narrow, but not negligible, distribution of the orientation of the easy axes must be taken into account, it already provides some interesting information. First of all, the idealised 2D hexagonal model used for the calculation represents the largest effect of dipolar interactions. The broadening observed for the zero field resonance is significant, but still less pronounced than the experimental one, which is significantly broader than the simulated curve without dipolar interactions (see Figure 2.10c). Interestingly, the shape of the XMCD detected hysteresis does not becomes more squared on decreasing the photon flux, in contrast to what observed on $TbPc_2$ films.[85,86] It must however be stressed that our experiments are performed at very low photon-flux, a requirement to preserve the integrity of the molecules and to achieve the sub-kelvin temperatures necessary to investigate the dynamics of Fe_4 species.

Though the mechanism of relaxation of SMMs on surfaces needs further experimental and theoretical studies to be fully understood, the results reported in this chapter clearly show the many challenges we had to face and how demanding has been a detail characterisation of the deposition process for such complex and fragile molecular systems thus highlighting the inherent difficulties that still have to be overcome in order to safely embed those complex molecules in real devices.

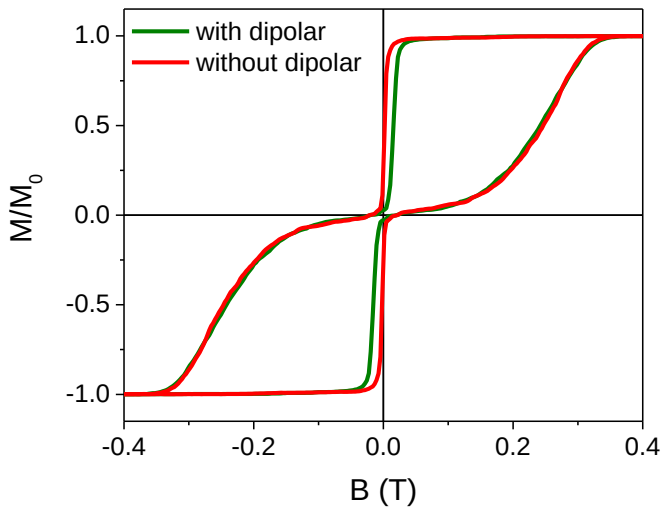

Figure 2.40 Calculated hysteresis loops with (green line) and without (red line) the dipolar field contribution. Parameters: T = 0.5 K; N_{Fe4} = 40, v = 1.2 mT/s

3 Dy-based Single-Molecule Magnets

3.1 Introduction

The extensive study carried out on the deposition of Fe_4 submonolyers presented in the previous chapter highlighted some interesting achievements on the sublimated film of these polynuclear iron-based complexes, but also some drawbacks. In order to find newer and more competitive SMMs candidates to be deposited on surface, we decided to explore potentialities of other systems. Among the SMMs, those containing lanthanides present a large magnetic anisotropy, one of the key feature for the bistable behaviour. The pivotal role of the anisotropy has been widely investigated since Ishikawa and co-workers reported that the bis(phthalocyaninato) Terbium(III) neutral complex $[TbPc_2]^0$ presents SMM behaviour with anisotropy barriers up to 330 K.[18] $TbPc_2$ represents one of the most widely investigated SMM in surface science.[4,20,21,44,87] This molecule, which belongs to the metal double decker family, has a relatively simple general structure: the Tb^{3+} is coordinated by two phthalocyaninato ligands (Pc) rotated of 45° one with respect to the other.[18] One of the key features of this complex is its thermal stability, which allows its deposition by thermal sublimation. Its thermal stability and flatness in shape have favoured STM and STS studies to investigate the electronic structure of $TbPc_2$ by direct visualization of its frontier orbitals.[22,88,89]

The magnetism of films of $TbPc_2$ has been mainly studied by XAS and XMCD, showing the retention of the SMM behaviour in thin films[21,90] and a complex behaviour has been observed. Margheriti *et al*.[21] and in a parallel a study of Stepanow *et al*.[23] demonstrated that in a monolayer of those molecules sublimated on metals (Au or Cu) the dynamics of the magnetisation is faster than in thick films or in the bulk. A possible explanation could be that in the ML coverage the Pc orbitals strongly hybridise with those of the metal substrate. Later it was clearly demonstrated that also the magnetic hysteresis of bulk $TbPc_2$ is strongly affected when the environment is altered with respect to the crystalline phase, being the magnetism in this system dependent also on the intramolecular interactions.[87] Even more recently, it has been shown that a submonolayer coverage of $TbPc_2$ on an MgO insulating layer shows an even enhanced magnetisation hysteresis with respect to the bulk. Moreover, this hysteresis is not present if the substrate is a pristine Ag(100) confirming the tendency of the $TbPc_2$ to hybridise when in contact with metallic surfaces.[24]

Even if $TbPc_2$ presents very appealing characteristics, its erratic magnetic behaviour makes necessary to look for new SMM that are less prone to surface hybridisation. Many neutral and radical lanthanide-based SMMs has been synthesised both as mononuclear and polynuclear complexes.[91–96] Slightly before the beginning of

my thesis, a new Dy^{3+} SMMs has been the object of a collaboration between the Université Européenne de Bretagne in Rennes and the LAMM in Florence. The neutral complex of formula $[Dy(hfac)_3(PyNO)]_2$ (DyNOPy), where $hfac^-$ = hexafluoroacetylacetonate and PyNO = pyridine-N-oxide, is characterised by slow relaxation of the magnetisation at 1.4 K.[27] The presence of the β-diketonate ligands on the molecule is expected to induce a pronounced volatility of the DyNOPy itself. A subsequent characterisation by XPS and ToF-SIMS of a thick film obtained by thermal sublimation, demonstrated the chemical stability of the molecule.[28] Muon spin relaxation experiments (μSR) on this sample showed that the magnetic properties, and in particular the evolution of spin dynamics with temperature, are virtually identical to those of the bulk.[28] These findings were considered extremely important and encouraged us to deepen the investigation and the understanding of the behaviour of this molecule.

The geometry of DyNOPy leads to an intrinsic anisotropy which can be enhanced by an electrostatic contribution. Later the DyNOPy molecule has been slightly modified introducing two electron-withdrawing groups promoting an increase of the anisotropy of the system. A strong electron-withdrawing group g, the nitro group, has been introduced in the para position of the pyridine ring for reasons of steric hindrance. This complex whose structure is reported in Figure 3.1 has the following formula $[Dy(hfac)_3(NOPyNO_2)]_2$ ($DyNOPyNO_2$). The magnetic characterisation of this new complex and its surface deposition based on thermal sublimation are the subject of the first part of this chapter.

In the second part of this chapter we describe and our attempts of depositing on surface a Dy-based single ion magnet presenting a long tetrathiafulvalene-based ligand with several conjugated bonds suitable also for the realisation of multifunctional conductive and switchable magnetic film.[97,98] I want to point out that, while the deposition of Fe_4-based systems on surfaces have been studied since a relatively long time, the study of the deposition of these new classes of SMM systems presented here is almost unprecedented in the surface science field. For this reason in this chapter we describe also the preliminary steps comprising the characterisation of thick films, that is a mandatory activity that must precede deeper studies at the monolayer level.

3.2 Investigating the volatily of the $DyNOPyNO_2$

In this section, we report on the chemical and magnetic characterisation of the film of $DyNOPyNO_2$. The synthesis and the characterisation of the $DyNOPyNO_2$ crystalline material has been performed by Dr. K. Bernot and Dr. X. Yi of the INSA, ISCR, Université Européenne de Bretagne, Rennes. The synthesis of the complex is described in the PhD thesis of X. Yi[99] while the magnetic characterisation of the complex is briefly described in the following.

The structure of $DyNOPyNO_2$ is illustrated in Figure 3.1. Single crystal X-ray studies revealed that $DyNOPyNO_2$ crystallises in P21/n space group. The asymmetric unit contains one $Dy(hfac)_3$ moiety and one NO_2PyNO ligand. The NO_2PyNO ligands connect two equivalent (related by the inversion centre) $Dy(hfac)_3$ moieties to form the binuclear complex $DyNOPyNO_2$ as shown in Figure 3.1.

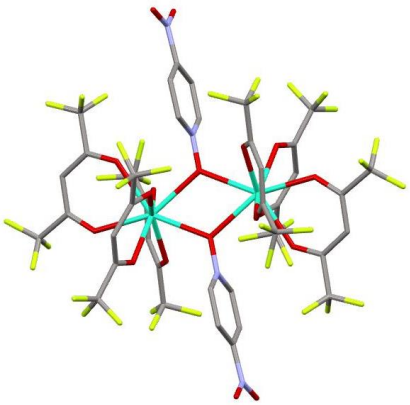

Figure 3.1. Crystal structure of $DyNOPyNO_2$, hydrogen atoms are omitted for clarity. Colour code: Dy = light blue, O = red, C = grey, N = violet, F = yellow.

The Dy^{3+} ion is surrounded by six O atoms from three $hfac^-$ and two O atoms from two NO_2PyNO ligands, therefore it is located in a square antiprism coordination geometry (with idealized D_{4d} symmetry). The Dy-Dy intradimer distance is 4.071(4) Å, while the shortest intermolecular Dy-Dy distance is found to be 10.041(2) Å, demonstrating that each dimer is well isolated. The structure is similar to other Dy dimers of this class, such as DyNOPy.[27,99]

3.2.1 Chemical characterisation of a thick film of $DyNOPyNO_2$

In order to check the possibility to sublimate the complex $DyNOPyNO_2$ we have grown several films on different substrates checking both the chemical integrity and the magnetic behaviour of the complex after the sublimation. The deposition of the molecule on the substrates has been performed by sublimation in HV. For the thermal deposition we have used a homemade Knudsen cell. During the sublimation the powders have been heated up to 415 K reaching a nominal deposition rate of 1.5 Å/min calculated by QCM.

ToF-SIMS characterisation

ToF-SIMS characterisation allows a first direct comparison of the bulk material and the sublimated film. The bulk reference has been obtained by scratching the $DyNOPyNO_2$ powder on a copper foil, while the film of ≈ 33 nm has been deposited on a gold on mica substrate.

In Figure 3.2 the spectrum of the film is compared with that of the pristine powder. The fragmentation pattern of these two samples is almost superimposable, giving a first demonstration of the intactness of the molecular deposit obtained by OMBE. The molecular peak is not present neither in the scratch nor in the sublimated film according to earlier reports based on similar molecules.[28] It is interesting to study the regions corresponding to the peak $[M\text{-}2hfac\text{-}NOPyNO_2]^+$ (1294 m/z) and $[M\text{-}4hfac\text{-}DyNOPyNO_2]^+$ (716 m/z): the isotopic distribution of these two representative peaks (Figure 3.2) for the film and the bulk shows a good agreement with the theoretical pattern. Additionally, the signal of the molecular peak with the loss of an $hfac^-$ ligand $[M\text{-}hfac]^+$ at 1640m/z is weak but clearly visible. Some of the stronger signals of the spectrum are due to the loss of $hfac^-$ and NOPy ligands such as $[Dy(hfac)_3(PyNO)\text{-}F]^+$ (857 m/z) and $[M\text{-}4hfac\text{-}\ NO_2DyPyNO]^+$ (716 m/z). A complete assignment of the peaks in the spectra with their intensity is given in Table 3.1.

Table 3.1. The assignation of the peaks find with ToF-SIMS for the $DyNOPyNO_2$ film. The intensity of each peak is described in the second and third column where w = weak, m = medium, s = strong.

Peak (m/z)	Bulk	Film	Assignment
1778	vw	vw	$[M\text{-}CF_3H]^+$
1746	vw	vw	$[M\text{-}CF_3HO_2]^+$
1641	vw	vw	$[M\text{-}hfac]^+$
1561	w	w	$[M\text{-}hfac\text{-}CF_3N+H]^+$
1436	w	w	$[M\text{-}hfac\text{-}2NO_2\text{-}FH_2\text{-}PyNO]^+$
1372	w	w	$[M\text{-}2hfac\text{-}2NO_2+CO]^+$
1363	w	w	$[M\text{-}2hfac\text{-}2NO_2+OH_3]^+$
1315	mw	mw	$[M\text{-}2hfac\text{-}(CO)_2HO_4+H_2]^+$
1296	mw	mw	$[M\text{-}2hfac\text{-}\ NO_2PyNO]^+$
1280	mw	w	$[M\text{-}2hfac\text{-}\ NO_3PyNO]^+$
1208	w	w	$[Dy_2(hfac)_3(PyNO)(CO)_3C_2F_3\text{-}H]^+$
1175	mw	mw	$[M\text{-}3hfac\ \text{-}F_2O]^+$
1156	w	w	$[M\text{-}3hfac\text{-}F_3O]^+$
1127	w	w	$[M\text{-}3hfac\text{-}F_3NO_2+H]^+$
1016	w	w	$[M\text{-}3hfac\text{-}\ NO_2PyNOCF_3H]^+$
857	s	s	$[Dy(hfac)_3(PyNO)\text{-}F]^+$
799	m	m	$[M\text{-}5hfac\text{-}O]^+$
718	s	s	$[M\text{-}4hfac\text{-}\ NO_2DyPyNO]^+$
704	m	-	$[Dy((hfac)_2(NOPyNO)H_2]^+$
702	m	m	$[Dy(hfac)_2(NOPyNO)]^+$
700	m	m	$[Dy(hfac)_2(C_5H_2NONO)]^+$
672	m	m	$[Dy(hfac)_2C_5H_4NO]^+$
609	w	w	$[Dy_2(PyNO)_2COCH_3CF_2]^+$
530	s	m	$[Dyhfac(PyNO)O_2CH_2F]^+$
513	m	m	$[Dy(PyNO)O_2CH_2F_2]^+$
422	m	m	$[Dy_2N_2OC_4H_2]^+$
340	s	s	$[Dy(PyNO)O_2C_4H]^+$

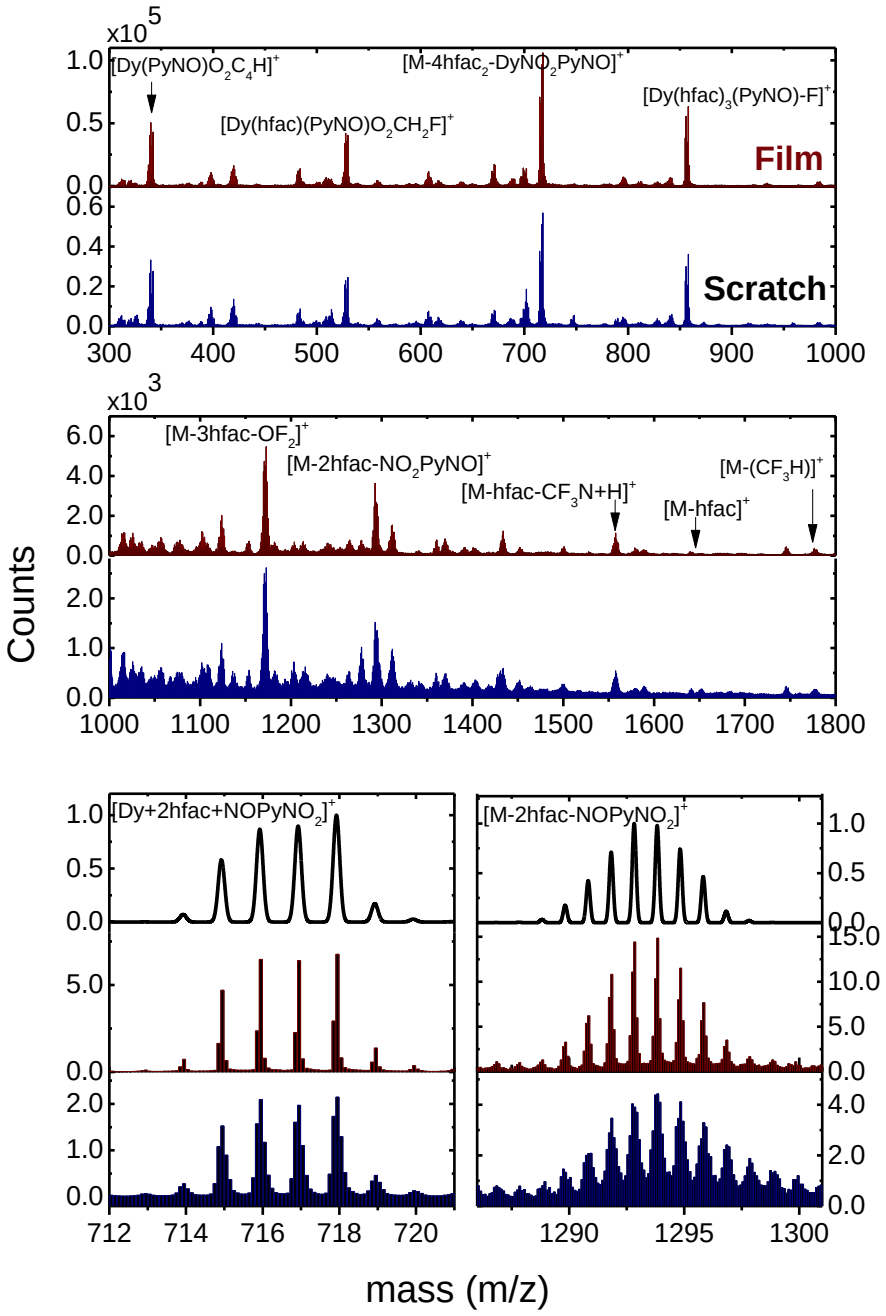

Figure 3.2. ToF-SIMS spectrum of the film (in red) and the bulk reference (in blue) for the $DyNOPyNO_2$ complex. In the bottom part there are two zoomed region. Spectra have been calibrated to $C_2H_2^+$ (m/z = 26.0156), CF^+ (m/z = 30.9984), CF_3^+ (m/z = 68.9952) and [M-4hfac- $DyPyNONO_2$]$^+$ (m/z = 717.9274).

XPS characterisation

In order to confirm that the molecules in the sublimated film are intact, an XPS analysis has been also performed, being this technique capable of verifying both the stoichiometry of the molecular deposits as well as the valence of the elements present on the deposited molecular layers. The bulk reference has been obtained by scratching the powder on a carbon tape, while a film of ≈ 50 nm has been deposited on a gold on mica substrate. We cannot use the same sample as in ToF-SIMS, being this technique partially destructive and because of the risks related to the surface contamination during transfer and preparation phases.

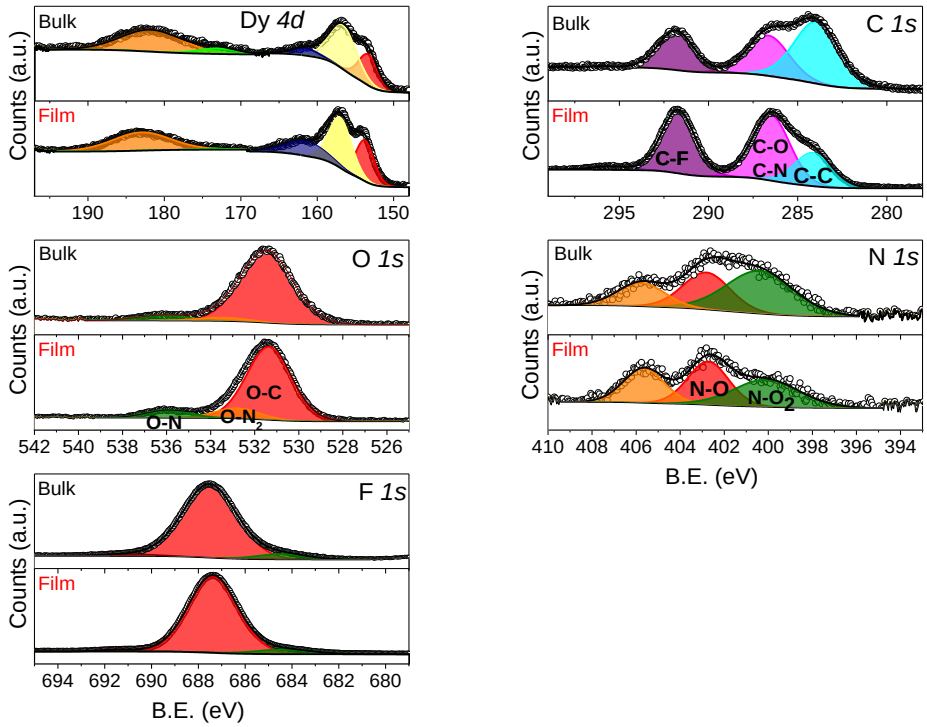

Figure 3.3. XPS region of Dy 4d, C 1s, O 1s, N 1s and F 1s for the DyNOPyNO₂ film and bulk reference. Data analysis was based on a standard method for deconvolution using mixed Gaussian (G) and Lorentzian (L) line shapes (G=30%, L=70%, Gaussian-Lorentzian product) for each component in the spectrum. The inelastic background in the spectra was subtracted by means of the Shirley method.[100]

A quick analysis obtained by comparing the sublimated sample with the pristine one reveals in both samples the presence of the expected elements constituting the $DyNOPyNO_2$. The film shows a marked charging effect due to the low conductivity of the molecular film that has been corrected using as a reference the C_{CF} *1s* peak at 291.8 eV. A careful analysis of the regions of interest evidences that the spectral features of the system are completely maintained after the deposition (Figure 3.4).

The regions Dy *4d*, C *1s*, O *1s*, N *1s* and F *1s* for the bulk and the film are shown in Figure 3.4.

The Dy *4d* region presents, as expected, a complex spectrum due to *4d-4f* interactions. The fine structure and the main peak centred at 157 eV are perfectly in line with a Dy^{3+} system.[101,102] The C *1s* region of the film shows a fine structure which can be clearly assigned to the different carbon atoms according to previous studies on similar complexes:[28,103] at high BE, well separated from the others, a peak attributable to the fluorinated carbon ($-CF_3$) atoms centred at 291.8 eV can be identified. The peak at 286.4 eV is due to the contributions of the ketonic carbon atoms (C=O) and the carbon bound to nitrogen. The component at lower BE is the sum of the aliphatic and aromatic carbons. Table 3.3 compares the experimental and theoretical values for each contribution on the C *1s* peak, showing a good agreement between the two sets of values. The feature at 295.6 eV is due to shake-up signal of the C *1s*. It is not possible to do the same attribution of the peaks for the bulk reference since the carbon tape substrate has a very strong contribution in this region. The analysis of the O 1s region reveals the presence of three distinct contributions attributable to the pyridine N oxide (536.2 eV), the nitro group[104] (533.4 eV) and to the ketonic (531.4 eV) oxygen respectively. The trend of the quantitative analysis of the different contributions in the region is in good agreement with the calculated one (see Table 3.3). The N 1s peak is fitted using three components: one for -NO (402.7 eV), another one for $-NO_2$ (405.7 eV) and a third component at lower BE (400.0 eV). These energy values are in good agreement to what we can find in literature[104,105] for N-oxide and $-NO_2$ groups. The small peak at lower binding energy could be attributed to a radiation damage that is more evident in the bulk sample. The F 1s peak presents a major component at 687.4 eV, due to the fluorine in the $-CF_3$ groups, and a minor component at lower binding energy due to a small radiation damage. A semi-quantitative analysis of the composition of the film according to the integrated peak signals gave the values reported in Table 3.2 that well compares with the theoretical ones.

To resume, the combination of the ToF-SIMS and the qualitative and semi-quantitative XPS analyses allow us to safely confirm that the $DyNOPyNO_2$ film obtained by sublimation in vacuum condition is intact from a chemical point of view.

Table 3.2. Semi-quantitative analysis of the $DyNOPyNO_2$ film and bulk compared with the theoretical values.

	F *1s*	**Dy *3d***	**C *1s***	**O *1s***	**N *1s***
% film	35.7	2.8	46.2	15.3	3.7
% bulk	38.1	2.4	42.7	16.8	3.3
% theoretical	36.0	2.0	40.0	18.0	4.0

Table 3.3 Experimental and theoretical values for each contribution on the C 1s and O 1s peaks in the film of DyNOPyNO₂.

	C *1s*			**O *1s***		
	CF	**C**N/**C**O	**C**C	C**O**	N**O**	N**O₂**
Theoretical %	30.0	45.0	25.0	66.7	11.1	22.2
Experimental %	36.2	42.2	21.5	80.0	8.7	11.3

3.2.2 Magnetic characterisation of bulk and film of $DyNOPyNO_2$

We performed a first magnetic characterisation by *ac* susceptibility. The temperature and frequency dependence of the real and imaginary components of the susceptibility of powders of $DyNOPyNO_2$ are illustrated in Figure 3.4. Strong frequency dependence of the in-phase (χ') and out-of-phase (χ'') components of the magnetisation is observed, in line with what found for similar compounds.[27,99] By fitting the χ'' vs frequency curves with an extended Debye model, the relaxation times τ at the investigated temperatures has been extracted. The Arrhenius plot for the bulk is shown in Figure 3.6: two regimes are clearly evidenced. At high temperature, the relaxation is governed by a thermally activated mechanism, while in the low temperature region the Arrhenius plot flattens suggesting the onset of a different regime. The Orbach relaxation process characterised by an excitation to an intermediate state followed to the deexcitation to the final state, takes place at high temperatures. The second process taken into account is the Raman one that involves the excitation to a virtual state. Though the nature of this mechanism remains unclear and recent studies points towards a key role played by low energy phonon modes,[106,107] it is rather common to take into account the two regimes by considering the relaxation rate as the sum of two contributions with the following equation:

$$\tau^{-1} = \tau_0^{-1} \exp\left(-\frac{\Delta}{k_B T}\right) + AT^n \qquad (5)$$

which gives the following parameters: $\tau_0 = (3.1 \pm 1.5) \times 10^{-10}$ s, $\Delta = 204 \pm 8$ K, $A = 0.037 \pm 0.003$ and $n = 3.93 \pm 0.05$ The value obtained for the barrier of the Orbach process is slightly higher with respect to other dysprosium dimers, and in particular slightly more than the parent compound DyNOPy,[27,108,109] confirming the success of the synthetic design. The Dy^{3+} is a Kramer ion, *i.e.* an ion with an odd number of electrons, which means that the minimum degeneration of the ground state electronic levels is two, a doublet. For Kramer's ions the parameter *n* for the Raman relaxation pathway is expected to be 9, but lower values can be obtained if optical phonons are taken into account.[110–112]

The temperature and frequency dependence of the real and imaginary component of the susceptibility of the $DyNOPyNO_2$ in the form of a ≈ 650 nm thick evaporated film on teflon is illustrated in Figure 3.5. The frequency dependence of the in-phase

(χ') and out-of-phase (χ'') components of the magnetisation is in line to what found for the bulk, though the frequency range has been limited to 1 kHz as the sensitivity of the SQUID detection is necessary for the analysis of a film of SMMs. The relaxation times τ at the different temperatures have been extracted and compared to those of the bulk (Figure 3.6). The superposition of the Arrhenius plot for the bulk and film are in good agreement. The *ac* characterisation suggests that the magnetic behaviour of the molecule is unaltered after the sublimation process.

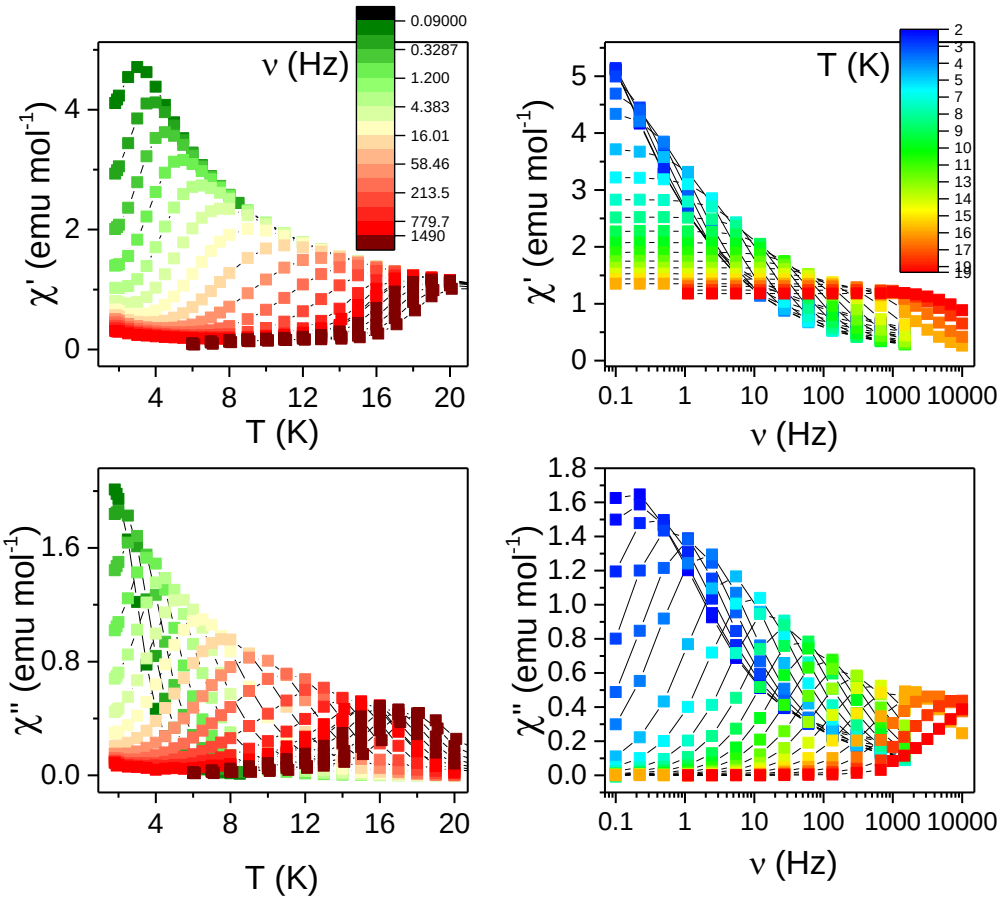

Figure 3.4 Temperature and frequency dependence of the real (χ') and imaginary (χ'') part of the susceptibility of the DyNOPyNO₂ bulk in zero static magnetic field.

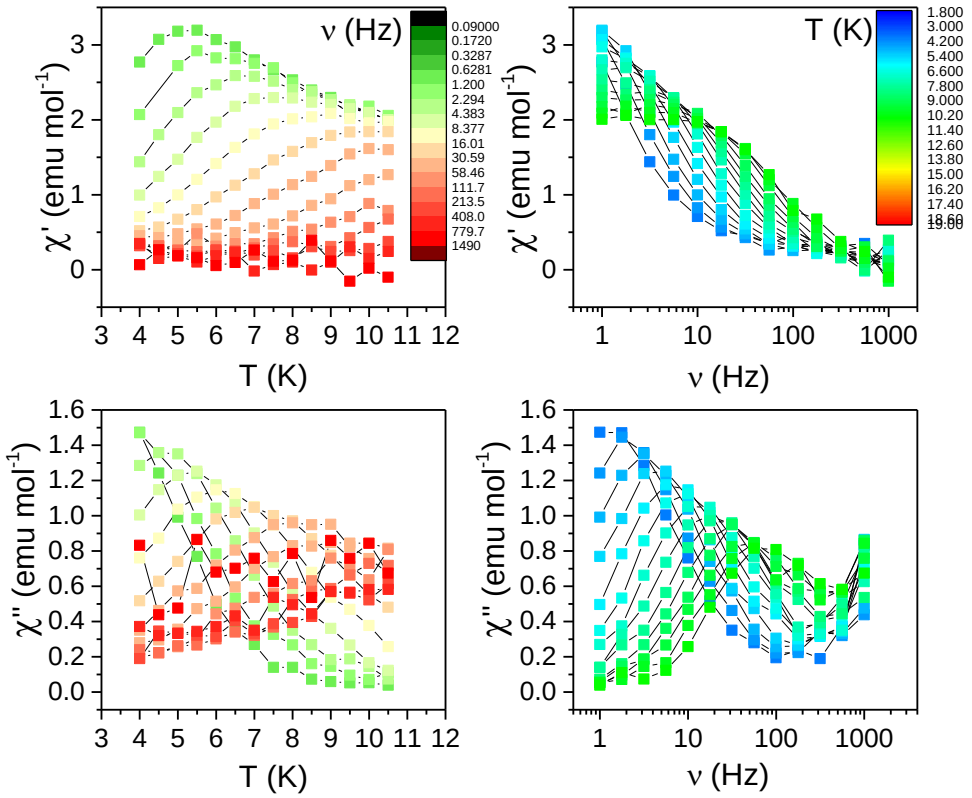

Figure 3.5. Temperature and frequency dependence of the real (χ') and imaginary (χ'') part of the susceptibility of the DyNOPyNO₂ film in zero static magnetic field.

A further magnetic investigation has been performed measuring the dynamics at lower temperature, *i.e.* at 0.5 K (Figure 3.7a). The hysteresis loop recorded for the powder of $DyNOPyNO_2$ shows a butterfly shape typical of the complexes with similar structure like DyNOPy (cf. with Figure 3.7b).[27] This shape can be due either to antiferromagnetic coupling between the two Dy^{3+} or to quantum tunnelling of the magnetisation at the single-ion level.[27,113] The hysteresis loop of the $DyNOPyNO_2$ film is very similar in shape to that of the bulk. The opening of the loop confirms the retention of the SMM behaviour of the $DyNOPyNO_2$ after the sublimation in a wide range of temperatures.

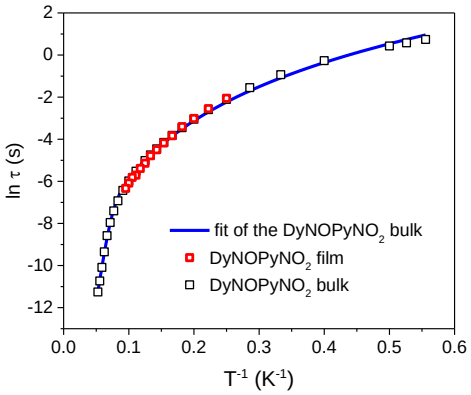

Figure 3.6. Arrhenius plot for the bulk and the film of DyNOPyNO₂.

While the magnetisation curves of compound DyNOPy and $DyNOPyNO_2$ in bulk phase present a similar behaviour featuring a hysteresis although with slightly larger opening for the DyPyNO, the situation is different in the film. The hysteresis on DyNOPy film is not opened (see Figure 3.7b). This means that the dynamics of the sublimated film of DyNOPy is faster with respect to the pristine DyNOPy. We must consider that the differences that we are looking at in Figure 3.7 are very small. Another important comment is that, when deposited on surface, the complex can suffer a distortion of the geometry that, in turn, modify the anisotropy energy barrier (see Section 3.1). This can justify a faster relaxation of the molecular film with respect to the bulk. The difference in the dynamics between DyNOPy and $DyNOPyNO_2$ film can be attributed to a spin-phonon bottleneck effect. The spin–phonon bottleneck effect is a phenomenon due to the lack of an efficient exchange between the spins and the thermal bath mediated by low-frequency phonons, with the resulting slowing down of the relaxation process. Recently the relaxation mechanism of different vanadyl-based molecules revealed a pronounced dependence of the relaxation time by the size of the crystallites, which was associated with a giant spin–phonon bottleneck effect.[114] Being the structure of the two complexes DyNOPy and $DyNOPyNO_2$ slightly different we can suppose that there is a different packing of the film that provoke a different coupling of the molecule with the environment with consequently different relaxation dynamics. However, we cannot obtain unambiguous conclusions on the difference between the dynamics of the film of DyNOPy and $DyNOPyNO_2$.

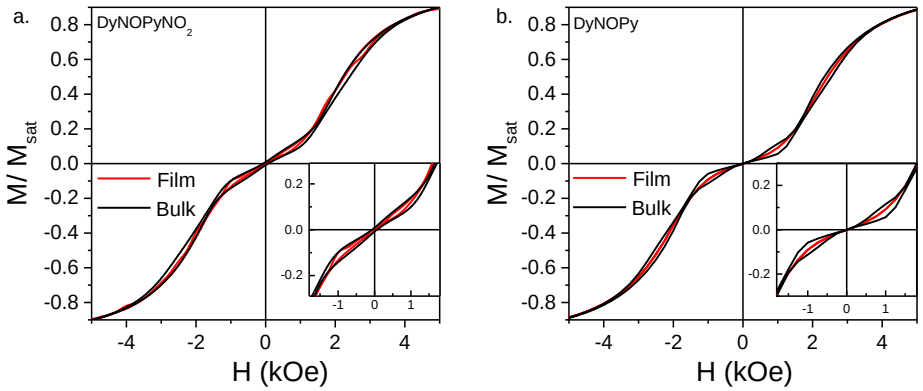

Figure 3.7. Hysteresis loop recorded at 0.5 K for the bulk and the film of $DyNOPyNO_2$ (a) and DyNOPy (b) complexes.

Concluding, $DyNOPyNO_2$ is chemically intact after the sublimation, as demonstrated by XPS and ToF-SIMS. The interesting magnetism of the $DyNOPyNO_2$ powder is retained in the film, as demonstrated by *ac* susceptibly and hysteresis loop. However, the opening of the hysteresis loop in the $DyNOPyNO_2$ film is less pronounced with respect to the bulk.

3.3 Deposition on surface of a Dy-based single ion magnet

The Dy-monomer studied in this chapter is $[Dy(tta)_3(L)]$ (tta =2-thenoyltrifluoroacetonate; L = 4,5-bis(propylthio)-tetrathiafulvalene-2-(2-pyridyl)benzimidazole-methyl-2-pyridine), illustrated in Figure 3.8. The Dy^{3+} ion, in a square antiprism environment, is linked to six oxygen and two nitrogen atoms which belong to three tta^- anions and ligand L, respectively.[29] Crystal packing is governed by a head-to-tail arrangement of L.

The synthesis and the characterisation of $[Dy(tta)_3(L)]$ bulk has been performed in Rennes by the group of Dr. Fabrice Pointillart at the Institut des Sciences Chimiques de Rennes, Université de Rennes, France.[29] The complex is an evolution of the previously studied $[Dy(hfac)_3(L)]$ (hfac = 1,1,1,5,5,5-hexafluoroacetylacetonate; L = TTF-based ligands where TTF = tetrathiafulvalene).[115] This Dy^{3+} monomer shows SMM behaviour in solution, but loose its peculiar magnetic properties in the solid state because of intermolecular interactions (hydrogen bonds). To go beyond this problem, the $hfac^-$ have been replaced by tta^-. It has been demonstrated that this second compound presents SMM behaviour both in solid and frozen solution (see Figure 3.8b).[29] The butterfly-shape hysteresis is clearly visible at 2 K and is appreciable till 4 K, thanks to a very slow magnetic relaxation. The fact that the slow relaxation of magnetisation is visible at 2 K instead of 0.5 K, as for DyNOPy, or the Fe_4, is

dramatically important when the complex is studied as a thin film. In fact, in order to reach 2 K the set-up of magnetic characterisation equipped with a cryostat with pumped ^{4}He is sufficient, while to go below 1 K the use of pumped ^{3}He or a dilution fridge based on ^{3}He-^{4}He mixture is necessary.

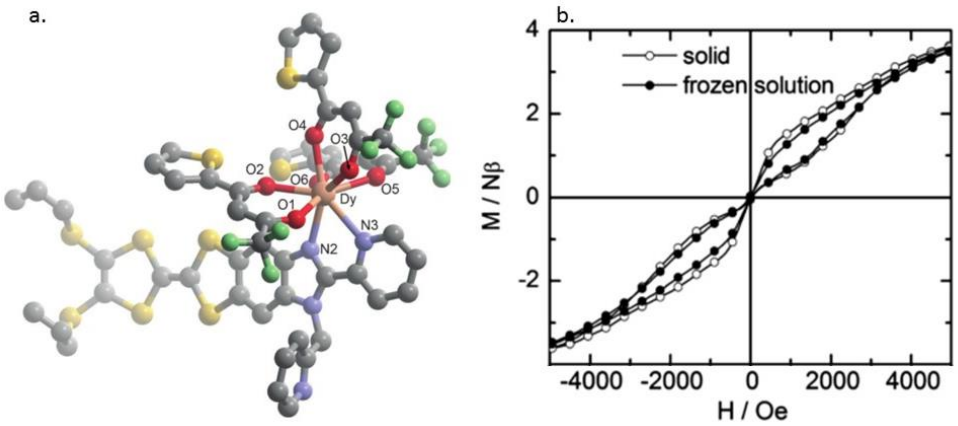

Figure 3.8. (a) Molecular structure of [Dy(tta)$_3$(L)] where H atoms and solvent molecules are omitted for clarity. Green F, yellow S, grey C. (b) Hysteresis loops of the complex measured at 2 K at 150 Oe s^{-1} on a solid sample and in frozen solution.[29]

The chemical structure of [Dy(tta)$_3$(L)] suggests that is a very versatile system for the deposition on surface that could be done by thermal sublimation thanks to the presence of the β-diketonates ligands as well as by a wet chemistry protocol based on the affinity of the bis(propylthiolato) groups with gold surface. The results of the two strategies are described in the following of paragraphs.

3.3.1 Investigating the volatility of [Dy(tta)$_3$(L)]

In order to confirm the hypothesised volatility of this complex a thick films of [Dy(tta)$_3$(L)] has been grown by sublimation in HV and subsequently characterised by XPS and *ac* susceptibility. The system has been sublimated using the home-made deposition chamber described in Section 5.8. During the deposition, the crucible has been held at 430 K, monitoring by the QCM to a rate of ≈ 0.3 Å/min.

XPS have been recorded to check the intactness of the film after the sublimation. The bulk reference has been obtained by scratching [Dy(tta)$_3$(L)] powder on a copper foil, while the film of around 130 nm has been deposited on a gold on mica substrate.

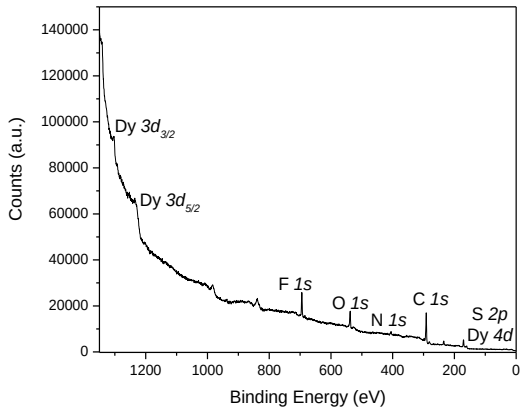

Figure 3.9 Survey XPS spectrum of the evaporated film of [Dy(tta)$_3$(L)] on gold on mica acquired with a standard Al K_α source.

All the expected peaks are visible on the survey spectrum of the film (see Figure 3.9). The C *1s*, S *2p*, Dy *3d*, N *1s* and F *1s* of the evaporated film and of the bulk reference are reported in Figure 3.10 and Figure 3.11. The region 200-150 eV of the spectra in the sublimated film presents both the Dy *4d* and S *2p* peaks. Despite the presence of the S *2p* contribution, the features of the dysprosium in this region are clearly visible. The S *2p* peak is at 163.5 eV, in good agreement to what expected for the sulphur groups in the molecule.[116] The Dy *4d* region presents a complex structure due to *4d-4f* interactions. This fine structure and the main peak centred at 157 eV are perfectly in line with a Dy^{3+} system (cf. Chapter 3.2).[101,102] The C *1s* region of the film shows a fine structure that can be assigned to the different carbon atoms according to previous reports on similar complexes.[28,103] The following contributions are present: fluorinated (292.3 eV), ketonic (288.4 eV), -CN –CS (286.8 eV) and aliphatic and aromatic carbons. The peak of the N *1s* is at 399.7 eV and that of F *1s* at 688.2 eV. The analysis of the O *1s* region reveals a peak at 531.6 eV due to the ketonic oxygen.

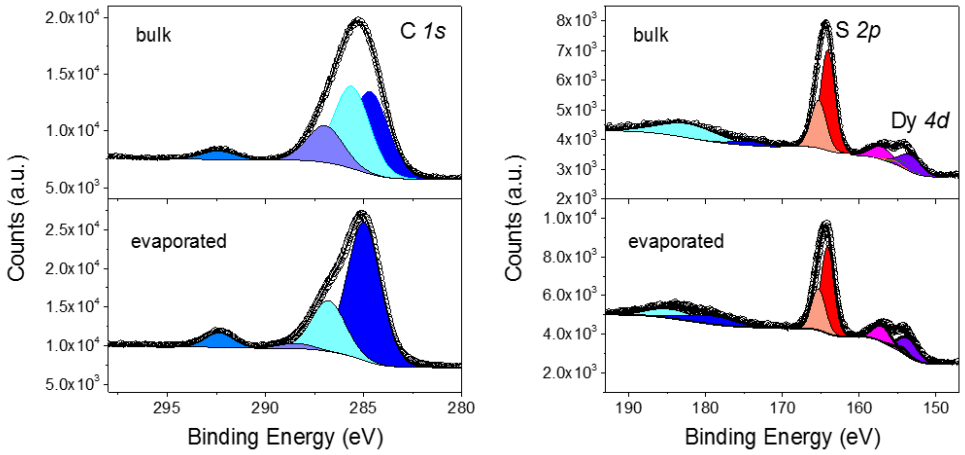

Figure 3.10 C 1s, S 2p, Dy 4f XPS spectra of the evaporated film of [Dy(tta)$_3$(L)] on gold acquired with a standard Al K$_\alpha$ source.

No significant differences are present in the spectra of the sublimated film and of the bulk, except in the case of the carbon region where the discrepancy can be explained by the presence of adventitious carbon on the copper foil used as substrate for the bulk measurements.

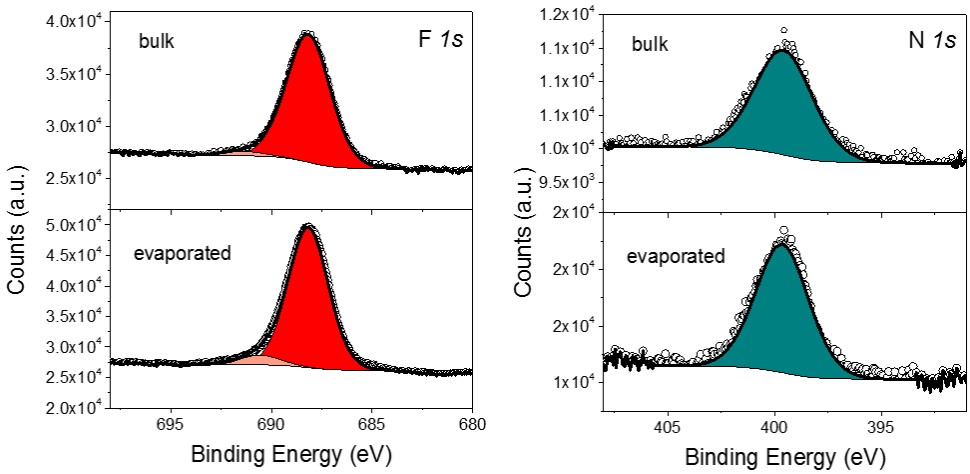

Figure 3.11 F 1s, N1s XPS spectra of the evaporated film of [Dy(tta)$_3$(L)] on gold acquired with a standard Al K$_\alpha$ source..

A semi-quantitative analysis of the peaks is shown in Table 3.4; the C *1s* peak can be effected by a great uncertainity due to the presence of adventitious carbon, so it is not included. The measured composition of the film agrees well with the theoretical values.

Table 3.4 Semi-quantitative analysis of the XPS spectra of the [Dy(tta)$_3$(L)] sublimated film compared to bulk and expected values.

	S *2p*	**Dy *4d***	**N *1s***	**F *1s***
% Theoretical	39 %	4 %	17 %	39 %
% Bulk	38 %	4 %	16 %	42 %
% Film	36 %	5 %	16 %	44 %

For the magnetic characterisation, a thicker film, of ≈ 360 nm has been prepared, in fact a great amount of product is necessary for the ac susceptibility measurements. The substrate used is teflon, that presents a very low diamagnetic response. The frequency dependence of the out-of-phase components of the *ac* susceptibility for the bulk sample is illustrated in Figure 3.12a. Differently with respect to what could be expected by the XPS characterisation, the behaviour of the film is completely different from the bulk, with the loss of the SMM behaviour. However it is not very surprising because, as already discussed in the introduction, it is rather uncommon to find SMM stable face to sublimation. To deepen the understanding of the behaviour of the molecule face to the environment, a dropcast sample of [Dy(tta)$_3$(L)] in CH_2Cl_2 has also been measured. The relaxation of the dropcast has an intermediate behaviour between the bulk and the film. This demonstrates that the loss of the crystalline habitus already perturbs the system in such a pronounced way, enough to modify its magnetisation dynamics.

To sum up, [Dy(tta)$_3$(L)] film seems intact after a first XPS analysis, but its *ac* susceptibility demonstrates the loss of the slow relaxation of the magnetisation after the sublimation.

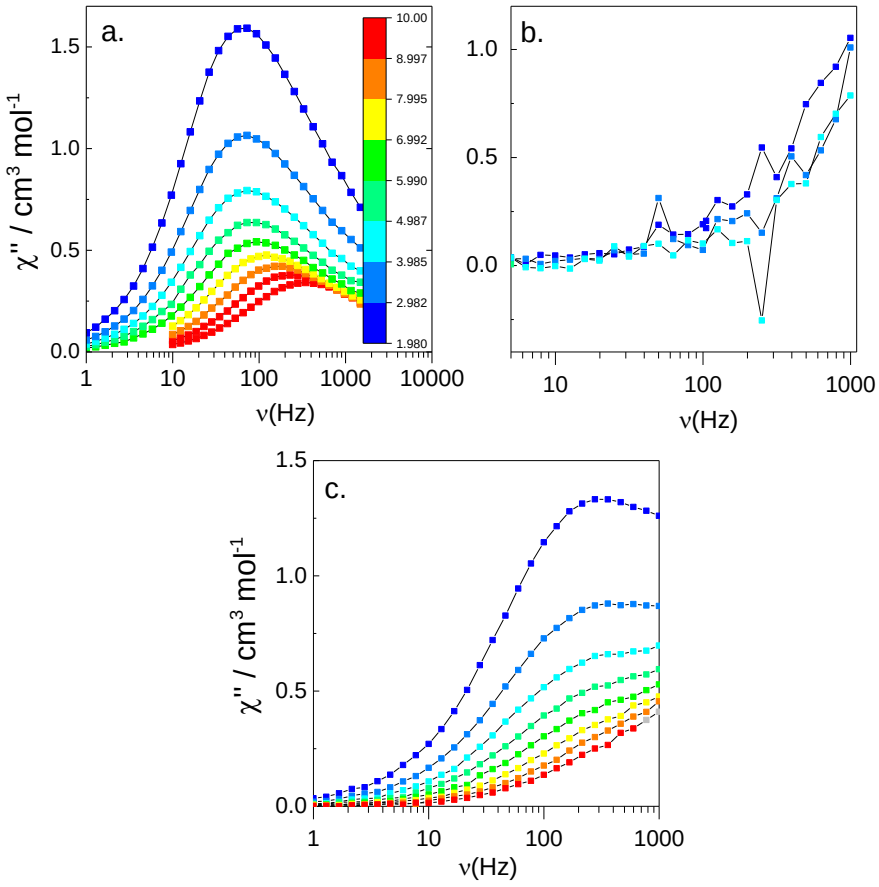

Figure 3.12. Frequency dependence of the χ'' in zero static field for the bulk (a), the film (b), and the dropcast (c) of [Dy(tta)$_3$(L)].

3.3.2 Deposition of [Dy(tta)$_3$(L)] from diluted solution

In the previous chapter, it has been demonstrated that the sublimation pathway to obtain a film of the monomeric Dy complex has not been successful. The presence of many sulphur groups, and in particular the two bis(propylthiolato) groups, could allow the grafting of the complex by self-assembling strategy *via* wet chemistry on a gold substrate. We therefore attempted this deposition strategy. In order to prepare the monolayer film, the gold on mica substrate, after the flame annealing, has been immersed in a solution of 2 mM of [Dy(tta)$_3$(L)] in CH_2Cl_2 for 20 hrs. The substrate has then been cleaned with CH_2Cl_2; all the procedure has been performed in a glove bag filled with nitrogen.

XPS characterisation

The spectrum of the monolayer presents all the peaks expected for the molecule, even if the intensity of the peaks is very low. The position of the signals results analogous to those in the sublimated film illustrated in the previous chapter. The only difference are the sulphur peaks, in fact the S *2p* region shows a marked difference between the bulk sample and the monolayer (see Figure 3.13). The bulk sample in fact presents only one species with the spin-orbit splitting typical of the *p* peaks. For the monolayer spectrum, together with the main peak at 163.3 eV (red colour), a second peak is present at 161.5 eV (blue colour). In line with its lower B.E., the peak is attributed to the sulphur which binds the gold substrate.[117] The area of this peak represents the 30% of the total sulphur peak. Since the total number of sulphur in this molecule is 9, less than 1/3 of the sulphur atoms seems to be bound to the gold surface. This is almost in line with the fact that two sulphur of the bis(propylthiolato) groups have lost their propyl groups and bind to the surface.

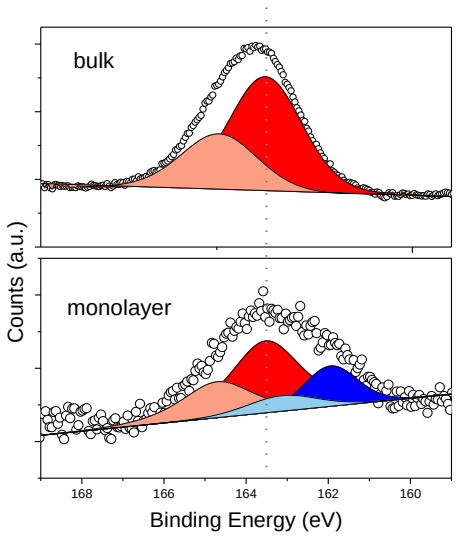

Figure 3.13. XPS spectrum of the S 2p region of the monolayer and of the bulk reference sample of [Dy(tta)$_3$(L)]. Spectra acquired using a standard Al K_α source.

The semi-quantitative analysis of the monolayer of the complex is reported in Table 3.5. The dysprosium is not taken into account due to the difficulties in estimating its intensity at very low coverages because of its peculiar structuration of the peak. The presence of spurious carbon introduced on the surface due to the wet chemistry preparation cannot be excluded, therefore we take into account only the area of nitrogen, sulphur and fluorine for the semi-quantitative analysis. As we can see from this analysis, there is a discrepancy between the experimental and the expected values; the nitrogen and the sulphur are in excess. We supposed two

scenarios to explain this difference. We could hypothesise that the molecule loses one of the β-diketonate ligand because of a partial dissociation process of the molecule in solution. The value expected in this case are reported in line 4 of Table 3.5. An alternative explanation foresees a dissociation process liberating a fraction of ligand L. In that case, we expect to have a partial passivation of the gold surface from the ligand itself. The value of the semi-quantitative analysis that we expect considering that half of the surface is passivated by the free ligand is reported in Table 3.5. These values resemble rather the experimental ones, even if there is still a discrepancy, especially in the N/S ratio. Considering this scenario, we expect to have the 28% of the sulphur bounded to the surface, a percentage in line with what we have obtained experimentally.

Table 3.5 Semi-quantitative XPS analysis of the $[Dy(tta)_3(L)]$ film comparted with the expected values. The lines with grey background represent two possible scenarios for the complex: in line 4 the values for the molecule $[Dy(tta)_3(L)]$ that loose of the tta^- ligand and in line 5 the values for a monolayer film composed at 50% of $[Dy(tta)_3(L)]$ molecules and 50% of L ligands.

	N/S	**F/S**
Theoretical	0.44	1
Experimental	0.64	0.44
Theoretical for $[Dy(tta)_3(L)]$ -1tta^-	0.50	0.75
Theoretical for a film 50% $[Dy(tta)_3(L)]$ + 50% L	0.89	0.50

XAS characterisation

In order to probe the magnetic behaviour of the monolayer of $[Dy(tta)_3(L)]$, also in this case a synchrotron experiment has been requested to overcome the sensitivity issues. XAS/XMCD experiments have been performed at DEIMOS beamline in the Soleil synchrotron in Paris. These experiments have been carried out under a 3 T magnetic field parallel to the X-ray light propagation vector that is normal to the surface of the sample. The cryostat available in this beamline allows to go to temperature as low as 1.8 K, sufficient to probe the dynamics of the magnetisation of this complex. The monolayer has been prepared as described in Chapter 3.3.2., while we used as a reference a dropcast of a CH_2Cl_2 solution of $[Dy(tta)_3(L)]$ on gold on mica.

The XNLD characterisation, reported in Figure 3.14b, has been performed to gain more insight in the organisation of the molecule on the substrate. The XNLD spectrum acquired at the $M_{4,5}$ edge of the dysprosium does not present any significant signal, therefore we can deduce that the molecules do not have a preferential orientation on the gold substrate.

The XAS spectra recorded at the $M_{4,5}$ edge using circularly polarised light for the monolayer sample is illustrated in Figure 3.14. The shape of the curves are in good agreement to other similar systems.[118,119] The monolayer presents a strong XMCD signal of about 155%.

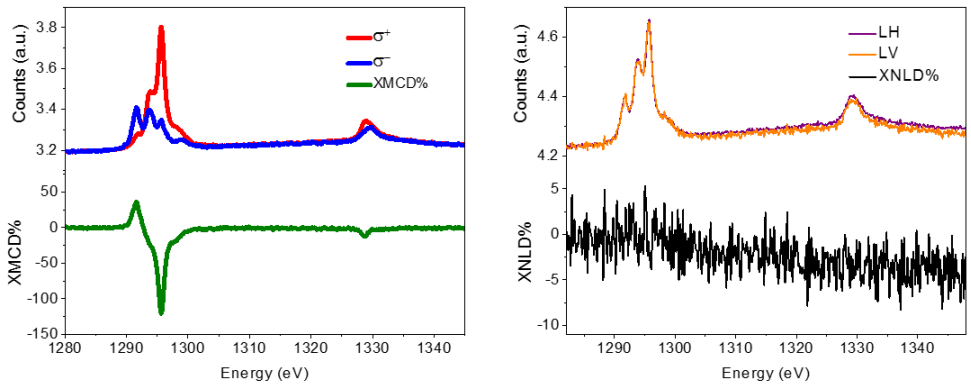

Figure 3.14. (Left) XAS and XMCD and (right) XAS and XNLD spectra of the monolayer of [Dy(tta)$_3$(L)] on gold on mica.

The variation of the XMCD acquired at its maximum amplitude with respect to the magnetic field, shows an opening of the hysteresis loop both for the bulk sample and for the monolayer (see Figure 3.15). The loop is not well resolved around zero since in this region the S/N ration is low, due to the acquisition set-up. However, the only fingerprint of the molecule on the hysteresis is around zero, and we cannot probe that zone. Even if the hysteresis loop of this complex does not represent a fingerprint, such as that of Fe_4, the clear opening that we see is uncommon at 1.8 K and, for this reason, promising. Therefore, the XMCD results demonstrate that the fraction of intact molecule present on the surface still features magnetic bistability.

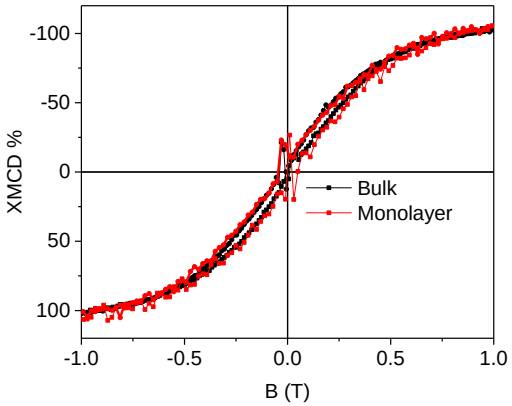

Figure 3.15. Hysteresis loops acquired by monitoring the field dependence of the XMCD signal at 1295.7eV. The red curve is the monolayer sample of [Dy(tta)$_3$(L)], while the black one is the bulk reference of [Dy(tta)$_3$(L)].

To sum up, the XPS characterisation of the sulphur region showed the chemical bonding of the complex to the surface, however the semi-quantitative analysis suggested a partial dissociation of the complex in solution. The XMCD characterisation of the film demonstrated the retention of the magnetic bistability after the deposition on surface. This suggests that a relevant fraction of the molecules are bonded to the surface and preserve their SMM behaviour, showing that the deposition by wet chemistry can be a valuable strategy to transfer these molecules at the nanoscale.

4 Assembling molecular qubit candidates on surface

While the previous two chapters have been focused on magnetic molecular systems characterised by anisotropy and large spin, we present here the research we have carried out on paramagnetic molecules with $S = ½$ featuring long spin coherence times and therefore of interest for their potential application as qubits for quantum computation. As already briefly described in the introduction, qubits based on molecular spins can be organised on surfaces and the interaction among them can be tuned via a rational synthetic design. Thus, they represent a valuable alternative to be explored with respect to other electron-spin-based qubits like nitrogen vacancies in diamond[40,41] and impurities in silicon and silicon carbide.[120]

Magnetic molecules have been studied as possible building blocks of quantum computing since the beginning of this century.[7,121,122] Christou *et al.* already in 2002 proposed a supramolecular dimer of Mn_4 SMM with antiferromagnetic coupling between the two clusters as a component for quantum devices.[121,123] However, only more recently a systematic evaluation of potentialities of molecular systems for quantum computation have been started. The Cr_7M (M = Ni, Mn) molecules are polynuclear magnetic rings where the magnetic properties can be tuned by changing the M metal atom: Cr_7Ni has an $S = 1/2$ while Cr_7Mn has an $S = 3/2$. These complexes were proposed as possible qubits and were investigated by pulsed EPR showing relaxation times, T_m, significantly exceeding the duration of their coherent manipulation.[124–126] The coherence time of these rings seems to be strongly affected by the coupling to the nuclear momentum of the protons and by the conformational rigidity of the chemical structure. Therefore the structure of these molecules has been engineered in order to optimise their properties in term of long spin coherence time.[127] The Cr_7Ni rings have been linked together tuning the coupling between their spin choosing the desired linker, thus opening perspectives in the control of the entanglement of spin-based qubit.[128–130] The molecular structure has also been modified to foster the linking to the gold substrate by wet chemistry. The characterisation of the submonolayer film showed that the molecular structure is intact, but the magnetic properties of the system are not fully retained after the grafting.[131] This result is not unexpected, since, as we observed and discussed in the previous chapters, the deposition on surfaces demands a pronounced stability not often encountered in polynuclear magnetic molecules. Relaxation times comparable to that of Cr_7M have been obtained for a nitronyl nitroxides (NitR) radical optimised for the chemical grafting on surface.[132]

Longer spin coherence times have been recorded on metal complexes having only one metallic centre.[133–135] Warner *et al.* studied a commercial phthalocyanine, CuPc, that has the advantage of being very stable with respect to thermal sublimation.[133] Thus, the separation of the molecular qubits can be properly tuned by inserting in the molecular film a diamagnetic matrix. Nuclear spin-free vanadium complexes displayed outstanding long coherence times.[134,136] Zadrozny *et al.*[136] showed that, when magnetic dilution is made in a nuclear spin-free solvent such as CS_2, T_m approaches one millisecond at low temperature, indicating that molecular spin systems can be as performant as extended inorganic structures.

In this frame, vanadium-based molecules with long spin coherence times have been studied in the LaMM laboratory. During the last part of this PhD work two vanadyl complexes have been investigated, $VO(dpm)_2$ and VOPc (where Pc = Phthalocyanine), both molecules are volatile and can be grown as a thin film in UHV.[137,138] Both complexes present a typical square pyramidal coordination with a short V=O double bond. The strongly axial ligand field produced by the short V=O bond removes orbital degeneracy with the d_{xy} orbital being the lowest in energy and the only one to be half occupied. The scheme in Figure 4.1 represents the orbital structure of the V^{4+}. Vanadyl systems are therefore well described by a spin $S = 1/2$ with slightly anisotropic g tensor close to the free electron value.

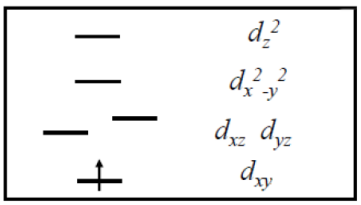

Figure 4.1 Schematic representation of the V^{4+} orbitals in vanadyl complexes.

4.1 Study of the processablity of $VO(dpm)_2$

The first vanadyl-based system that has been investigated in this thesis work has been the $VO(dpm)_2$, those structure is illustrated in Figure 4.2. This vanadyl complex has been selected because the strong V=O bond is expected to increase the rigidity of the coordination sphere with a reduction of spin–lattice relaxation efficiency. The $VO(dpm)_2$, presents a typical square pyramidal coordination with a short V=O double bond (1.59 Å *vs.* an average of 1.964 Å for the V–O single bonds), as expected for the members of this family.[139] As already discussed in the previous chapters, the presence of the β-diketonate ligands favours the volatility of the molecule.

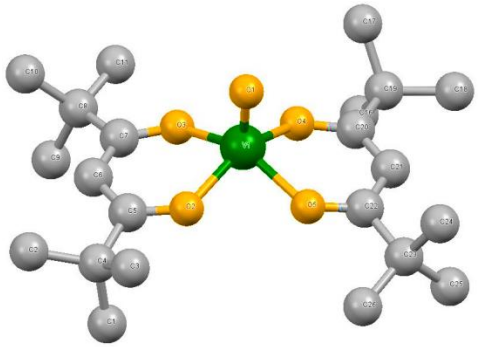

Figure 4.2 Ball and Stick representation of the $VO(dpm)_2$; colour code: C = grey, O = yellow, V = green.

This simple mononuclear complex of vanadium(IV) has been investigated by the combination of *ac* magnetic susceptometry to study spin–lattice relaxation and pulsed EPR spectroscopy to characterise the spin coherence.[140] Given the lack of an isostructural non-magnetic compound, pulsed EPR measurements have been carried in frozen solutions and have provided T_m values. The T_m of the $VO(dpm)_2$ is compared to that of others complexes with long spin coherence in Figure 4.3. $VO(dpm)_2$, though the presence of many hydrogen atoms and thus not yet optimized for coherent manipulation of the spin state, presents state-of-the-art phase memory times. Its relaxation time is in fact an order of magnitude longer than those of optimised Ni_7Cr[127] and slightly longer to those of CuPc.[133] On the contrary the relaxation time T_m of $(PPh_4)_2[V(C_8S_8)_3]$ in CS_2 approaches one millisecond at low temperature,[136] thus better with respect to $VO(dpm)_2$. Interestingly, the remarkably long coherence of this molecule is rapidly lost on increasing temperature because the spin–lattice relaxation acts as limiting factor for T_m.

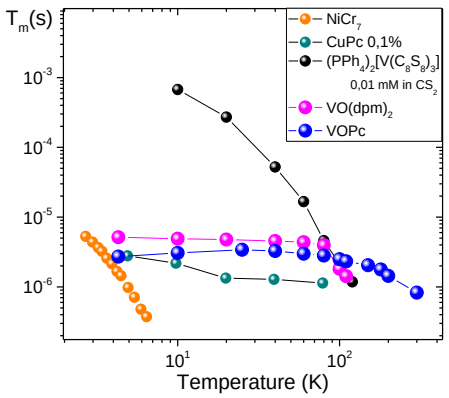

Figure 4.3 T_m relaxation time vs. temperature of different molecular complexes.

The *in situ* morphological and spectroscopic characterisation of a monolayer deposit of $VO(dpm)_2$ on Au(111) is the focus of this chapter and the results obtained suggest that the molecules are intact on the surface, making these simple units potential candidates as molecular qubit individually addressable by scanning probe techniques.

4.1.1 Deposition on Au(111) and *in situ* characterisation of $VO(dpm)_2$

STM characterisation

The ML and sub-ML deposition and characterisation of $VO(dpm)_2$ films have been performed *in situ* in the CeTeCS platform (see Section 5.8.). The STM characterisation has been performed at 30 K. The substrate used for this study is an Au(111) single crystal. Before the preparation of the sample, the gold has been freshly cleaned through sputtering (2 μA, 1 keV) and annealing (720 K). Considering that $VO(dpm)_2$, like other β-diketonates, shows high volatility (see Chapter 2), the sublimation has been performed in a dedicated preparation chamber with a base pressure of 1×10^{-7} mbar. As for the $Fe(dpm)_3$, in order to have a ML/sub-ML coverage, there is no need to heat the powder; the sample is just exposed to the vapour pressure of the complex.

A subML coverage of $VO(dpm)_2$ is then obtained exposing the clean gold sample to the vanadyl pressure (see Figure 4.4). The $VO(dpm)_2$ does not strongly interact with the surface, organizing spontaneously in extended islands, even if some isolated objects are observed at the kinks of the Au(111) herringbone reconstruction, which are known to be highly reactive sites. The islands present an ordered structure with regular boundaries maintaining the herringbone modulation of the gold substrate. The resolution of the image is not enough to address the individual units. The height of the $VO(dpm)_2$, measured and mediated on several zones, is 0.27 ± 0.02 nm. This value is in good agreement with that found in other similar metal complexes with dpm^- ligands, such as $Fe(dpm)_2$ (see Chapter 2).[56,68]

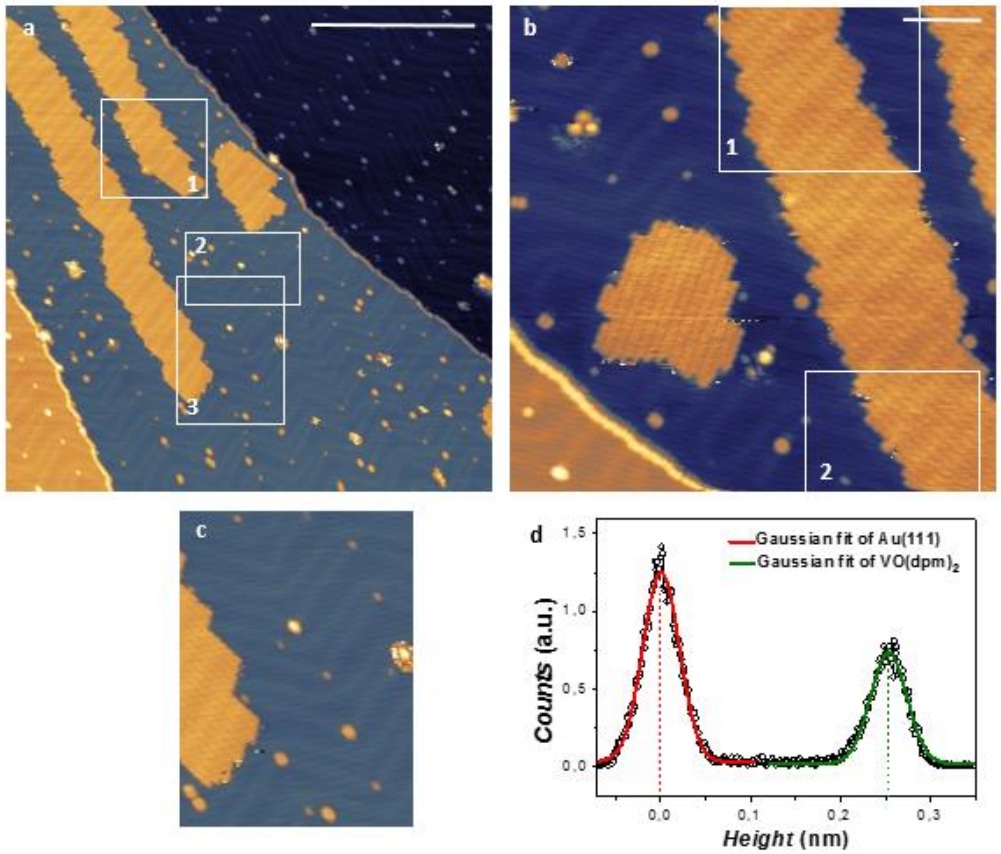

Figure 4.4 (a, b) STM images of a sub-monolayer deposition of $VO(dpm)_2$ measured at 30 K. Bias = -2 V (empty states), I = 5 pA. The scanned regions are 150 × 150 nm^2 in (a) and 60 × 60 nm^2 in (b) and the bars correspond to 50 nm and 10 nm, respectively. The zones into the frames are the ones used for the evaluation of the height distribution. c) Enlarged view of zone 3 in (a). d) Height distribution.

Exposing the surface to the $VO(dpm)_2$ atmosphere for a longer period leads to the formation of a complete monolayer (see Figure 4.5). The regularly packed molecules still reveal the herringbone structure underneath.

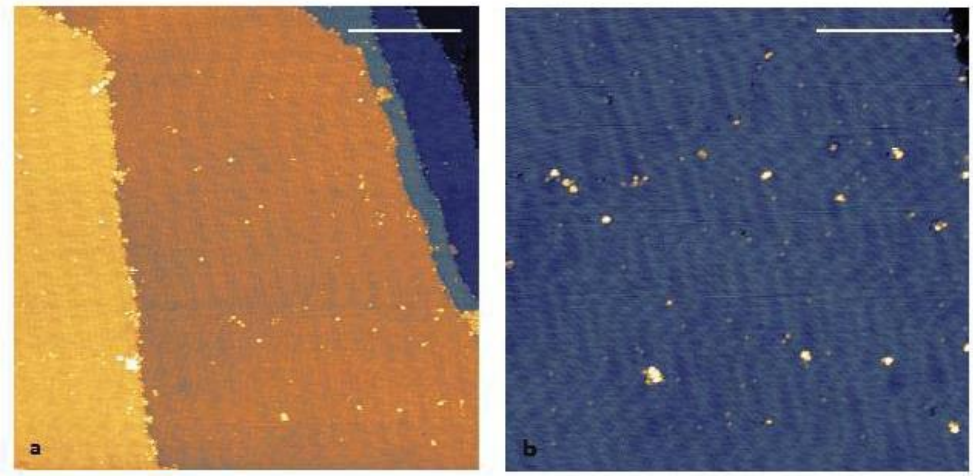

Figure 4.5 STM image of a monolayer deposition of $VO(dpm)_2$ measured at 30 K. Bias = -2 V, I = 5 pA. a) 200 × 200 nm^2 region. b) 100 × 100 nm^2 region, zoom of the precedent. The scale bars are 50 nm (a) and 30 nm (b).

XPS characterisation

In order to investigate if the molecules are intact after the deposition, we performed the XPS analysis of a monolayer of $VO(dpm)_2$. Moreover, the XPS characterisation of a thick film prepared *ex situ* has been used to test the stability of the complex in air.

The thick film has been prepared in a home-made evaporation chamber, and transferred to the XPS chamber using a glove bag filled with nitrogen. The sublimation has been performed on top of a polycrystalline Au film evaporated on muscovite mica. Before the sublimation a hydrogen flame annealing procedure has been adopted in order to clean the *ex situ* prepared substrate. The deposition was performed using the same evaporator as for the monolayer coverage but the powders were heated at 373 K. The comparison of the STM and XPS characterisation of an *in situ* monolayer deposition performed by heating the powders (at 373 K, where a rate is observed by QCM) or leaving them at room temperature, proves that there is no difference between the two deposition procedures.

The monolayer was subjected to differential charging and the Au $4p_{3/2}$ peak present the same energy shift as the main ones of the molecule (O *1s*, V *2p*, C *1s*). Performing the calibration using the Au $4p_{3/2}$, the position of the main peak of C *1s* was 285.4 eV. In order to use the same calibration for the thin and the thick film, being the Au $4p_{3/2}$ not visible, the methyl C *1s* at 285.4 eV signal has been used as a reference to correct the charging effect. XPS data analysis has been performed by removing the inelastic background by means of the Shirley method[100] and then applying a deconvolution of the experimental spectra using mixed Gaussian and Lorentzian line-shapes for each component in the spectra. In the case of V *2p* component the adopted

method resulted in line with previous studies.[141] The background for the O *1s* peak was obtained by subtracting also the contribution of the Au *4p 3/2* peak at 547 eV.

The XPS spectra of a monolayer of $VO(dpm)_2$ is reported in Figure 4.13. The O 1s peak has been fit considering two components. The peak at 532.1 eV has been attributed to the oxygen atom of the dpm^- ligands ($O_{C=O}$), while that at 531.3 eV to the oxygen of the vanadyl group ($O_{V=O}$). The latter value is in good agreement with what is reported in literature for similar systems, like VOPc on Ag(111).[142,143] The ratio of the area of the two components is close to 1 : 4, as expected for the stoichiometry of the molecule, thus proving the integrity of the complex on surface. The carbon C 1s peak presents three components at 287.2 eV, 285.4 eV and 284.6 eV attributed respectively to the carbonylic carbon, methyl carbon while the third component can be associated with –CH and -CC carbons. However, the most informative peak is the V 2p which provides specific hints on the oxidation state of this element and thus on possible interaction with the metal surface and their effect on the $S = 1/2$ character of the molecule. The V $2p_{3/2}$ peak is at 516.4 eV, and its distance from the O 1s, $\Delta E(O\ 1s_{V=O}\text{-}V\ 2p_{3/2})$, is 14.9 eV, comparable to VOPc monolayer and multilayers ($\Delta E(O\ 1s_{V=O}\text{-}V\ 2p_{3/2}) = 14.6$ eV) on Ag(111).[143]

A semi-quantitative analysis of the regions above described gives the following composition C = 81 ± 4%, O = 16 ± 1%, V = 2.6 ± 0.6% which well compares with the theoretical values (C = 78.6%, O = 17.9%, V = 3.6%).

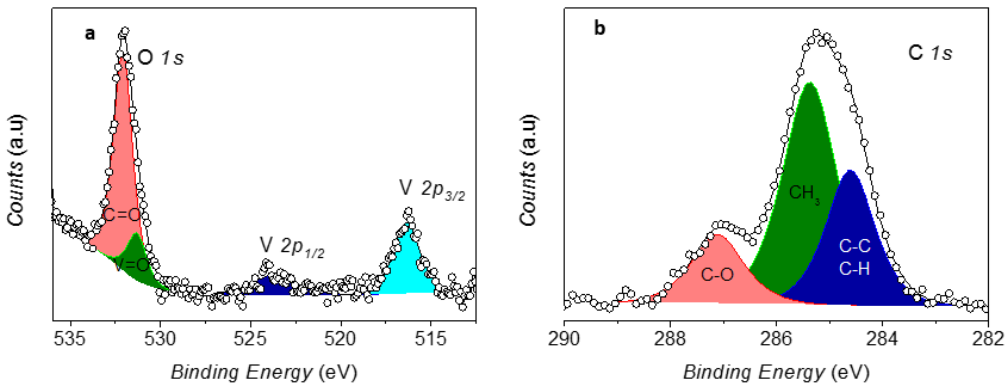

Figure 4.6 XPS spectra of a monolayer coverage of $VO(dpm)_2$ on Au(111). The O 1s and V 2p regions are shown in (a) while the C1s region in (b). Filled area and lines represent the best fit components and resulting spectra, respectively. Spectra acquired with a monocromatic Al K_α source.

We notice that $VO(dpm)_2$ films resulted somehow instable in air: *ex situ* prepared thick films of about 150 nm showed a partial surface oxidation as suggested by the decrease in the $\Delta E(O\ 1s\ _{V=O}\text{-}V\ 2p_{3/2})$ value accompanied by a progressive shift of the V *2p* peak (Figure 4.7).

These observations indicate that, by operating in controlled condition most of the $VO(dpm)_2$ molecules can be deposited intact on the surface. The deposited

molecule are also expected to preserve their paramagnetic character, since the only occupied d orbital, d_{xy}, is expected to lie flat with limited overlap with the orbitals of the gold substrate. A similar scenario was observed for copper(II) phthalocyanine molecules that are known to retain their unpaired electron in the dx^2-y^2 orbital.[144] In the vanadyl derivative VOPc the metal atom is slightly above the plane of the equatorial oxygen atoms; the distance of the metal ion from the surface is therefore further increased thus reducing the interaction with the substrate. It is thus not surprising that synchrotron-based experiments on monolayers of VOPc on Ag(111)[143] detected a substantially unchanged magnetism of the $S = 1/2$ of V^{4+} compared to thicker films. It is therefore reasonable to envisage that $VO(dpm)_2$ molecules retain their paramagnetic nature when in contact with the gold substrate. This system represents therefore an appealing alternative to the use of N-donors phthalocyanine- and porphyrin-based systems for deposition on surfaces, though the instability of the $VO(dpm)_2$ films face to air must be taken into account.

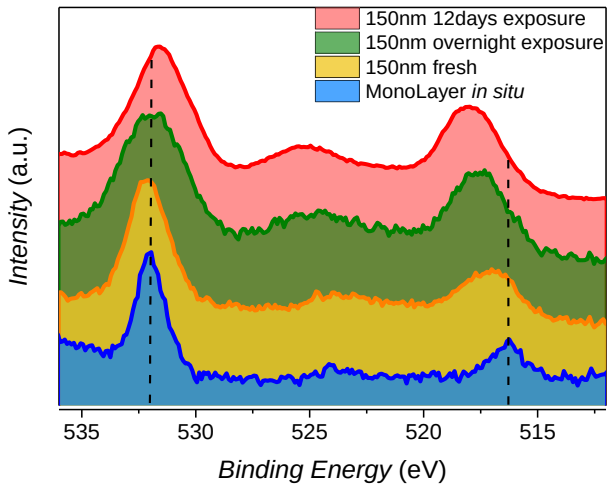

Figure 4.7. Comparison of O 1s and V 2p XPS spectra of the monolayer and thick film. The thick film of 150 nm was prepared ex situ and transferred into the XPS chamber using a glove bag filled with nitrogen; the monolayer was prepared and kept in situ. The time-dependence of the exposure to air is reported.

4.2 Towards the study of the quantum coherence at a single-molecule level

The study of the deposition of $VO(dpm)_2$ was the first step of the challenging project focused on the study of molecules with long-coherence time in a 2D material presenting different environment. We decided to move to the VOPc molecule for different reasons. The VOPc is volatile, as $VO(dpm)_2$, but is stable in air and is a

semiconductor, a technologically relevant characteristic.[145] A recent study on the magnetic relaxation of the VOPc carried out in our laboratory has shown remarkably long spin coherence time also for this N-coordinated vanadyl complex.[146] The relaxation times of this molecule are in fact comparable with those of $VO(dpm)_2$, as shown in Figure 4.3. Moreover, the possibility to dilute the paramagnetic molecules in a matrix of isostructural but diamagnetic TiOPc molecules has allowed to investigate the spin dynamics in a wider temperature range, *i.e.* above the melting point of the frozen solution. This study revealed a remarkably long T_m at room temperature also in high concentration and the possibility to coherently manipulate the spins at room temperature.[146] Of relevance for this thesis is the flatness of the molecule that makes it an ideal candidate to perform an individual molecule characterisation by scanning probe microscopy and spectroscopy.

The VOPc deposition has been therefore investigated with the aim of studying the relaxation time of the molecule on surface. No information are in fact available on the effect of surface confinement on the dynamics of isotropic $S = 1/2$ systems, which differs significantly from that originated by magnetic anisotropy in Single Molecule Magnets. The measurement of the relaxation time of magnetic atoms or molecules can be indeed performed by XMCD, as illustrated in Chapter 2. Recently, individual holmium atoms absorbed on ultrathin MgO(100) layers on Ag(100) have shown magnetic remanence up to 30 K and a relaxation time of 1500 seconds at 10 K.[147] However this type of investigations allows the characterisation of very slow magnetisation dynamics (with relaxation times > 10 s) and they are collective investigations. The study of relaxation times of individual magnetic molecule would be interesting in order to probe the variation of the relaxation times with the environment, a crucial point for the quantum computation. Relaxation times of an individual atom, molecule or nanostructure can be investigated using scanning probe techniques.[148–150] Loth *et al.* used an STM with a pump-probe scheme and a spin-sensitive contrast mechanism to measure electron spin relaxation times of individual Fe-Cu dimer with nanosecond time resolution.[151] B.W. Heinrich *et al.* measured a relaxation time of $\tau \approx 10$ ns on a paramagnetic molecule on a superconducting substrate.[150] A further step was done combining a pump probe system with femtosecond pulses of circularly polarised light.[152] With this setup, they were able to resolve coherent spin dynamics on the picosecond timescale in semiconductor heterostructures. The coupling of the spatial resolution of an STM with the energy resolution of an Electron Paramagnetic Resonance (EPR) has made possible to measure the EPR spectra of an individual iron atom on a magnesium oxide film.[153] Our study of the relaxation time of the VOPc is in the wake of these promising studies.

The structure of the VOPc is illustrated in Figure 4.8. VOPc is a nonplanar metal-phthalocyanine in which the vanadyl ion VO^{2+}, coordinated by four nitrogen donor atoms of the dianionic phthalocyaninato ligand, points out of the plane of the ligand. The VOPc presents a distorted square pyramidal coordination with the metal slightly

above the basal plane (0.575(1) Å).[154] The metal form a short double bond with the oxo-ligand having a V=O distance of 1.580(3) Å.

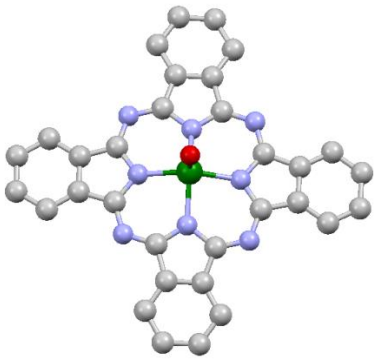

Figure 4.8 Ball and stick representation of the VOPc structure; colour code: C = grey, V = green, N = light blue.

The VOPc has been deposited by thermal deposition on several metallic surfaces[143,155,156] and on HOPG.[155–157] At monolayer level, the VOPc can lay with oxygen-up or oxygen-down configurations (see Figure 4.9) depending on the reactivity of the surface.[143,155] For instance, the chemical interaction of the oxygen of the V=O with the Si(111) favour the oxygen-down configuration of the VOPc molecular layer.[143] A similar behaviour has been observed for VOPc grown on Ni(111).[155] Adler *et al.* demonstrates by XPS that the vanadium undergoes a partial transfer charge at the Ni(111) interface, depending on the oxygen-down configuration. They completely prevent the charge transfer by the introduction of a graphene intermediate layer.

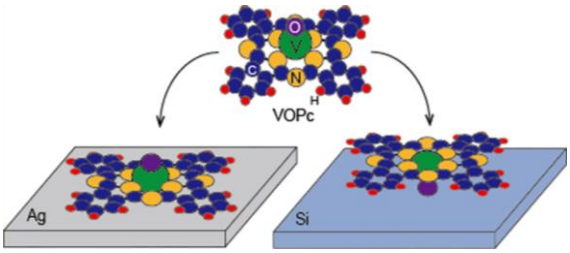

Figure 4.9 The VOPc molecule lays with oxygen-up configuration of Ag(111) and with oxygen-down configuration on Si(111)-(7 x 7).[143]

Preventing the charge transfer between the V^{4+} and the substrate makes the graphene an interesting substrate for our purpose. This characteristic is of crucial importance, otherwise the oxidation state of the vanadium is altered, modifying the paramagnetic $S = ½$ system. Moreover, as we are interested in studying the spin coherence time, two other aspects of this substrates must be evidenced: i) it acts as a decoupling layer from the conduction electrons of a metallic substrate that are

expected to accelerate magnetic relaxation; ii) the small contribution of nuclear spins in the substrate is expected to increase the spin coherence.

4.2.1 Characterisation of the graphene substrate

The graphene grown on silicon carbide (SiC) used for this experiment has been produced by Dr. E. Vélez-Fort and Dr. A. Ouerghi in the Laboratoire de Photonique et de Nanostructures (CNRS-LPN, France). The graphitisation from SiC is one of the few synthetic method to obtain large-area and high-quality epitaxial graphene.[158,159]

The large-area epitaxial graphene is grown on off-axis 6H-SiC(0001). During the growth process (schematised in Figure 4.10), the substrate is heated to 1820° in an 800 mbar argon atmosphere. The preparation method used here is similar to that described by Lalami *et al.* [159] The silicon has a lower sublimation temperature with respect to the carbon thus it starts to sublime enriching the surface in carbon. The carbon atoms still on the surface start the growth process forming the first carbon layer (the buffer layer). If the sample is maintained at high temperature, a second layer starts to grow, that will be the new buffer layer. The heating of the sample allows the reorganisation of the graphene layer. The suggested growth process is illustrated in Figure 4.10 right. The graphene starts its growth in the proximity of nanofacet regions consisting of step edges, the more reactive site of the substrate. The carbon atoms then diffuse parallel to the step edge. The diffusion of the C atoms perpendicular to the step edges toward the terrace regions may initially be energetically less favourable, resulting in a high ribbon density. Nevertheless, at higher annealing temperatures, these ribbons coalesce and gradually propagate laterally toward the centre of the terraces, before generating a second graphene layer. This growth process results in a large area epitaxial graphene on SiC with a small amount of bilayers. The obtained graphene has an intrinsic n-doping due to the charge transfer from the SiC substrate.[160]

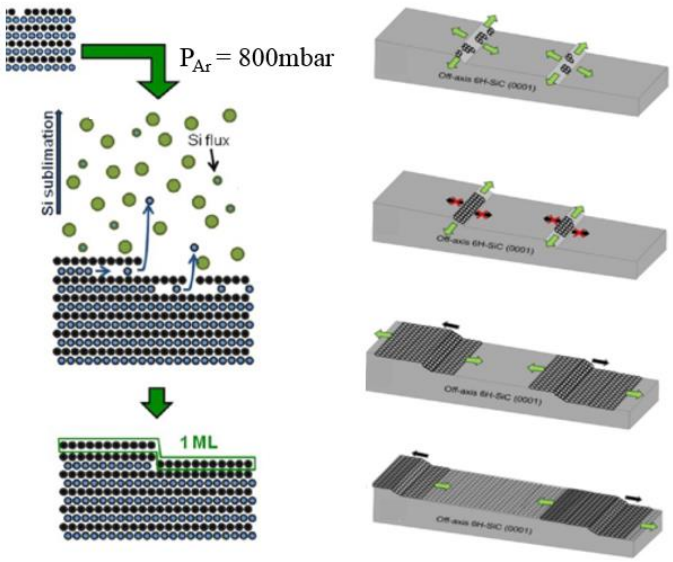

Figure 4.10 (Left) Epitaxial graphene growth under Ar fluxes, generating a uniform graphene monolayer. (Right) Schematic steps of the graphene growth from top to down.[158]

We used this substrate for the deposition of VOPc, having preliminarily characterised this surface by STM and XPS. The STM image of a large-area graphene with the honeycombed structure is shown in Figure 4.11 left. The observed regular structure is a Moiré pattern due to the presence of the buffer graphitic layer bond to the SiC. The zoomed image in Figure 4.11 right show atomic resolution in graphene; the structure of the substrate underneath is still visible.

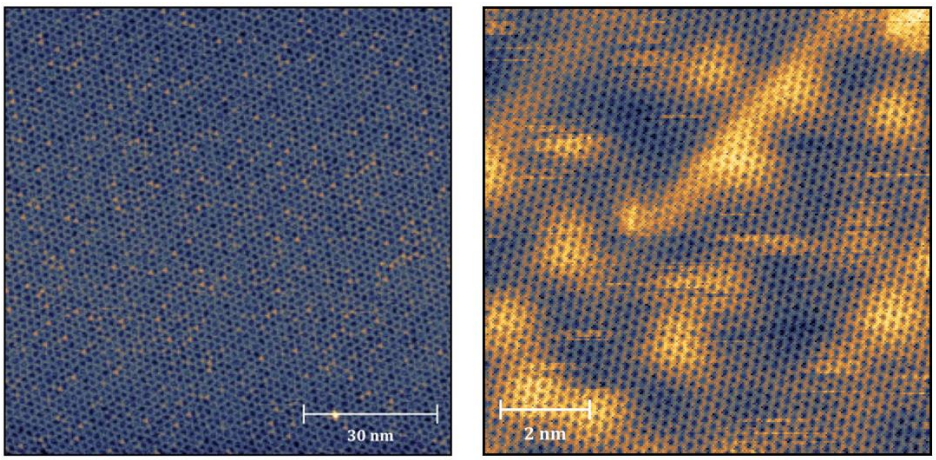

Figure 4.11 STM images of the graphene substrate performed at 1.7 K. The images has been acquired with the following conditions: (Left) Size: 100 × 100 nm², I = 10 pA, bias = 2 V; (Right) Size: 10 × 10 nm², I = 10 pA, bias = 2 V.

The XPS survey of the graphene (see Figure 4.12) shows the presence of the carbon and silicon, without any contamination.

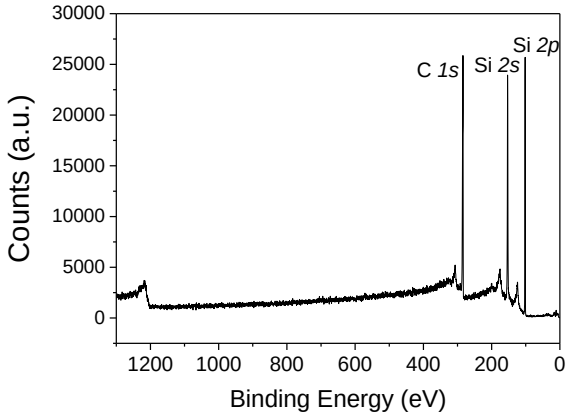

Figure 4.12 XPS survey of the bare graphene. The spectrum is acquired using a monochromatic Al source.

4.2.2 *In situ* characterisation of a submonolayer film of VOPc

Several articles reported on the sublimation of VOPc on different surfaces, [143,155–157] but few studies are focuses on graphene and HOPG.[155–157] Previously discussed study demonstrates the retention of the $S = 1/2$ of the vanadium after the deposition on graphene.[155] In order to confirm this information and to test the sublimation procedure, a VOPc submonolayer film on graphene has been prepared and characterised in the CeTeCS laboratory in Florence.

Sublimation has been carried out using a resistively heated quartz crucible in HV ($P \sim 5 \times 10^{-7}$ mbar) with a K-thermocouple buried into the molecular powder. The VOPc powders, purchased from Sigma-Aldrich, have been degasses for two days at a temperature lower than the sublimation temperature (~ 615 K) in order to eliminate possible volatile impurities. Prior to exposition to the molecular flux, the graphene substrate has been annealed at 770 K for 30 minutes. The VOPc molecules have been subsequently deposited on the freshly annealed substrate held at room temperature.

A submonolayer coverage of VOPc on graphene has been characterised by STM at 30 K. The Figure 4.13a shows a large VOPc island grown on the graphene substrate. A square packing is glimpsed inside the molecular island, but the tip is very unstable on the molecular layer border, probably because of the high mobility of the VOPc on this inert surface. The dendritic structure at the centre of the image (indicated by the red arrow), seems a disordered VOPc domain. A zoomed frame of this area is reported in Figure 4.13b. In this image, a higher resolution has been obtained inside the molecular layer and a square pattern is clearly observable. The mobile molecules on the border are less ordered, forming a dendritic domain.

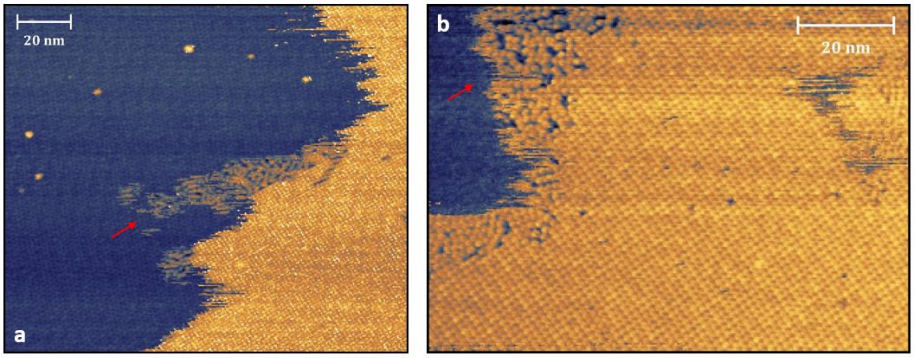

Figure 4.13 STM images of a submonolayer of VOPc on graphene; (a) size = 150 × 130 nm², I = 20 pA, bias= -2 V; (b) size = 100 × 72 nm², I = 5pA, bias = -2V.

Zooming further inside the island, we see a 2D-crystal structure (Figure 4.14). The ordered pattern observed in these areas feature regular brighter spots that could be attributed to the VO groups that protrude with respect to the plane of the molecule, suggesting the oxygen-up configuration. This hypothesis is supported by similar evidences found on VOPc grown on HOPG.[156]

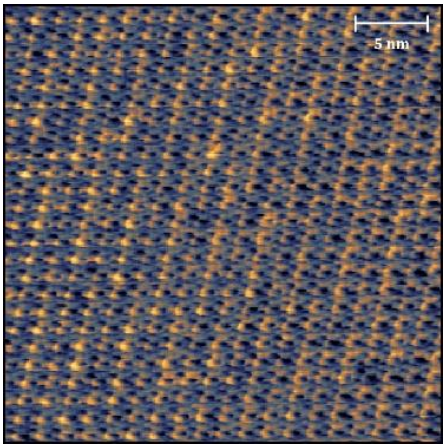

Figure 4.14 Zoom of the STM image reported in Figure 4.13; size = 30 × 30 nm², bias = -1.5 V, I = 5 pA.

In order to exclude the presence of charge transfer effects between the V^{4+} and the substrate, the submonolayer of VOPc has been characterised by XPS. The XPS spectra are reported in Figure 4.15 and Figure 4.16. The spectra have been calibrated setting the main carbon peak, attributed to the SiC contribution, at 283.4 eV.[161] The carbon region is shown for bare graphene and for graphene after the molecular deposition. The pristine graphene presents three contribution: SiC (at 283.4 eV), the graphene (at 284.7 eV) and the interface layer (at 285.5 eV). These energy values are

in good agreement with those obtained by synchrotron-radiation XPS for a graphene layer prepared in the same way.[161]

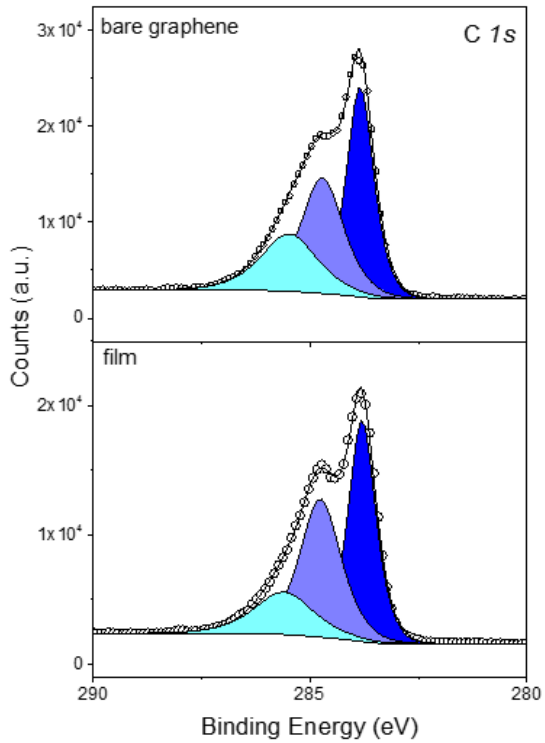

Figure 4.15 Carbon 1s peak for the bare graphene and for the VOPc film on graphene. Filled area and lines represent the best fit components and resulting spectra, respectively. A Shirley background has been subtracted. The spectra has been acquired using a monochromatic Al K_α source.

The C *1s* region is not relevant being the main carbon component for the phthalocyanine expected to be superposed to the peak of graphene.[143] The BE region between 510 and 535 eV is on the contrary very informative because it contains the main oxygen and vanadium peaks. The V $2p_{3/2}$ peak is observed at 516.4 eV, the O *1s* peak at 531.0 eV and their distance $\Delta E(O\ 1s_{V=O}\text{-}V\ 2p_{3/2})$ is 14.6 eV, a value perfectly in line with what observed in VOPc monolayer and multilayers.[143,155] This confirms that on the graphene substrate the metal atom is not subject to charge transfer processes. The retention of the unpaired electron in the d_{xy} is of crucial importance for our subsequent study. The nitrogen region presents a main peak at 398.9 eV, and a small shake up at higher binding energy, in line to what has been already observed for VOPc.[143,145]

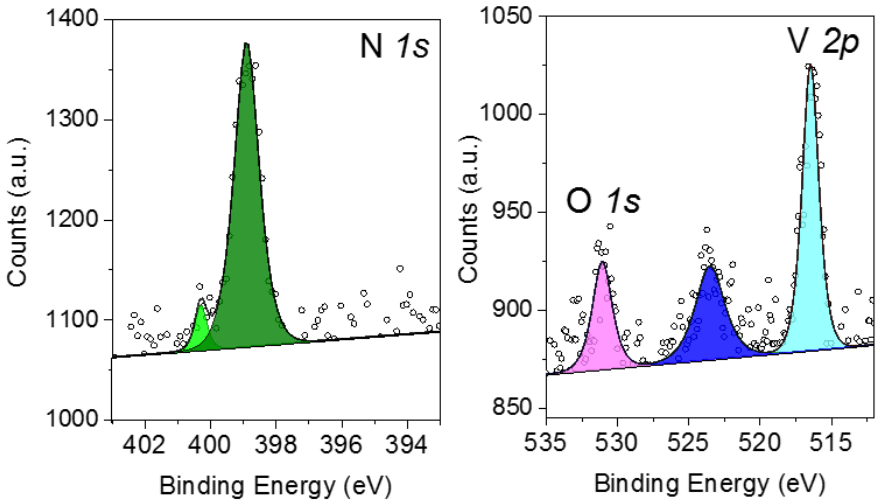

Figure 4.16 XPS spectra of a submonolayer coverage of VOPc on graphene; (left) N 1s, (right) O 1s and V 2p region. Filled area and lines represent the best-fit components and resulting spectra, respectively. A linear background has been subtracted. The spectra has been acquired using a monochromatic Al K_α source.

In the semi-quantitative analysis reported in Table 4.1, the carbon contribution is not taken into account because the molecular contribution cannot be extrapolated from the main peak of the substrate. The experimental data show a slight excess of vanadium and oxygen with respect to nitrogen. This could be attributed to impurity in the molecular powder even if a partial fragmentation of the molecule with the consequent release of phthalocyanine cannot be totally excluded. However, all STM characterisations performed in Florence or (later) in Hamburg have not revealed evidences of the presence of fragments or impurities in the deposits. Moreover, being the main goal of the planned experiments an investigation at the individual molecule level the eventual presence of irrelevant zones of the samples partially contaminated by spurious species have been judged not relevant.

Table 4.1 Semi-quantitative analysis of the VOPc film.

	O *1s*	**V *2p***	**N *1s***
% experimental	13.5	14.5	72.0
% theoretical	10.0	10.0	80.0

4.2.3 STM and IETS characterisation of VOPc on graphene

In order to have access to the single molecule magnetic degree of freedom the STM investigation can be extended to energy resolution by performing Inelastic

Electron Tunnelling Spectroscopy (IETS) at cryogenic temperatures eventually applying an external magnetic fields in order to remove the degeneracy between magnetic levels. Such an investigation has been performed in the Dynamics of Nanoelectronic Systems Group at the Max Planck Institute of Hamburg under the supervision of Dr. Sebastian Loth. In this institute is available a Unisoku STM/STS setup connected with a UHV platform for sample preparation. The STM has a ^{3}He pumped cryostat that allows to go down to 0.4 K. Both sample and tip are thermalized at low temperature, thus the thermal noise is minimised, fundamental requirement in order to acquire IETS spectra. It is possible to apply a magnetic field up to 9 T along the STM junction and of 2 T in an arbitrary direction. Thanks to the collaboration with Dr. S. Loth, profiting of a shot term visit grant of a COST initiative, I had the opportunity to spend two month work in their UHV-STM setup. With their state-of-the-art equipment, we investigated the VOPc submonolayer grown on a freshly purified graphene.

The same optimised protocol developed in Florence for the substrate cleaning and the molecular evaporation has been employed in Hamburg to prepare the VOPc submonolayer. In particular, the same home-made evaporator has been mounted on the preparation chamber in Hamburg. Subsequently a submonolayer of VOPc has been grown on a freshly purified graphene substrate. The large-scale image in Figure 4.17 shows an island of VOPc forming a 2D crystal. In the high-resolution zoom in Figure 4.17 left both the VOPc island and the graphene substrate, with atomic resolution, are clearly visible at bias of -2 V. In the STM in Hamburg the bias is applied to the sample, thus the configuration is opposite with respect to the Omicron STM in Florence. In Figure 4.17, by applying a negative voltage to the sample we probed the occupied states of the molecule. Reaching an higher spatial resolution with respect to previous experiment here it has been possible to make an assignment of the observed features: the sketch of a VOPc is tentatively superposed to the STM image as a guide.[156,157] The vanadyl group is visible as a sphere surrounded by eight lobes formed by the triazinic-like rings.

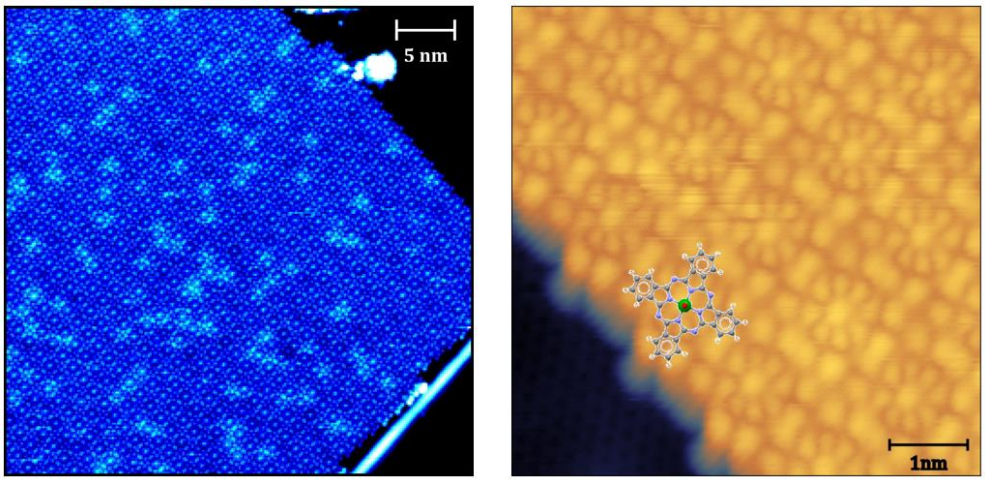

Figure 4.17 STM images, acquired at 1.8 K, of a submonolayer of VOPc on graphene. (Left) Size = 40 × 40 nm², I = 10 pA, bias = -2 V. (Right) Size = 40 × 40 nm², I = 10 pA, bias = -2 V.

Inversing the bias between the tip and the substrate the morphology of the molecular layer changes as illustrated in Figure 4.18, where the bright protrusions represent the vanadyl group. The different features of the molecular layer at the two opposite biases are analogous to what has been observed for VOPc monolayer on HOPG.[156] The resolution of Figure 4.18 is lower with respect to the previous one, but the STM junction appears more stable. In fact, often very high resolution is obtained when a small molecule is adsorbed at the top of the tip; however this molecule can be released during the spectroscopy, hampering a detailed characterisation as a function of applied voltage bias.

We succeeded in measuring the DOS of the VOPc molecules illustrated in Figure 4.18 right. The spectrum has been acquired on the ligands and on the vanadyl group, red and blue spot respectively on Figure 4.18. This investigation allows the determination of the orbital structure of the molecule. The Lowest Unoccupied Molecular Orbital (LUMO) appears at 0.77 V. The occupied state region presents a peak at -1.82 V in the spectrum taken on the ligand and at -2.01 V in the spectrum recorded on the vanadyl. Experimental and calculated DOS of VOPc deposited on HOPG shows a similar trend, with some shift in the peaks.[157] They found the LUMO at ≈ 1.6 V and two peaks at -1.61 V for the ligand and at -1.9 V for the vanadyl group. The different electronic structure and the different work functions of the substrate in the two studies could explain these differences.

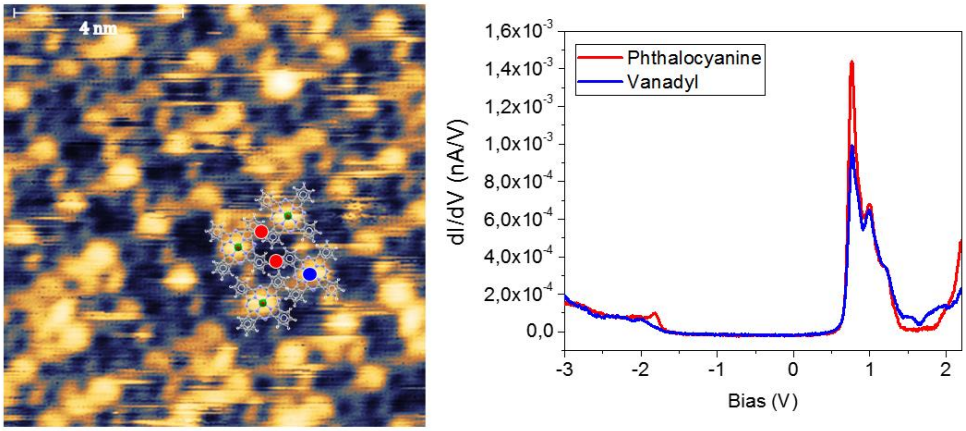

Figure 4.18 (Left) STM image of the VOPc layer on graphene. Dimension: 10 × 10 nm², I = 10 pA, bias = 2 V. (Right) STS curves measured on the ligands (red line) and on the vanadyl (blue line). The tunnel junction was set at the following conditions: V= 2.2 V, I = 100 Pa.

The step forward is to study the spin excitation of the VOPc by Inelastic Electron Tunnelling Spectroscopy (IETS). The IETS in fact probes electronic and magnetic properties of individual atoms, nanostructures and molecules. Heinrich *et al.* measured with this technique the spin-flip of individual manganese atom on Al_2O_3 islands.[162] Together with study on individual atoms,[148,163] also magnetic molecules have been probed by IETS.[164] Recently, Burgess *et al.* measured the spin excitation of individual Fe_4 molecules.

The principle of this characterisation technique are briefly presented here. The conduction process in a tunnel junction can occur following two paths: elastic and inelastic tunnelling. In the first, there is no exchange energy between the tip and the probed substrate, while in the second case the applied voltage is large enough to promote an excitation of the molecule. To describe the two tunnelling processes we can consider a spin in a tunnel junction, *i.e.* between the tip and the graphene substrate (see Figure 4.19). If the voltage applied to the tip is smaller with respect to the energy necessary to excite the local spin (ΔE), the tunnelling process is elastic. This tunnelling channel is always available if there are empty state on the sample at the same energy of the filled in the tip or *vice versa*. On the contrary, if the voltage of the junction match with the ΔE, the spin can be excited to a higher energy level. This is an additional conduction channel that can be detected as a step in the differential conductance of the tunnelling junction as a function of the applied voltage at the junction.

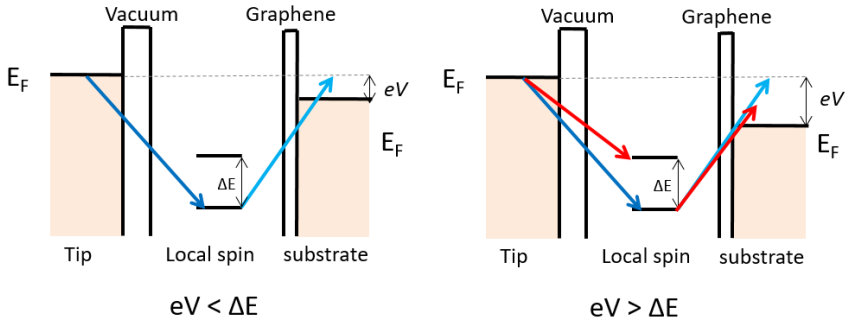

Figure 4.19. Elastic (left) and inelastic (right) tunnelling processes.

Considering our VOPc system, the unpaired electron is in the d_{xy} orbital and, if the system is inserted in a magnetic field, the orbital is spitted because of the Zeeman Effect. The system can therefore be described by a simple Hamiltonian containing the Zeeman splitting:

$$\widehat{H}_Z = g\mu_B \widehat{\boldsymbol{H}} \cdot \widehat{\boldsymbol{S}}_T \qquad (6)$$

where g is the Landé g-factor, μ_B the Bohr magnetron and S_T the total spin and H the applied magnetic field. The calculated spectra for an S = 1/2 in different magnetic fields are reported in Figure 4.20. Dr. L. Malavolti of the Max Planck Institute of Hamburg performed the calculations considering the tunnelling as a scattering process in the frame of the Born approximation.[165] On the basis of the selection rules, the spin transition in the IETS process must preserve the spin angular momentum. The transition intensities are calculated using a Hamiltonian of interaction:

$$H = \boldsymbol{\sigma} \cdot \boldsymbol{S} + U \qquad (7)$$

where σ is the spin of the electron, S is the spin of the individual molecule and U is a spin independent scattering term.

The threshold voltages at which the step is observed corresponds to the energy of the spin excitation. The expected Zeeman splitting for the system in 9 T magnetic field is 1.05 mV. In the experimental differential conductance spectra (dI/dV) reported in Figure 2.1 bottom, a step is observed around zero. This feature is more visible at higher field, as expected from the comparison with experimental data. However, the oscillation of the signal at higher biases makes difficult to determine threshold voltage of the signal. The shape of the signal around zero has a “V-shape”, making the experimental spectrum different with respect to the calculated.

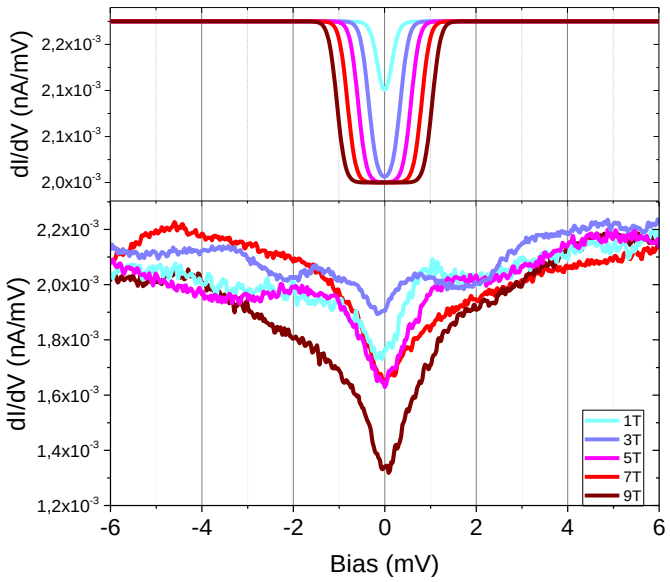

Figure 4.20 (Top) Simulated (g-factor = 2) and (bottom) experimental IETS spectra on VOPc on graphene. The experimental curves were recorded at 0.6 T and the junction was set at the following conditions: V = 10 mV, I = 20 pA, lock-in modulation 0.5 mV.

The experimental spectra reported in Figure 4.20 has been recorded with the tip probing the ligand of the VOPc, but a comparable situation is observed for the spectra recorded on the vanadyl group. For these curves is difficult to certainly affirm that the signal is due to the spin transition of the $S = 1/2$ of the VOPc, as a clear shift of the expected step with the applied magnetic field is not visible. It must be stressed that $S = 1/2$ systems are more challenging to be proved as the only excitation is induced by the Zeeman term and occurs at significantly lower energy than those observed in atoms and molecules with the spin multiple split in zero field by the magnetic anisotropy. An additional experimental difficulty we have encountered is that on the graphene substrate it is not possible to treat the tip in order recover the optimal conducting conditions. It must be noted that the IETS spectra of the bare graphene in an applied field is on its own not flat, making the investigation of the molecule even more complicated. Additionally, low energy phonons of the graphene could also explain the structuration of the spectrum on the graphene and induce some alterations on that of VOPc/graphene. In addition, the application of a magnetic field in a conductor generates the circulation of the charge carriers in cyclotron orbits called Landau Levels (LLs). Using STS Miller *et al.* observed the LLs on graphene on silicon carbide showing non-equally-spaced energy level with a peak at zero-energy.[166] This peak could be present also in our spectrum of the graphene substrate, altering our measurements.

Though promising and informative, these low temperature single molecule spectroscopy studies are not yet complete. The study of the VOPc on a metallic substrate could help to better understand the IETS behaviour of the molecule, disentangling the signal of the molecule from that of a complex substrate such as the graphene on SiC.

5 Experimental methods

In order to study the deposition on surface of magnetic molecules a multi technique approach is essential. This allows probing the morphologic, chemical and magnetic characteristics of a molecular film, as sketched in Figure 5.1. In fact, only taking advantage of the information obtained by several technique it is possible to have a complete picture of the mechanisms involved in the deposition of the molecules on surface. In this chapter are illustrate the technique I have used during my PhD thesis.

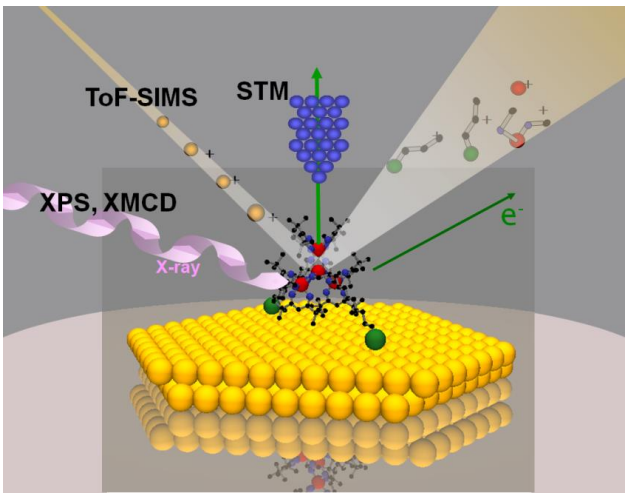

Figure 5.1 Pictorial description of the multi-technique approach required for the characterisation of magnetic molecules on surface.

5.1 Standard magnetometry

The magnetic characterisation of bulk powder samples and thick films in this PhD thesis have been performed by standard magnetometry technique in order to collect initial information about the molecular materials we planned to transfer to surfaces as well as to characterise thick deposits obtained by sublimation on diamagnetic surfaces.

Standard magnetometers allow measuring the susceptibility χ and the magnetisation M of the samples. The susceptibility is defined as:

$$\chi = \frac{\delta M}{\delta H} \tag{8}$$

where *M* is the molar magnetisation of the sample and *H* is the magnetic field vector. In the case of the molecular scale, the magnetic moment can be defined as the energy variation of the system due to the interaction with the applied magnetic field:

$$m = -\frac{\delta E}{\delta H} \tag{9}$$

The macroscopic magnetic properties are linked to the *n* energetic levels ($E_n$where *n* = 1, 2, …, *n*) of the system by the Boltzmann distribution law:

$$M = \frac{N \sum_n (-\frac{\delta E_n}{\delta H}) e^{-\frac{E_n}{kT}}}{\sum_n e^{-\frac{E_n}{kT}}} \tag{10}$$

where T is the temperature expressed in Kelvin and the *k* is the Boltzmann constant.

The standard magnetometers are based on induction. A voltage is induced in the detection coil if the magnetic flux changes in time. A magnetised sample can thus induce a an electromotive force if its position is changed, as it happens in direct current (*dc*) magnetometer, or if its magnetisation varies in time due to an oscillating magnetic field. The latter is the case of alternate current (*ac*) susceptometry. To separate the contribution coming from the sample from spurious ones a special design of the detection coil is employed, which becomes sensitive only to the gradient of the magnetic field and is therefore called gradiometer. Different types of gradiometer exist but the second order is the most commonly used. The coils of the magnetometers allow to eliminate the contribution of the external magnetic field.

The sensitivity of the measurement can be enhanced by using a Superconductive Quantum Interference Device (SQUID), the more sensitive instrument to detect the magnetic flux. The device is based on a superconductive ring with a Josephson junction.

5.1.1 *Ac* susceptibility

The *ac* susceptibility allows to characterise the magnetic dynamics of the investigated magnetic materials. The sample is inserted in a primary coil, as illustrated in Figure 5.2. A small oscillating field of a few Oe is applied to the sample by generating an alternate potential to the end of the coil. A secondary coil is present, a first order gradiometer. The two parts of the secondary coil have opposite wounding so no voltage is induced by the first coil on the second one and *vice versa,* unless the geometry is unbalanced by the presence of the sample in one of the two secondary coils. The oscillating magnetic field provokes an oscillation of the magnetic moment of the sample that is sensed by the secondary coil. The signal is proportional to the change of the sample magnetisation.

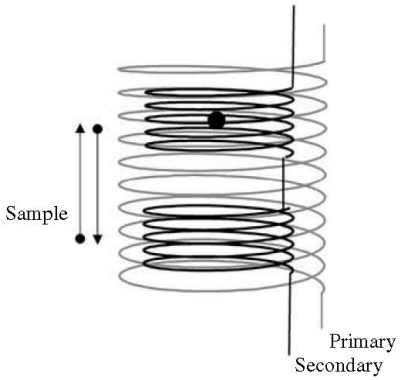

Figure 5.2 The sample inserted in a primary coil that generate an oscillating magnetic field and a second coil that sense the magnetic response of the sample.[10]

The magnetic field experienced by the sample is:

$$H = H_0 + h\,cos\omega t \tag{11}$$

where H_0 is the external magnetic field applied in the same direction of the *ac* field, h is the amplitude of the oscillation and ω is the frequency of the *ac* magnetic field. *Ac* susceptometry allows measuring the magnetic susceptibility, as described by equation 6, and illustrated in Figure 5.3, because the oscillation in field is very small. Moreover, the sensitivity of the technique does not depend on the applied static magnetic field. On the contrary, in *dc* susceptibility measurements the susceptibility can be obtained only in the low field approximation as:

$$\chi = \frac{M}{H} \tag{12}$$

where M is assumed to be linear with H. From a dynamic point of view, if the sample magnetisation does not follow the oscillating magnetic field the susceptibility can be described as:

$$\chi(\omega) = \chi'(\omega) - i\chi''(\omega) \tag{13}$$

where χ' and χ'' are the real and imaginary parts of the susceptibility (see Figure 5.4).

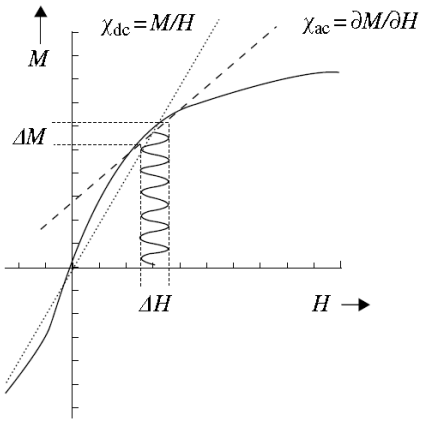

Figure 5.3 Ac and dc susceptibility.[10]

Two possible extreme conditions can be encountered. When the *ac* field ω oscillates with such a frequency that the magnetic response is not rapid enough to follow the field oscillations, the system is in adiabatic conditions, described by χ_S. On the contrary, if ω is slow with respect to the relaxation time, the system is in isotherm conditions described by χ_T. Casimir and Du Pré suggested[167] introducing these two values in equation 11 giving rise to:

$$\chi' = \frac{\chi_T - \chi_S}{1 + \omega^2\tau^2} + \chi_S \tag{14}$$

$$\chi'' = \frac{(\chi_T - \chi_S)\omega t}{1 + \omega^2\tau^2} \tag{15}$$

where τ is the relaxation time of the magnetisation of the system. The main relaxation path is via phonon coupling, therefore $\chi_S(\omega)$ can be interpreted as susceptibility of the isolated molecule, and $\chi_T(\omega)$ correspond to the system in equilibrium with phonons.

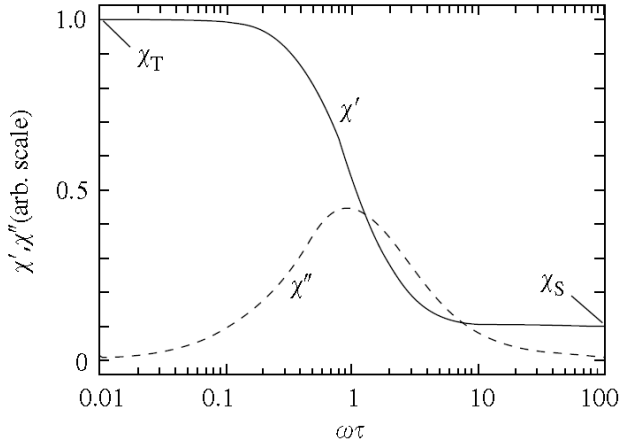

Figure 5.4 $\chi'$and χ''reported as a function of the ac frequency.[10]

If the system presents a distribution of the relaxation times, the susceptibility can be described as:[168]

$$\chi'(\omega) = \chi_S + (\chi_T - \chi_S)\frac{1 + (\omega\tau)^{1-\alpha}\sin(\pi\alpha/2)}{1 + 2(\omega\tau)^{1-\alpha}\sin(\pi\alpha/2) + (\omega\tau)^{2-2\alpha}} \qquad (16)$$

$$\chi''(\omega) = (\chi_T - \chi_S)\frac{(\omega\tau)^{1-\alpha}\cos(\pi\alpha/2)}{1 + 2(\omega\tau)^{1-\alpha}\sin(\pi\alpha/2) + (\omega\tau)^{2-2\alpha}} \qquad (17)$$

where the wider is the distribution of relaxation times, the larger is α. The fit of the experimental data of χ'' *vs.* ωt allows to obtain the relaxation time and its distribution at the measurement temperature. If the measure is repeated for different temperatures, a plot of the relaxation times *vs.* temperature can be obtained. The exponential decay can be fitted in first approximation with an Arrhenius behaviour:

$$\tau = \tau_0 e^{\Delta E/k_b T} \qquad (18)$$

This treatment is often used to obtain the energy barrier characteristic of SMM behaviour.[10]

5.2 Photoelectron Spectroscopy

Photoelectron Spectroscopy (PS) technique is based on photoelectric effect, observed for the first time by H. Hertz in 1887 and then explained by A. Einstein.[169] The photoelectric effect occurs when photons provide enough energy to an electron to overcome its ionisation potential and an electron is emitted from the atom as a photoelectron.

The mean free path of electrons in matter is of the order of the nanometre, for this reason, even if the ionisation occurs deeper in the sample, only the electrons originated in the first nanometres leave the surface. The technique is therefore surface sensitive.

The diagram reported in Figure 5.5 can be used to describe the photoelectron process. The Binding Energy (E_B) of a photoelectron can be defined as:

$$E_B = h\nu + E_K + \phi_{Sa} - \phi_{Sp} \tag{19}$$

where E_K is the kinetic energy of the photoelectron, $h\nu$ the energy of the incidence radiation, ϕ_{Sa} and ϕ_{Sp} the work function respectively of the sample and of the spectrometer. The work function, ϕ, is defined as the minimum energy needed to remove an electron from a solid surface, and is different for each material, thus also for the sample and the spectrometer. The sample and the spectrometer are electrically connected and grounded, so their Fermi energies (E_F) are at the same level. However, the emitted photoelectrons, being transmitted from the sample to the spectrometer, are shifted in energy because of the different work function of the two materials. For this reason, the spectra need to be corrected by an internal reference to be comparable to the data acquired with different instruments. The PE probes the final state of the system, while the ground state can be obtained by theoretical considerations.

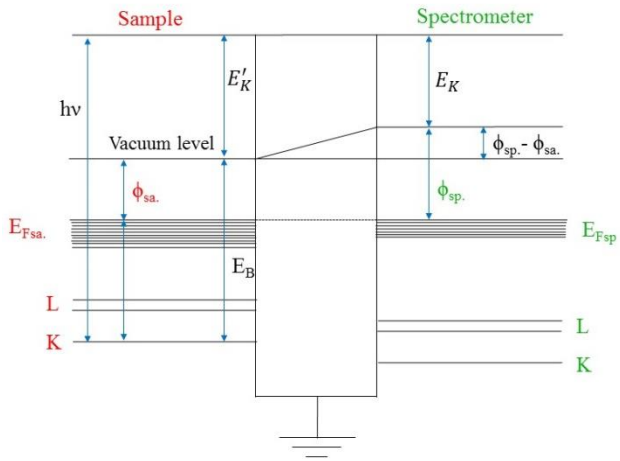

Figure 5.5 Level scheme of the sample (right) and spectrometer (left).

The emitted photoelectrons can be discriminated for their different kinetic energy by using a hemispherical analyser and can be counted by a detector placed at the end of the analyser, as illustrated in Figure 5.6. The spectra shown in this thesis are acquired in Fixed Analyser Transmission (FAT) mode. In FAT mode, the pass energy (P.E.) of the analyser is held at a constant value and the transfer lens system present in the linear part of the analyser has been used to retard the kinetic energy of

electrons to the range accepted by the analyser. This method allows to have the same energy resolution for the entire spectrum. The spectra are commonly shown as a function of the binding energy because of the dependence of the kinetic energy by the radiation energy.

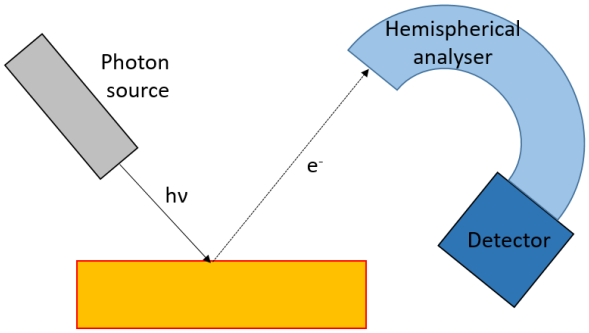

Figure 5.6 The photon flux excites an electron of the substrate that is emitted as a photoelectron. The photoelectron than enters in the hemispherical analyser to be separated in energy and then detected.

5.2.1 X-ray Photoelectron Spectroscopy

X-ray photoelectron spectroscopy (XPS) is a technique used for studying the elemental composition and the chemical environment of the different species at the surface of a solid sample. The X-ray exciting radiations more commonly used are Al K_α (E = 1486.6 eV) and Mg K_α (E = 1253.6 eV). In this energy range of photons, the photoelectric effect promotes the emission of electrons from the core levels of atoms. The binding energy of the detected photoelectrons depends on the electron density on the element, giving information on the oxidation state of the atom and on the elements or groups to which this atom is bound. Electrons in orbitals with angular momentum $l \neq 0$ feature multiplet splitting of the peak, up to several eV, due to the spin-orbit coupling. This feature can help in the identification of the specific photoelectron.

To properly interpret an XPS spectrum others phenomena have to be taken into account, the most relevant one being the Auger effect. When X-rays interact with the surface, Auger emissions can occur because of the *two-electron process* shown in Figure 5.7. This Auger process happens *ca.* 10^{-14} seconds after the photoelectric event. The Auger emission is two electron process: an external electron falls into the inner orbital and a second electron is emitted, carrying the exceeding energy (Figure 5.7). The energy of the Auger electron is not influenced by the X-ray excitation energy, but depends only on the energy levels of the sample.

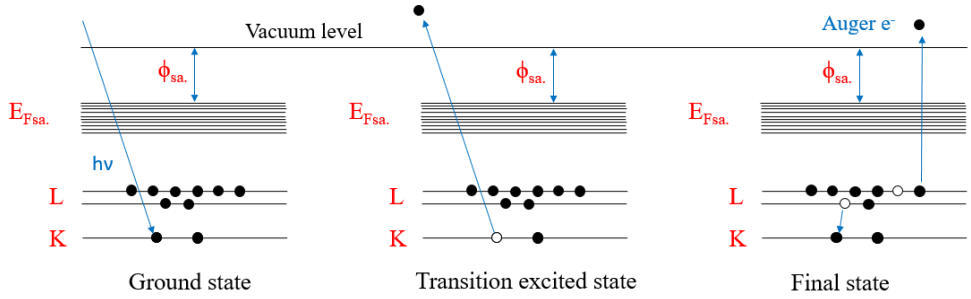

Figure 5.7 Schematic representation of the Auger process.

Another extra event in the photoelectron process is related to the excited states. When the photoemission process involves also a transition of a core electron into a valence band, the final excited atom is not in the ground state. Therefore, the kinetic energy of the resulting photon, E_K, is lower than the expected one, of a value ΔE depending on the energy of the excited state. This generates a shake-up peak that falls at a binding energy higher of ΔE with respect to the main peak.

The analysis of the peaks position in the spectra and a proper attribution of each signal allows a *qualitative analysis*, thus leading to the identification of the elements present in the sample. In addition to this qualitative information, the XPS spectrum can also give a quantification of the elements present at the surface. This is possible by a comparison of the area of the peak of the elements of interest. In order to compare and quantify an element content, however, the efficiency of promoting the emission and detection of each photoelectron has to be considered.

In fact, the intensity of a photoelectron peak depends on several factors:

$$I_{A,c} = f \cdot N_A \cdot \sigma_{A,c} \cdot \lambda \cdot \theta \cdot F \cdot T \cdot D \cdot a \qquad (20)$$

Where:

$I_{A,c}$: intensity of photoelectrons emitted by a core level c of the A element,

f: flux of X-photons for unity of time and volume,

N_A: number of atoms of the element A per unity of volume,

$\sigma_{A,c}$: photoelectric cross section of the core level c of the A element,

λ: mean free path of the photoelectrons in the sample,

θ: angle between the direction of the photoelectron and the normal to the surface,

F: solid angle of the analyser,

T: transmission function of the analyser,

D: efficiency of the detector,

a: area of the sample from which the detected photoelectrons arrive.

Often, however, an approximation can be used considering either empirically measured atom sensitivity factors or by assuming that the most relevant parameter is the cross-section (σ) of the considered transition. In this thesis we used the cross

section calculated in the dipole length approximation and reported in the literature.[170,171]

In this approximation, the atomic percentage of each element is calculated as:

$$\%\ Element(A) = \frac{I_A/\sigma_A}{\sum I_i/\sigma_i}\ x\ 100 \qquad (21)$$

where I_A and I_i are the intensity of photoelectrons emitted by an A element or b the sum i of all elements.

5.2.2 Ultraviolet photoelectron spectroscopy

In Ultraviolet Photoelectron Spectroscopy (UPS) the energy used to probe the sample is lower with respect to XPS, thus permitting to probe only the valence band of the sample but with a higher resolution. The most common excitation source is the helium discharge lamp that emits at two lines of radiation: He^{I} (light emitted from neutral atoms) at 21.22 eV and He^{II} 40.82 eV (light emitted by singly ionised atoms). The UPS characterisation allows studying the electronic structure of the surface. It is very useful to determine the experimental DOS of a molecular film, which can be compared with the calculated DOS. We exploit this comparison in the study of the sublimation process of Fe_4 and $Fe(dpm)_3$ molecules as discussed in Section 2.4.1. An example of UPS spectra compared to calculated DOS is show in Figure 5.8.

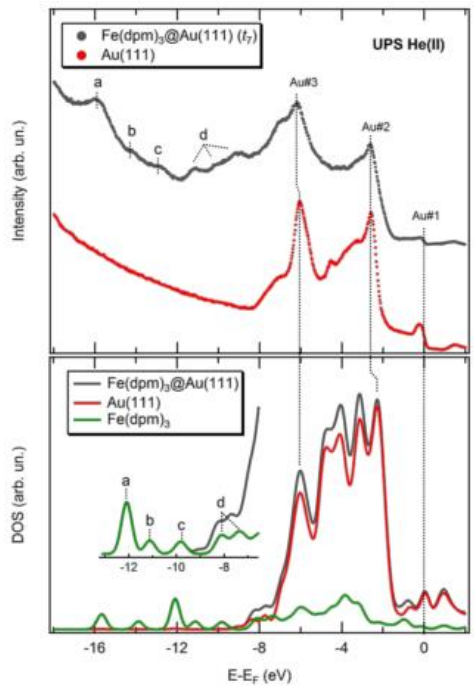

Figure 5.8 (Up) experimental UPS spectra of $Fe(dpm)_3$ grown on Au(111) and of the bare substrate. (Down) calculated DOS for $Fe(dpm)_3$, Au(111) and $Fe(dpm)_2$@Au(111).

5.3 Scanning Tunnelling Microscopy

Scanning Tunnelling Microscopy (STM), together with Atomic Force Microscopy, is a scanning probe technique, a very powerful technique to study surfaces. The probe is a sharp tip that allows to image the surface with very high resolution. The STM was invented by G. Binnig and H. Rohrer at the IBM in Zurich in 1981. They received the Nobel Prize in physics five years after the invention.

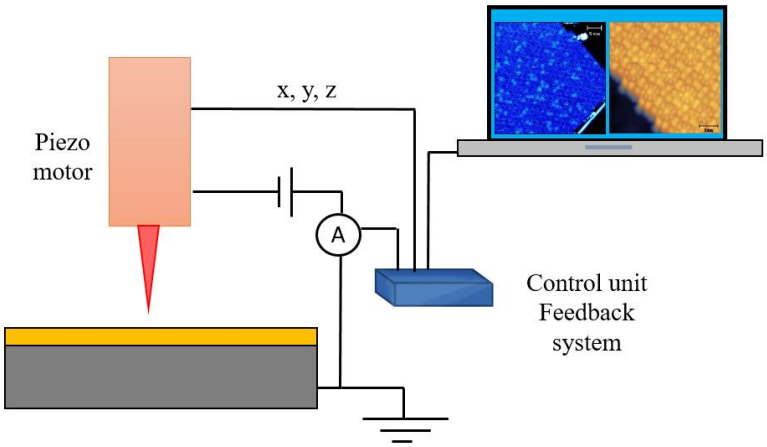

Figure 5.9 Scheme of an STM.

A schematic representation of an STM is shown in Figure 5.9. In STM a sharp conducting tip is placed over a conducting surface and a bias voltage is applied between the two electrodes. When the tip is sufficiently close to the surface (≈ 10 Å) a tunnelling current passes through the junction. The STM image is acquired scanning the tip, with a fine control of the x, y, z positions, over the sample. The fine control of the movement is achieved by a piezoelectric motor system. The feedback loop allows to scan the surface with a constant tunnelling current, *i.e.* in constant current mode. The feedback circuit receives the tunnel current and, if the current changes, modifies the tip-sample distance in order to restore the initial current. The STM images acquired in the frame of this PhD thesis are obtained using constant current mode, however the images can be also acquired in constant height mode. In this case, the height is kept constant by modification of the tunnel current.

In a simplified picture, the tunnelling of electrons can be described following the scheme depicted in Figure 5.10 representing a particle passing through a barrier with height V_0 and thickness z.

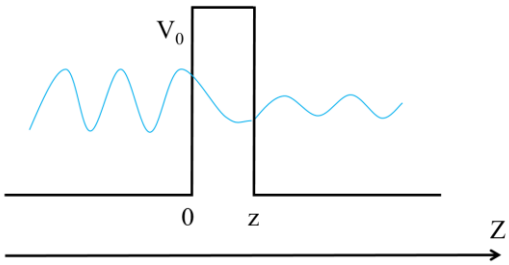

Figure 5.10 Schematic representation of a tunnelling barrier. The path of the electron, coming from the right, is indicated in blue.

The particle with an energy $E < V_0$ can go beyond the barrier only in a quantum mechanical system. In that case the electron can be described by a wave function $\psi(z)$. The wave function can be obtained resolving the time independent Schrödinger equation:

$$H\psi(z) = E\psi(z) \tag{22}$$

where the Hamiltonian is:

$$H = -\frac{\hbar}{2m}\frac{d^2}{dz^2} + V \tag{23}$$

with $V = 0$ outside the barrier and $V = V_0$ inside the barrier.

The solution of the equation 20 for an electron going in the positive Z direction is:

$$\psi(z) = \psi(0)e^{-kz} \tag{24}$$

where the k exponential factor is given by:

$$k = \sqrt{\frac{2m(V_0 - E)}{\hbar}} \tag{25}$$

and $E < V_0$. The probability to find an electron inside the barrier is:

$$|\psi^2(0)|e^{-2kz} \tag{26}$$

Therefore the tunnel current I_t can be described as:

$$I_t \propto e^{-2kz} \tag{27}$$

We can clearly see that the tunnel current decays exponentially with the distance between the tip and the sample. For this reason, the measured tunnel current is mainly due to the interaction of the very last atom of the tip with the substrate.

A more accurate treatment of the process can be done considering the tunnelling process related to the many independent scattering events that brings the electron to overcome the barrier.[172] Developing this formalism,[173,174] we can obtain that the tunnelling current is proportional to several physical quantities:

$$I_t \propto \rho_t(E_F) \cdot \rho_s(E_F) \cdot V \cdot e^{-2kz} \tag{28}$$

where $\rho_t(E_F)$ and $\rho_s(E_F)$ are the local density of state (LDOS) of the tip and the sample at the Fermi energy and V is the voltage applied to the junction. The DOS can be defined "local" because is spatially resolved. Thus, in STM the contrast is due to both the topography and the density of states of the substrate. In an STM image, we

can consider that the density of states of the tip is the same in the entire scan, so this contribution, in a first approximation, is not taken into account. This double dependence makes the analysis of the image less intuitive but makes the STM image very informative.

5.3.1 Scanning Tunnelling Spectroscopy

As we have seen in the previous section, the tunnelling current depends on the LDOS of the surface and the tip. The STS allows studying the LDOS of the surface in more detail. The tip is therefore positioned on the top of the zone of interest and the feedback loop is switched off. A voltage ramp is applied to the tunnel junction and the current is measured. If we neglect the contribution of the tip, the tunnel junction would depends only on the density of states of the investigated substrate and the applied bias.

Therefore, a *dI/dV* curve, namely proportional to the conductance in the STM junction, would give substantial information on the LDOS of the substrate. Experimentally a lock-in detection of an alternate bias is employed to properly measure the *dI*/*dV* curve. An *ac* bias is superimposed to the potential ramp and the lock-in allows to discard the capacitive current signal. In order to take into account the differences in the transmission coefficient of the junction, a further normalisation is used.

5.4 Time of Flight Secondary Ion Mass Spectrometry

The Time-of-Flight Secondary Ion Mass Spectrometry (ToF-SIMS, see a scheme in Figure 5.11) is a surface sensitive technique that provides information on the chemical nature of the analysed surface. In this technique, a pulsed ion beam is used to remove molecules from the outermost surface of the sample. Molecular ions, or their fragments, come from the topmost layers of the sample and only these fragments have sufficient energy to overcome the surface binding energy and leave the sample.

In the ToF-SIMS a collimated primary beam of ions (Ga^+, Bi^+, $C60^+$, Au^+ *etc.*) is accelerated to the investigated zone of the sample with energy in the range of 10-25 keV. The strong interaction of the beam provokes the fragmentation of the first layers of the surface. These fragments are constituted by neutral, positive or negative particles; charged particles can be thus extracted and accelerated toward a detector using a fixed voltage. If a positive voltage is applied, only the negative ions would be detected and *vice versa*.

In a ToF detector, these ions are differentiated on the basis of the following relation:

$$E = \frac{mv^2}{2} = \frac{mL^2}{2zt^2} \tag{29}$$

where E is the acceleration energy, m the mass of the flying object, v the velocity of the object, L is the length of the travel and t is the flight time. By placing the detector far from the sample, which means that secondary ions have a long path (see Figure 5.11), it is possible to get an excellent mass resolution (often exceeding 10.000 $m/\Delta m$).

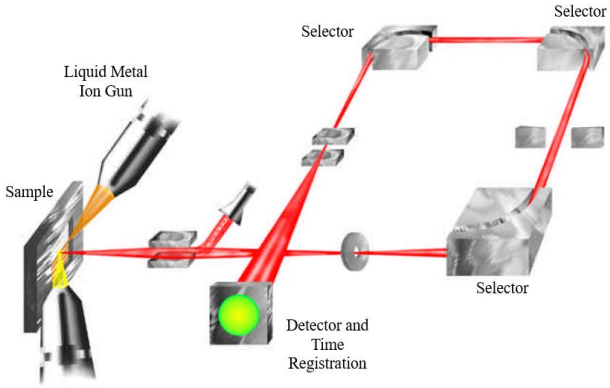

Figure 5.11 ToF-SIMS scheme. Source: TRIFT III manual.

After separation in the ToF analyser, the secondary ions are post-accelerated with a voltage up to 15 kV. This acceleration is applied to the ions to improve the detection efficiency of the high-mass ions. In the last step, the ions reach the detector unit, which is typically composed by a photo-converter electrode, a channel plate, a scintillator, a photomultiplier and a counter, all in series.

ToF-SIMS analyses reported in this PhD thesis have been performed with a TRIFT III time-of flight secondary ion mass spectrometer (Physical Electronics, Chanhassen, MN, USA), equipped with a gold liquid-metal primary ion source, available at the University of Siena thanks to a collaboration with Prof. A. Magnani. Positive-ion spectra have been acquired with a pulsed Au^+ primary ion beam, by rastering the ion beam over a 100 μm × 100 μm sample area.

5.5 Use of synchrotron for the characterisation of magnetic molecules

The synchrotron radiation is obtained when an accelerated electron beam is deviated by its trajectory; the energy loss is the electromagnetic synchrotron radiation. The synchrotron radiation has some characteristics that can be described as follows:

- *high brilliance*: the synchrotron source is more than hundreds of thousands times brighter than a conventional X-ray source and highly collimated;
- *polarisation*: the synchrotron radiation is highly polarised, can be polarised both linearly and circularly;

- *wide energy spectrum*: synchrotron radiation is emitted with a wide range of energies, allowing a beam of any energy to be produced, from microwaves to hard X-rays.

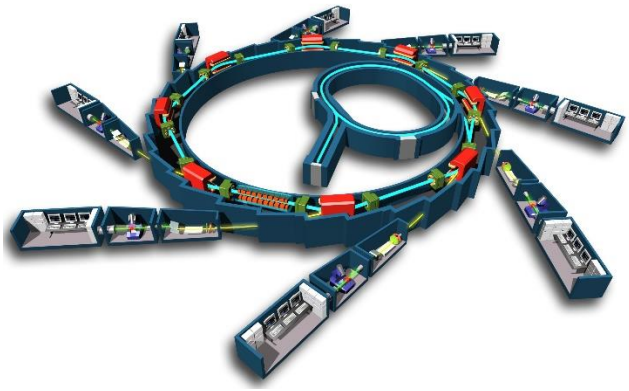

Figure 5.12 Scheme of a synchrotron presenting the linear accelerator, the booster, the storage ring and the beamlines. Source: Soleil Synchrotron.

In order to obtain the synchrotron radiation, a first electron radiation of several MeV is created by an electron gun. The electrons pass through a linear accelerator that imparts them an energy of hundreds of MeV. The electrons move then into the booster ring and are accelerated until GeV. They are then injected into the storage ring where their linear trajectory are deviated by the magnetic field (focussing magnets). The bending magnets around the storage ring bent the electrons into their racetrack orbit. As the electron are deflected, they produce the "white" light tangential to the plane of the electron beam. This is the synchrotron radiation that can be used from each beamline (see Figure 5.12) placed in each curved section of the storing ring where are installed bending magnets and eventually insertion devices to induce more complex motions in electrons. Those devices are constituted by periodic arrays of magnets placed above and below the electron pathway (Figure 5.13). The insertion devices are divided in two classes: wigglers and undulators. The wiggler produces a high-energy radiation (10-20 KeV) that is not highly collimated. The undulator, on the contrary, produces a lower-intensity (in average) radiation even if intense emission is obtained for specific energy ranges depending on the design of the apparatus. This second type of insertion devices, made up of a complex array of small magnets, force the electrons to follow an undulating trajectory (see Figure 5.13). The light produced by undulators is more collimated and by specific displacements on the components of the undulators is possible to produce selectively linearly (vertical and horizontal) and circularly (left and right) polarised light. The most advanced beamlines in which X-ray absorption spectroscopy (XAS) experiments are carried out are equipped with undulators.

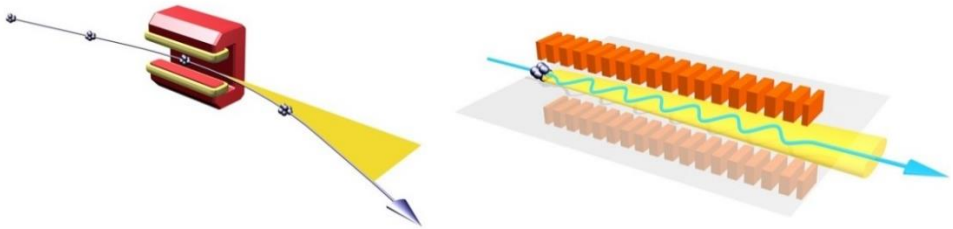

Figure 5.13 Schematic representation of a bending magnet (right) and insertion device (left). Source: Soleil Synchrotron.

5.6 Ultra-low temperature X-ray absorption end station

Most of the XAS characterisations described in this thesis (Chapter 2) have been performed using the Très Bas Température (TBT) end-station installed until November 2016 at the SIM-X11MA beamline at the Swiss Light Source (PSI, Switzerland) in Figure 5.14. The studies reported here have been possible only using this end-station, allowing reaching temperature as low as 300 mK in UHV. The TBT has been designed and developed by Dr. J-P Kappler of Institut de Physique et de Chimie des Matériaux de Strasbourg (IPCMS) and Dr. Ph. Sainctavit of Institut de Minéralogie et de Physique des Milieux Condensées (IMPMC), Université Pierre et Marie Curie, Paris in collaboration with the low-temperature staff of Air Liquide (Grenoble, France).

The end-station is constituted of two main parts: a 6 Tesla cryomagnet inside a cryostat with optical access and a chamber normally used to introduce the samples and that can be adapted to some *in situ* preparations. The cryostat is equipped with a ^{3}He-^{4}He dilution insert that allows measure samples in UHV environment at temperatures as low as 300 mK under X-ray irradiation. A complete description of the set-up can be found in literature.[175,176]

The samples are installed on an oxygen-free high thermal conductivity (OFHC) copper sample holder directly screwed on the cold finger of the dilution cryostat that is electrically isolated with a sapphire block from the insert. The temperature on the set-up is measured by silicon diodes from 300 K to 4 K and with a ruthenium oxide (RuO_2) sensor below 4 K. RuO_2 resistances are also used on the sample holder to monitor the temperature during the experiment. RuO_2 resistances can be probed with currents as low as only a few nanoamperes, corresponding to very low power dissipation ($< 10^{-10}$ W), that does not influence the temperature of the sample. The sensitivity RuO_2 resistances increases when the temperature decreases, resulting in very high sensitivity below 1 K.

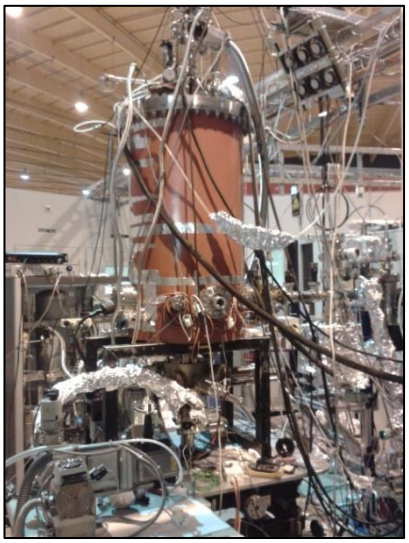

Figure 5.14 TBT end-station at the SIM-X11MA beamline at the Swiss Light Source (PSI, Switzerland).

5.7 XAS characterisation

XAS experiments allow to study several properties of thin films of magnetic molecules. The main advantages are related to:

- *element sensitivity:* the transition depends to the electronic structure of the surface, so it is a fingerprint of the atom;
- *valence sensitivity:* the shift of the peak is influenced by the electrostatic surrounding of the investigated element;
- *surface sensitivity:* using an adapted detector the technique can be sensitive to the first few nanometres of the surface;
- *sensitivity to the spin*: the use of an X-ray circular polarised light allows to be sensitive to the spin imbalance;
- *sensitivity to the anisotropy of the charge distribution of the absorbing atoms:* using the linear polarised light the technique probes the anisotropy of the orbitals of the surface, giving information on the ordering of the probed layer.

The XAS process can be simply described by a one-electron model (see Figure 5.15). An electron of the inner core is excited by the X-ray radiation to an unoccupied electronic state. In the case of the first transition series metal atoms the $L_{2,3}$ edges (transition from 2*p* to 3*d* orbitals) are the most commonly studied, while the rare earths are probed using $M_{4,5}$ edges (transition from 3*d* to 4*f* orbitals).

The XAS technique is surface sensitive when the Total Electron Yield (TEY) detection[177] is used. After the XAS process the probed atom presents a core hole that is not stable and can thus relax by fluorescence or causing an emission of secondary

electrons. The rate of these processes is proportional to the probability of XAS absorption and can therefore be used to quantify the absorption. The emission of secondary electrons charge the sample and if the sample is conductive its neutrality can be re-established by grounding the sample holder. A picoammeter inserted between the sample and the ground allows then an indirect measurement of the absorption. Being the mean-free path of electrons of the order of a few nanometers, the TEY detection is surface-sensitive. TEY detection needs a normalization against a non-absorbing material to monitor the incident photon (I_0). Normalization is then obtained as: I/I_0.

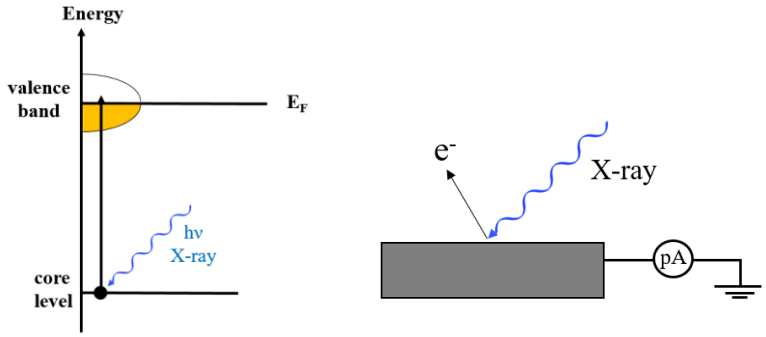

Figure 5.15 (Right) XAS process described by the simply one-electron picture. (Left) XAS TEY detection mode.

5.7.1 XMCD

The XMCD spectrum is described by:

$$XMCD = \sigma_R - \sigma_L \tag{30}$$

where σ_R and σ_L are the cross-section of circularly right (CR) and left (CL) polarised light. An example is illustrated in Figure 5.16.

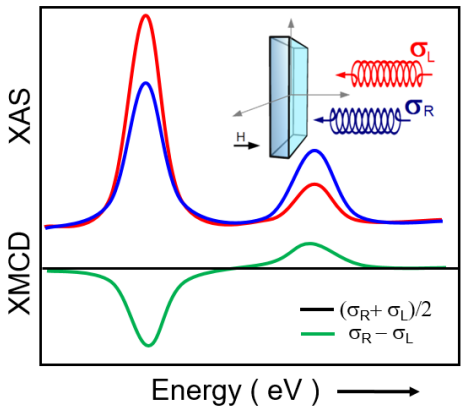

Figure 5.16 XAS (red and blue lines) and XMCD (green) spectra.[11]

To describe the main concepts of the XMCD we consider a transition metal atom whose electronic levels are shown in Figure 5.17. The *2p* shell is complete, while the *d* shell has a spin momentum due to the imbalance of the spin-up and spin-down electrons (states below the Fermi level). In order to probe this imbalance we need the absorption process to be spin-dependent. The circular polarised light is a spin-dependent probe. The CR and CL photons transfer their angular momentum, $+\hbar$ and $-\hbar$ respectively, to the excited photoelectron.

In the system that we consider (Figure 5.17) the excited photoelectron comes from the *2p* level, that is split, due to the spin-orbit coupling, in $2p_{3/2}$ and $2p_{1/2}$. The transfer of the angular momentum from the photon can be done by spin-orbit coupling. CR photons transfer the opposite momentum to the electron from CL photons, and thus photoelectrons with opposite spins are created in the two cases. The $p_{3/2}$ and the $p_{1/2}$ levels have opposite spin-orbit coupling ($l+s$, $l-s$), therefore the spin polarisation would be opposite in the two cases. The spin flip is forbidden in the electric dipole transition that govern the XAS absorption. For this reason, the photoelectron coming from the spin-up *p* core can be excited only on the spin-up *d* excited levels, and analogously for the spin-down. The transition intensity for the two light polarisations would be therefore proportional to the accessible *d* holes for the two polarization. The size of the dichroism scale with $\cos\theta$, where θ is the angle between the magnetic field direction and the photon spin. The maximum of the dichroic effect is when the two vectors are parallel or antiparallel.

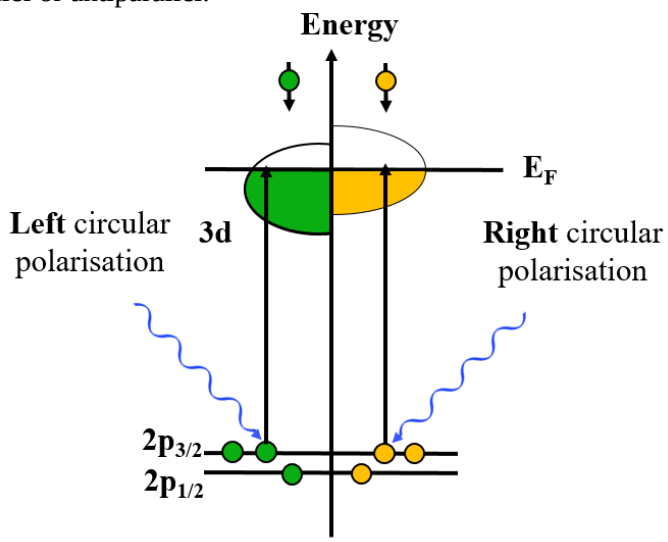

Figure 5.17 Schematic representation of the XMCD process for a transition metal atom with a partially empty d orbital.

5.7.2 XNLD

The XNLD spectrum is obtained by the following difference:

$$XNLD = \sigma_V - \sigma_H \quad (31)$$

where σ_V and $\sigma_H$are the cross-section of vertically and horizontally linearly polarised light. The XNLD characterisation provides useful information on the ordering of the molecular thin films.

The XNLD phenomenon can be explained by the "search for light" effect described by Stohr.[178] For linear polarised X-rays the electric field vector *E* acts like a "search light" for the direction of the maximum and minimum number of empty valence states.

We consider a transition metal atom where the electronic transition involves a *1s→2p* or *2p→3d* excitation. The spatial distribution of the *1s* orbital is symmetric, while the different *p* orbitals have a bilobed symmetry. If we consider a cubic ligand field, the three *p* orbitals are isoenergetic and the sum of the three gives a sphere. The *d* orbitals, that are anisotropic, in cubic ligand field, split in e_g and t_{2g} irreducible representation. The sum of the orbital for each irreducible representation is symmetric (see Figure 5.18). In a cubic symmetry, the X-ray absorption is therefore independent to the *E*-vector orientation relative to the sample, for non-magnetic materials.

However, the individual *p* and *d* orbital are asymmetric in space, thus as the geometry is lowered with respect to cubic, the transition to each *p* and *d* orbital depends on the orientation of the *E*-vector with respect to the system. The *p* orbitals present lobes with the maximum density of charge and nodal planes. The maximum of the XNLD signal would be observed when the *E* vector is along the lobes and the minimum when it is perpendicular.

The photoelectron is therefore ejected along the *E* vector by a spherically symmetric core. The *E* vector "search light", *i.e.* sense the empty valence states, and if there are no available valence state along its direction the transition vanishes.

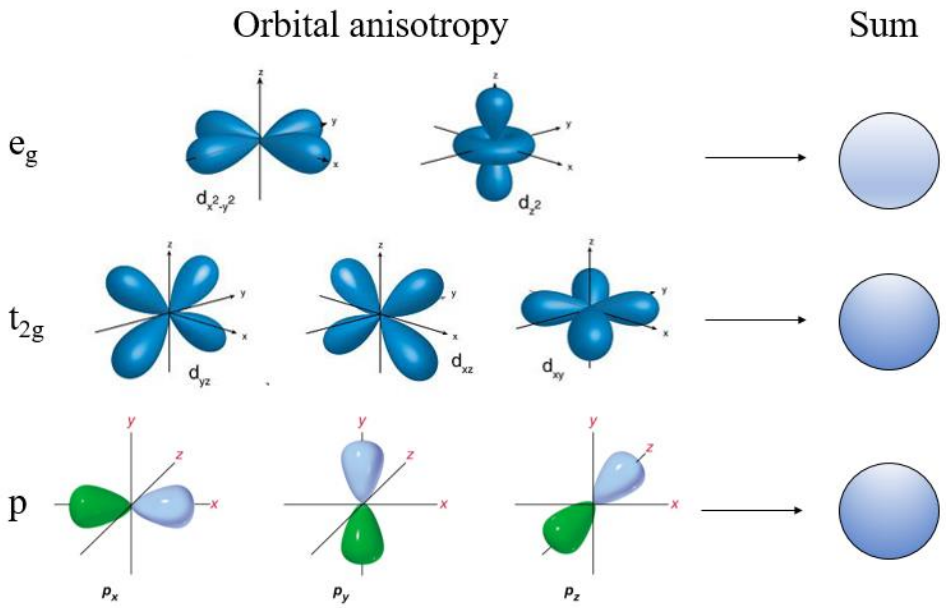

Figure 5.18 Spatial distribution of the orbitals: the individual orbitals are anisotropic, but the sum is spherically symmetric.

5.7.3 Measurements conditions

XMCD signal is proportional to the magnetisation of the specie we are looking at. It is then possible to follow the variation of the XMCD signal while changing different parameters (such as applied field or time), thus performing experiments that are analogue to the standard magnetometric ones.

In order to pick the correct signal, the raw drain current (I) on the sample at the XMCD peak must be normalized against I_0, as already mentioned. In addition to this, a further normalization must be carried out to measure a signal that has physical meaning. So, the peak signal needs to be divided by the signal of the pre-edge (usually 5-10 eV before the edge, but the exact position must be evaluated from each spectrum), thus obtaining:

$$I_{XMCD} = \frac{I_{peak}/I_{0peak}}{I_{preEdge}/I_{0preEdge}} \tag{32}$$

For such experiments the method used by the beamline for polarization switching is a key factor in the quality of the measurement. In standard beamlines, the two polarizations are switched by changing the relative horizontal position of the permanent magnets of the undulators: the typical time scale of this process is around one-two minutes, which is a relatively long time if one thinks it multiplied by the number of points of a normal magnetisation measurement. For this reason, a magnetisation curve based on XMCD signal is typically recorded first with one

polarization by sweeping the field, then with the other polarization at the energy of the XMCD maximum, then the process is repeated for the pre-peak energy; this is the acquisition method we used for our measurements at DEIMOS in Soleil, France.

However when we pass to dynamic experiments, in highly diluted and fast relaxing magnetic systems like monolayers of SMMs, standard polarization switching becomes a limiting factor in the performance of the whole setup. In order to perform a fast switch between the two polarisation, the beamline SIM X11-MA at SLS, Villigen, Switzerland is equipped with two undulators, set to deliver opposite polarizations, that are alternatively tuned and detuned (by moving the gap of about 2 mm). This process takes merely few seconds to change photon helicity on the sample. For each applied field value, both polarizations were acquired in sequence; at the end of the field scan, the same procedure is applied to the pre-edge signal.

In the case of time decay measurements, the signal relative to the two opposite polarizations is recorded alternatively at regular time intervals. For this type of measurement, even more than for hysteresis loops, tune/detune fast polarization switching, coupled to the extreme beam stability at SLS, is a necessary condition for the success of the experiment.

5.8 UHV platform

A big part of the experimental work at the monolayer level described in this thesis has been performed *in situ* exploiting the setup available at the "Centro per le Tecniche di Caratterizzazione a Scansione di Sonda" (CeTeCS). This setup is equipped with several chambers, devoted to sample preparation and characterisation. The preparation of the metallic surfaces has been performed in a dedicated chamber furnished with a heated manipulator, an ion gun and a metal sublimator (surface preparation in Figure 5.19).

Sublimation chamber

The chamber devoted to the sublimation of molecules has a home-made Knudsen-cell illustrated in Figure 5.20. A tantalum wire is rolled on the quartz crucible containing the molecular powder and allows the heating of the powders. A molybdenum foil is inserted into the crucible in order to make the heating homogeneous. A K-thermocouple is welded to the foil to control the temperature. The rate of sublimation is measured by a Sycom quartz microbalance.

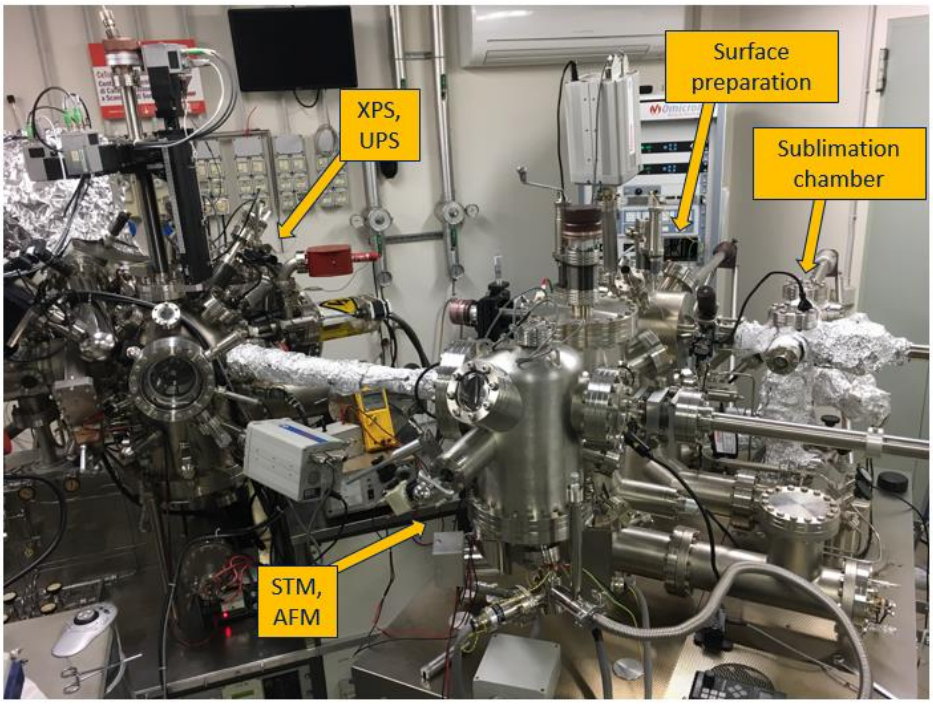

Figure 5.19 The UHV platform for the preparation and characterisation of hybrid materials used in this PhD thesis.

Spectroscopy chamber

The spectroscopy characterisation chamber is equipped with a SPECS Phoibos 150 electron analyser, standard Al and Mg sources, a monochromatic Al X-ray source and a ultra-violet discharge lamp. The sources are assembled at the magic angle (54.44°) with respect to the analyser. The base pressure of the chamber is $< 2 \cdot 10^{-10}$ mbar. At the beginning of my PhD thesis this chamber was equipped with an hemispherical analyser VSW HA100 with a 16-channel detector, where we performed the XPS analysis performed in Section 2.4. and Chapter 3.

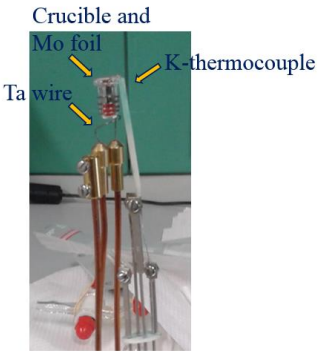

Figure 5.20 Home-made Knudsen cell.

STM chamber

The STM-AFM Omicron variable temperature is in a dedicated chamber with a base pressure < $2 \cdot 10^{-10}$ mbar. The temperature of the sample can vary from 25 K to 1500 K. The STM measurements illustrated in this PhD work are performed at 30 K and W-etched tips are commonly used. The bias potential is applied to the tip and the sample is grounded.

6 Conclusion

This PhD thesis has tackled the challenge of organising magnetic molecules on surfaces by using ultra high vacuum compatible techniques to better control the hybrid interface. This is in fact expected to play a key role in molecule-based devices.

We started our investigation studying the deposition by Organic Molecular Beam Epitaxy of Single Molecule Magnets of the Fe_4 family. The assembling of this class of molecules on surface was previously achieved by wet chemistry approaches, revealing that the magnetic bistability of these molecules is robust enough to be retained on surface. The preliminary available results on the possibility to sublimate these polynuclear metal complexes comprising beta-diketonates ancillary ligands prompted us to perform a detailed investigation of the growth process on surfaces. In particular, though we have been able to demonstrate that intact Fe_4 molecules are present on metallic surfaces we have also evidenced the presence of contaminants. The multi-technique approach that characterises the studies performed in this thesis work has led us to the conclusion that the detected fragments do not originate from a specific surface-induced decomposition but rather from a thermal degradation of the compound. Solutions to eliminate or reduce the amount of fragments on the surface could be based on the development of new Fe_4 derivatives with sublimation temperatures significantly lower than the temperature of degradation or on the use of more demanding deposition protocols based on electro-spray techniques. We have however observed that the presence of fragments is also dependent on the design of the UHV chamber. By employing synchrotron based techniques to measure the X-ray Magnetic Circular Dichroism we have evidenced the persistence of magnetic bistability and quantum tunnelling of the magnetisation also for monolayers of Fe_4 molecules deposited by sublimation. No evidence of contaminants has been detected in the XMCD spectra, which is not surprising as the main contaminant seems to be a low-spin $Fe(dpm)_2$ complex generated on the surface. More importantly no traces of divalent iron have been found in the X-ray absorption spectra, thus suggesting a lower sticking efficiency of the volatile species in the larger deposition chamber and at the higher vacuum available in the end-station.

Another important feature we have investigated by performing *in situ* low temperature STM studies is the molecular packing of Fe_4 molecules on the surface, a topic that has also been investigated theoretically by molecular dynamics by other members of the research group. Replacing the phenyl ring on the tripodal ligand with a shorter $-CH_2-S-CH_3$ residue the volatility has been retained but a more regular packing of the molecules has been obtained, though similar contaminating fragments have been detected. The hexagonal packing in a strict 2D lattice makes this particular system the ideal candidate to investigate the role of dipolar interactions on resonant

tunnelling of the magnetisation. Our results have inspired the theoretical work of Dr. Alessandro Vindigni at ETH, Zürich, who has developed a novel kinetic Monte Carlo approach to reproduce the hysteresis of a finite ensemble of dipolar coupled SMMs.

The unravelled fragility and the inherent low blocking temperature of Fe_4 systems prompted us to search for novel SMM candidates suitable to be assembled on surfaces. In order to exploit the larger magnetic anisotropy of lanthanides, we tested two Dy-based SMMs, a dimer with a bridging pyridine *N*-oxide and a monomer with a long tetrathiofulvalene-based ligand. Both molecules present beta-diketonate ligands that were supposed to promote thermal sublimation. However, slight distortions of the crystalline structures induce an alteration of the magnetic properties when the molecules are sublimated on a substrate. In the case of the Dy-dimer this alteration in tiny thus allowing to maintain the SMM behaviour, while this is completely lost in the Dy-monomer. This led us to the conclusion that also in this case an extra effort to design more rigid molecular structures is required for the thermal sublimation approach. We mention here that we tested also the deposition of the Dy-monomer by self-assembling from solution. The results presented in this thesis evidence that this alternative strategy can be pursued and further developed to transfer to surfaces this promising SMM system, once the decomposition issues revealed in this preliminary study will be overcome.

The research on SMMs and their integration in spintronic devices is still in its infancy and of great relevance for fundamental science, as the low blocking temperatures of these molecules makes them still inadequate for practical applications as memory units. Later, during this PhD thesis, the attention has been expanded to another class of molecules for which temperature requirements are less demanding. These are $S = 1/2$ systems exhibiting long-lived spin coherence that makes them suitable as spin-based quantum bits. The possibility to organise and "entangle" molecular spins has recently suggested their use to realise quantum gates that can be manipulated with microwave frequency radiation. Also in this field there is an increasing interest in single spin control that again goes through the assembling on surfaces.

The first system we have investigated in this frame belongs again to the class of beta-diketonate complexes. The deposition on a gold substrate, its STM and XPS characterisations have flanked a detailed magnetic analysis to form the first comprehensive study to go beyond frozen solution or crystalline molecular spin qubits. The magnetic core of the investigated molecule is the vanadyl moiety, which combines low spin-orbital coupling with an efficient suppression of orbital degeneracy thanks to the short V=O double bond.

The first promising results have prompted us to investigate also another vanadyl derivative: the complex with phthalocyanine. The motivation to move to this class of ligands, already widely investigated in surface science, has been the request to find a system that is more stable face to surface deposition. Moreover, VOPc is expected not to suffer significantly of the strong hybridisation with the surface, as the vanadium

ion lies above the Pc ring and the unpaired electron resides in an orbital that has negligible overlap with those of the ligand or of the substrate. Our long-term goal is in fact that to investigate the spin dynamic of isolated $S = 1/2$ molecules on the surface by employing scanning probe techniques. Recent advances have shown the great potentiality of these techniques, though up to now only on single adatoms on insulating barriers.

During this thesis, we have moved the first steps in this direction thanks to a collaboration with one of the leading groups in low temperature scanning probe techniques. Submonolayer of VOPc molecules have been deposited on gold and graphene grown on silicon carbide. The next step has been the investigation of the spin excitation of these single molecules, in order then to apply a pump and probe technique to detect the life time of the spin state and to investigate the effect of surface confinement. The investigation of the quantum coherence is another more challenging step to afford in the future. The preliminary results obtained by inelastic electron tunnel spectroscopy have revealed a scenario more complicated than expected. First it is important to stress how challenging is the investigation of very low energy excitations as those involving a spin doublet split by the Zeeman energy. The complexity of the graphene substrate, though very promising for its flatness and easy preparation, has probably been underestimated and further studies are necessary to access the spin dynamics of isolated vanadyl complexes. Despite these difficulties, during this thesis, we have successfully posed the basis for further research aimed at tearing down one of the limitation in the use of molecular spin qubits: the lack of an established method to control the spin state of single qubits, which is now possible, though extremely demanding, when using defects in semiconductors such as P atoms implanted in silicon.

7 References

1. Urdampilleta, M., Klyatskaya, S., Cleuziou, J.-P., Ruben, M. & Wernsdorfer, W. Supramolecular spin valves. *Nat. Mater.* **10,** 502–6 (2011).
2. Zyazin, A. S. *et al.* Electric field controlled magnetic anisotropy in a single molecule. *Nano Lett.* **10,** 3307–11 (2010).
3. Kahle, S. *et al.* The quantum magnetism of individual manganese-12-acetate molecular magnets anchored at surfaces. *Nano Lett.* **12,** 518–21 (2012).
4. Katoh, K., Komeda, T. & Yamashita, M. The Frontier of Molecular Spintronics Based on Multiple-Decker Phthalocyaninato Tb III Single-Molecule Magnets. *Chem. Rec.* **16,** 987–1016 (2016).
5. Burzurí, E. *et al.* Franck-Condon blockade in a single-molecule transistor. *Nano Lett.* **14,** 3191–3196 (2014).
6. Bogani, L. & Wernsdorfer, W. Molecular spintronics using single-molecule magnets. *Nat. Mater.* **7,** 179–86 (2008).
7. Leuenberger, M. N. & Loss, D. Quantum computing in molecular magnets. *Nature* **410,** 789–93 (2001).
8. Candini, A., Klyatskaya, S., Ruben, M., Wernsdorfer, W. & Affronte, M. Graphene spintronic devices with molecular nanomagnets. *Nano Lett.* **11,** 2634–9 (2011).
9. Wernsdorfer, W. Molecular Nanomagnets : towards molecular spintronics. *Int. J. Nanotechnol.* **7,** 1–25 (2010).
10. Gatteschi, D., Sessoli, R. & Villain, J. *Molecular Nanomagnets*. *Oxford University Press* (2006).
11. Cornia, A., Mannini, M., Sainctavit, P. & Sessoli, R. Chemical strategies and characterization tools for the organization of single molecule magnets on surfaces. *Chem. Soc. Rev.* **40,** 3076–91 (2011).
12. Mannini, M. *et al.* XAS and XMCD investigation of Mn12 monolayers on gold. *Chem. - A Eur. J.* **14,** 7530–7535 (2008).
13. Voss, S. *et al.* Investigation of the stability of Mn12 single molecule magnets. *Appl. Phys. A Mater. Sci. Process.* **94,** 491–495 (2009).
14. Barra, A. L. *et al.* Single-Molecule Magnet Behavior of a Tetranuclear Iron(III) Complex. The Origin of Slow Magnetic Relaxation in Iron(III) Clusters. *J. Am. Chem. Soc.* **121,** 5302–5310 (1999).
15. Barra, A.-L. *et al.* New Single-Molecule Magnets by Site-Specific Substitution: Incorporation of ‘Alligator Clips’ into Fe4 Complexes. *Eur. J.*

Inorg. Chem. **2007,** 4145–4152 (2007).

16. Mannini, M. *et al.* Quantum tunnelling of the magnetization in a monolayer of oriented single-molecule magnets. *Nature* **468,** 417–21 (2010).

17. Mannini, M. *et al.* Magnetic memory of a single-molecule quantum magnet wired to a gold surface. *Nat. Mater.* **8,** 194–7 (2009).

18. Ishikawa, N., Sugita, M., Ishikawa, T., Koshihara, S. Y. & Kaizu, Y. Lanthanide double-decker complexes functioning as magnets at the single-molecular level. *J. Am. Chem. Soc.* **125,** 8694–8695 (2003).

19. Katoh, K. *et al.* Direct observation of lanthanide(III)-phthalocyanine molecules on Au(111) by using scanning tunneling microscopy and scanning tunneling spectroscopy and thin-film field-effect transistor properties of Tb(III)- and Dy(III)-phthalocyanine molecules. *J. Am. Chem. Soc.* **131,** 9967–76 (2009).

20. Malavolti, L. *et al.* Magnetism of TbPc2 SMMs on ferromagnetic electrodes used in organic spintronics. *Chem. Commun.* **49,** 11506–8 (2013).

21. Margheriti, L. *et al.* X-ray detected magnetic hysteresis of thermally evaporated terbium double-decker oriented films. *Adv. Mater.* **22,** 5488–93 (2010).

22. Schwöbel, J. *et al.* Real-space observation of spin-split molecular orbitals of adsorbed single-molecule magnets. *Nat. Commun.* **3,** 953 (2012).

23. Stepanow, S. *et al.* Spin and orbital magnetic moment anisotropies of monodispersed bis (phthalocyaninato) terbium on a copper surface. *J. Am. Chem. Soc.* **123,** 11900–11901 (2010).

24. Wäckerlin, C. *et al.* Giant Hysteresis of Single-Molecule Magnets Adsorbed on a Nonmagnetic Insulator. *Adv. Mater.* **28,** 5195–5199 (2016).

25. Mannini, M. *et al.* Magnetic behaviour of TbPc2 single-molecule magnets chemically grafted on silicon surface. *Nat. Commun.* **5,** 4582 (2014).

26. Klar, D. *et al.* Hysteretic behaviour in a vacuum deposited submonolayer of single ion magnets. *Dalton Trans.* **43,** 10686–9 (2014).

27. Yi, X. *et al.* A luminescent and sublimable Dy(III)-based single-molecule magnet. *Chem. A Eur. J.* **18,** 11379–87 (2012).

28. Kiefl, E. *et al.* Robust magnetic properties of a sublimable single molecule magnet. *ACS Nano* **10,** 5663–9 (2016).

29. Cunha, T. T. *et al.* Magnetic Poles Determinations and Robustness of Memory Effect upon Solubilization in a DyIII-based Single Ion Magnet. *J. Am. Chem. Soc.* **135,** 16332–16335 (2013).

30. Blatt, R. & Wineland, D. Entangled states of trapped atomic ions. *Nature* **453,** 1008–1015 (2008).

31. Muhonen, J. T. *et al.* Storing quantum information for 30 seconds in a nanoelectronic device. *Nat. Nanotechnol.* **9,** 986–991 (2014).

32. Hanson, R. & Awschalom, D. D. Coherent manipulation of single spins in semiconductors. *Nature* **453,** 1043–1049 (2008).

33. Knill, E., La, R. & Milburn, G. J. A scheme for effcient quantum computation with linear optics. *Nature* **409,** 46–52 (2001).

34. Clarke, J. & Wilhelm, F. K. Superconducting quantum bits. *Nature* **453,** 1031–1042 (2008).

35. Chuang, I. L., K.Vandersypen, L. M., Zhou, X., Leung, D. W. & Lloyd, S. Experimental realization of a quantum algorithm. *Nature* **393,** 143–146 (1998).

36. Thiele, S. *et al.* Electrically driven nuclear spin resonance in single-molecule magnets. *Science* **344,** 1135–1138 (2014).

37. Pla, J. J. *et al.* A single-atom electron spin qubit in silicon. *Nature* **489,** 541–5 (2012).

38. Aromí, G. *et al.* Design of magnetic coordination complexes for quantum computing. *Chem. Soc. Rev.* **41,** 537–546 (2012).

39. Troiani, F. & Affronte, M. Molecular spins for quantum information technologies. *Chem. Soc. Rev.* **40,** 3119–3129 (2011).

40. Balasubramanian, G. *et al.* Ultralong spin coherence time in isotopically engineered diamond. *Nat. Mater.* **8,** 383–7 (2009).

41. Takahashi, S., Hanson, R., Van Tol, J., Sherwin, M. S. & Awschalom, D. D. Quenching spin decoherence in diamond through spin bath polarization. *Phys. Rev. Lett.* **101,** 1–4 (2008).

42. Tyryshkin, A. M. *et al.* Electron spin coherence exceeding seconds in high-purity silicon. *Nat. Mater.* **11,** 143–7 (2012).

43. Accorsi, S. *et al.* Tuning anisotropy barriers in a family of tetrairon (III) single-molecule magnets with an S= 5 ground state. *J. Am. Chem. Soc.* **128,** 4742–4755 (2006).

44. Cornia, A. & Mannini, M. Single-molecule magnets at surfaces. (2014) *in Molecular Nanomagnets and Related Phenomena, Structure and Bonding, Springer Verlag* **164,** 293-330 (2015).

45. Villain, J., Hartmann-Boutron, F., Sessoli, R. & Rettori, A. J. Villain, F. Hartmann-Boutron, R. Sessoli, A. Rettori, Europhys. Lett. 1994, 27, 159-164. *Eur. Lett.* **27,** 159–164 (1994).

46. Gatteschi, D. & Sessoli, R. Quantum Tunneling of Magnetization and Related Phenomena in Molecular Materials. *Angew. Chem. Int. Ed. Engl.* 268–297 (2003).

47. Gregoli, L. *et al.* Magnetostructural correlations in tetrairon(III) single-molecule magnets. *Chem. - A Eur. J.* **15,** 6456–6467 (2009).

48. Vergnani, L. *et al.* Magnetic bistability of isolated giant-spin centers in a diamagnetic crystalline matrix. *Chemistry* **18,** 3390–8 (2012).

49. Weide, H. How a nightmare turns into a vision. *Nat. Mater.* **8106,** 165–166 (2009).

50. Mannini, M. *et al.* XAS and XMCD investigation of Mn12 monolayers on gold. *Chem. A Eur. J.* **14,** 7530–5 (2008).

51. Moro, F. *et al.* Electronic and Magnetic Properties of Mn 12Molecular Magnets on Sulfonate and Carboxylic Acid Prefunctionalized Gold Surfaces. *J. Phys. Chem. C* **116,** 14936–14942 (2012).

52. Margheriti, L. *et al.* Thermal deposition of intact tetrairon(III) single-molecule magnets in high-vacuum conditions. *Small* **5,** 1460–6 (2009).

53. Ninova, S. PhD thesis, University of Florence, Single-Molecule Magnets and surfaces at Density Functional level of theory: a study of their properties before and after adsorption. (2014).

54. Y. Zhang and W. Yang. Comment on 'Generalized gradient approximation made simple'. *Phys. Rev. Lett.* **80,** 890 (1998).

55. Grimme, S., Antony, J., Ehrlich, S. & Krieg, H. A consistent and accurate ab initio parametrization of density functional dispersion correction (DFT-D) for the 94 elements H-Pu. *J. Chem. Phys.* **132,** 154104 (2010).

56. Malavolti, L. *et al.* Magnetic Bistability in a Submonolayer of Sublimated Fe 4 Single Molecule Magnets. *Nano Lett.* **15,** 535–541 (2015).

57. Totaro, P. *et al.* Tetrairon(III) single-molecule magnet monolayers on gold: Insights from ToF-SIMS and isotopic labeling. *Langmuir* **30,** 8645–8649 (2014).

58. Mannini, M. *et al.* Spin structure of surface-supported single-molecule magnets from isomorphous replacement and X-ray magnetic circular dichroism. *Inorg. Chem.* **50,** 2911–7 (2011).

59. Mannini, M. *et al.* X-Ray Magnetic Circular Dichroism Picks out Single-Molecule Magnets Suitable for Nanodevices. *Adv. Mater.* **21,** 167–171 (2009).

60. Friedman, J. R. & Sarachik, M. P. Single-Molecule Nanomagnets. *Annu. Rev. Condens. Matter Phys.* **1,** 109–128 (2010).

61. Thomas, L. *et al.* Macroscopic quantum tunneling of the magnetisation in a single crystal of nanomagnets. *Nature* **383,** 145–147 (2006).

62. Lanzilotto, V. *et al.* The Challenge of Thermal Deposition of Coordination Compounds: Insight into the Case of an Fe 4 Single Molecule Magnet. *Chem. Mater.* **28,** 7693-7702 *Chem. Mater.* (2016).

63. Loth, S., Etzkorn, M., Lutz, C. P., Eigler, D. M. & Heinrich, A. J. Measurement of Fast Electron Atomic Resolution. *Science* **329,** 1628–1630 (2010).

64. Loth, S. *et al.* Controlling the state of quantum spins with electric currents. *Nat. Phys.* **6,** 340–344 (2010).

65. Otte, A. F. *et al.* The role of magnetic anisotropy in the Kondo effect. *Nat. Phys.* **1,** 847–850 (2008).

66. Hirjibehedin, C. F., Lutz, C. P. & Heinrich, A. J. Spin Coupling in Engineered Atomic Structures. *Science* **312,** 1021–1024 (2006).

67. Miyamachi, T. *et al.* Robust spin crossover and memristance across a single molecule. *Nat. Commun.* **3,** 938 (2012).

68. Cimatti, I. *et al.* UHV deposition and characterization of a mononuclear iron(III) β-diketonate complex on Au(111). *Beilstein J. Nanotechnol.* **5,** 2139–2148 (2014).

69. Evans, S., Hamnett, A., Orchard, a. F. & Lloyd, D. R. Study of the metal-oxygen bond in simple tris-chelate complexes by He(I) photoelectron spectroscopy. *Faraday Discuss. Chem. Soc.* **54,** 227–250 (1972).

70. Rebeiro da Silva, M. A. V, Monte, M. J. S. & Huinink, J. Vapour pressures and standard molar enthalpies of sublimation of two crystalline iron (III) beta-diketonates. The mean molar (Fe–O) bond-dissociation enthalpies. **28,** 413–419 (1996).

71. Mulley, J. S., Bennett, R. a. & Dhanak, V. R. Adsorption, orientation and thermal decomposition of copper(II) hexafluoroacetylacetonate on rutile TiO2(110). *Surf. Sci.* **602,** 2967–2974 (2008).

72. Lin, W., Wiegand, B. C., Nuzzo, R. G. & Girolami, G. S. Mechanistic Studies of Palladium Thin Film Growth from Palladium (II) -Diketonates . 1 . Spectroscopic Studies of the Reactions of Bis (hexafluoroacetylacetonato) palladium (II) on Copper Surfaces. *J. Am. Chem. Soc.* **118,** 5977–5987 (1996).

73. Ninova, S. *et al.* Valence Electronic Structure of Sublimated Fe 4 Single-Molecule Magnets: an Experimental and Theoretical Characterization. *J. Mater. Chem. C* **2,** 9599–9608 (2014).

74. Carvallo, C. *et al.* Biogenic vs. abiogenic magnetite nanoparticles: A XMCD study. *Am. Mineral.* **93,** 880–885 (2008).

75. Brice-Profeta, S. *et al.* Magnetic order in γ-Fe2O3 nanoparticles: a XMCD study. *J. Magn. Magn. Mater.* **288,** 354–365 (2005).

76. Erler, P. *et al.* Highly Ordered Surface Self-Assembly of Fe_4 Single Molecule Magnets. *Nano Lett.* **15,** 4546-4552 (2015).

77. Cornia, A. & Parenti, F. Unpublished results (2015).

78. Margheriti, L. PhD thesis, University of Florence, Thermal deposition of

Single Molecule Magnets on metallic and magnetic surfaces. (2010).

79. Malavolti, L. PhD thesis, University of Florence, Single molecule magnets sublimated on conductiong and magnetic substrates. (2014).

80. Cuccoli, A., Fort, A., Rettori, A., Adam, E. & Villain, J. Dipolar interaction and incohernt quantum tunneling: a Monte Carlo study of magnetic relaxation. *Eur. Phys. J. B* **12,** 39–46 (1999).

81. J. J. Alonso & J. F. Fernandez. Tunnel window's imprint on dipolar field distributions. *Phys. Rev. Lett.* **87,** 7205 (2001).

82. Liu, J., Wu, B., Fu, L., Diener, R. B. & Niu, Q. Quantum step heights in hysteresis loops of molecular magnets. *Phys. Rev. B* **65,** 1–6 (2002).

83. Jansen, A. P. J. in *An Introduction to Kinetic Monte Carlo Simulations of Surface Reactions* 37–71 (2012).

84. A.P.J. Jansen. Monte Carlo simulations of chemical reactions on a surface with time-dependent reaction-rate constants. *Comput. Phys. Commun.* **86,** 1–12 (1995).

85. Dreiser, J. *et al.* X-ray induced demagnetization of single-molecule magnets. *Appl. Phys. Lett.* **105,** 32411 (2014).

86. Cimatti, I., Mannini, M., Poggini, L. & Sessoli, R. No Title. *Priv. Commun.*

87. Malavolti, L. *et al.* Erratic magnetic hysteresis of TbPc2 molecular nanomagnets. *J. Mater. Chem. C* **1,** 2935–2942 (2013).

88. Vitali, L. *et al.* Electronic structure of surface-supported bis(phthalocyaninato) terbium(III) single molecular magnets. *Nano Lett.* **8,** 3364–8 (2008).

89. Komeda, T. *et al.* Observation and electric current control of a local spin in a single-molecule magnet. *Nat. Commun.* **2,** 217 (2011).

90. Lodi Rizzini, a. *et al.* Coupling Single Molecule Magnets to Ferromagnetic Substrates. *Phys. Rev. Lett.* **107,** 177205 (2011).

91. Woodruff, D. N., Winpenny, R. E. P. & Layfield, R. A. Lanthanide Single-Molecule Magnets. *Chem. Rev.* **113,** 5110–5148 (2013).

92. Rinehart, J. D., Fang, M., Evans, W. J. & Long, J. R. Strong exchange and magnetic blocking in N_2^{3-}-radical-bridged lanthanide complexes. *Nat. Chem.* **3,** 538–42 (2011).

93. Ishikawa, N., Sugita, M. & Wernsdorfer, W. Quantum tunneling of magnetization in lanthanide single-molecule magnets: bis(phthalocyaninato)terbium and bis(phthalocyaninato)dysprosium anions. *Angew. Chem. Int. Ed. Engl.* **44,** 2931–5 (2005).

94. Demir, S., Jeon, I. R., Long, J. R. & Harris, T. D. Radical ligand-containing single-molecule magnets. *Coord. Chem. Rev.* **289–290,** 149–176 (2015).

95. *Lanthanides and Actinides in Molecular Magnetism*. (2015).

96. Holmberg, R. J. & Murugesu, M. Adhering magnetic molecules to surfaces. *J. Mater. Chem. C* **3,** 11986–11998 (2015).

97. Canevet, D., Sallé, M., Zhang, G., Zhang, D. & Zhu, D. Tetrathiafulvalene (TTF) derivatives: key building-blocks for switchable processes. *Chem. Commun. (Camb).* **7345,** 2245–69 (2009).

98. Mas-Torrent, M. *et al.* Single-crystal organic field-effect transistors based on dibenzo-tetrathiafulvalene. *Appl. Phys. Lett.* **86,** 3–5 (2005).

99. Yi, X. Structural, Magnetic and Photophysical Investigations on Lanthanide-Bases Single-Molecule Magnets. (2014).

100. Shirley, D. A. High-Resolution X-Ray Photoemission Spectrum of the Valence Bands of Gold. *Phys. Rev. B* **5,** 4709–4714 (1972).

101. Barreca, D. *et al.* Nanostructured Dy2O3 films: An XPS Investigation. *Surf. Sci. Spectra* **14,** 52 (2007).

102. Milanov, A. P. *et al.* Malonate complexes of dysprosium: synthesis, characterization and application for LI-MOCVD of dysprosium containing thin films. *Dalton Trans.* **40,** 62–78 (2011).

103. Popovici, D., Czeremuzkin, G., Meunier, M. & Sacher, E. Laser-induced metal-organic chemical vapor deposition (MOCVD) of Cu(hfac)(TMVS) on amorphous Teflon AF1600: an XPS study of the interface. *Appl. Surf. Sci.* **126,** 198–204 (1998).

104. Roodenko, K. *et al.* Time-resolved synchrotron XPS monitoring of irradiation-induced nitrobenzene reduction for chemical lithography. *J. Phys. Chem. B* **111,** 7541–9 (2007).

105. Bag, S., Roy, K., Gopinath, C. S. & Raj, C. R. Facile Single-Step Synthesis of Nitrogen-Doped Reduced Graphene Oxide-Mn 3 O 4 Hybrid Functional Material for the Electrocatalytic Reduction of Oxygen. *ACS Appl. Mater. Interfaces* **6**, 2692−2699 (2014).

106. Lunghi, A. No Title. *Priv. Commun.*

107. Lunghi, A., Totti, F., Sessoli, R. & Sanvito, S. No Title. *Submitt. to Publ.*

108. Long, J. *et al.* Single-Molecule Magnet Behavior for an Antiferromagnetically Superexchange-Coupled Dinuclear Dysprosium (III) Complex. *J. Am. Chem. Soc. 133* 5319–5328 (2011).

109. Layfield, R. A. *et al.* Influence of the N-Bridging Ligand on Magnetic Relaxation in an Organometallic Dysprosium Single-Molecule Magnet. *Chem. A Eur. J.* **16,** 4442–4446 (2010).

110. Colacio, E. *et al.* Slow Magnetic Relaxation in a Co II – Y III Single-Ion Magnet with Positive Axial Zero-Field Splitting. *Angew. Chem. Int. Ed. Engl.* **52,** 9130–9134 (2013).

111. Novikov, V. V *et al.* A Trigonal Prismatic Mononuclear Cobalt(II) Complex

Showing Single-Molecule Magnet Behavior. *J. Am. Chem. Soc.* 9792–9795 (2015).

112. Shriyastava, K. N. Theory of Spin-Lattice Relaxation. *Phys. Stat. Sol.* **437,** 437–458 (1983).

113. Guo, Y. *et al.* Strong Axiality and Ising Exchange Interaction Suppress Zero-Field Tunneling of Magnetization of an Asymmetric Dy 2 Single-Molecule Magnet. *J. Am. Chem. Soc.* **133,** 11948–11951 (2011).

114. Tesi, L. *et al.* Giant spin-phonon bottleneck effects in evaporable vanadyl-based molecules with long spin coherence. *Dalt. Trans.* **45,** 16635–16643 (2016).

115. Cosquer, G., Pointillart, F., Golhen, S., Cador, O. & Ouahab, L. Slow magnetic relaxation in condensed versus dispersed dysprosium(III) mononuclear complexes. *Chem. Eur. J.*. **19,** 7895–7903 (2013).

116. Oeter, D., Ziegler, C. & Gopel, W. Doping and stability of ultrapure alfa-oligothiophene thin films. *Synth. Met.* **61,** 147–150 (1993).

117. Pineider, F. *et al.* Deposition of intact tetrairon(III) single molecule magnet monolayers on gold: an STM, XPS, and ToF-SIMS investigation. *J. Mater. Chem.* **20,** 187–194 (2010).

118. Hamamatsu, T. *et al.* Magnetic Interactions in Cu II − Ln III Cyclic Tetranuclear Complexes : Is It Possible to Explain the Occurrence of SMM Behavior in Cu II − Tb III and Cu II − Dy III Complexes. *Inorg. Chem.* **46,** 4458–4468 (2007).

119. Westerstrom, R. *et al.* An Endohedral SMM with long Relaxation Times:DySc2N@C80. *J. Am. Chem. Soc.* **134,** 9840–9843 (2012).

120. Tyryshkin, A. M. *et al.* Electron spin coherence exceeding seconds in high purity silicon. *Nat. Mater.* **11,** 18 (2011).

121. Wernsdorfer, W., Aliaga-Alcalde, N., Hendrickson, D. N. & Christou, G. Exchange-biased quantum tunnelling in a supramolecular dimer of single-molecule magnets. *Nature* **416,** 406–9 (2002).

122. Hill, S., Edwards, R. S., Aliaga-Alcalde, N. & Christou, G. Quantum Coherence in an Exchange-Coupled Dimer of Single- Molecule Magnets. *Science* **302,** 1015–1018 (2003).

123. Hill, S., Edwards, R. S., Aliaga-Alcalde, N. & Christou, G. Quantum Coherence in an Exchange-Coupled Dimer of Single- Molecule Magnets. *Science* **302,** 1015–1018 (2003).

124. Troiani, F. *et al.* Molecular Engineering of Antiferromagnetic Rings for Quantum Computation. *Phys. Rev. Lett.* **94,** 207208 (2005).

125. Affronte, M. *et al.* Single molecule magnets for quantum computation. *J. Phys. D. Appl. Phys.* **40,** 2999–3004 (2007).

126. Ardavan, A. *et al.* Will spin-relaxation times in molecular magnets permit quantum information processing? *Phys. Rev. Lett.* **98,** 1–4 (2007).

127. Wedge, C. J. *et al.* Chemical engineering of molecular qubits. *Phys. Rev. Lett.* **108,** 1–5 (2012).

128. Timco, G. a. *et al.* Engineering the coupling between molecular spin qubits by coordination chemistry. *Nat. Nanotechnol.* **4,** 173–178 (2009).

129. Aromí, G., Aguilà, D., Gamez, P., Luis, F. & Roubeau, O. Design of magnetic coordination complexes for quantum computing. *Chem. Soc. Rev.* **41,** 537 (2012).

130. Timco, G. A., McInnes, E. J. L., Pritchard, R. G., Tuna, F. & Winpenny, R. E. P. Heterometallic rings made from chromium stick together easily. *Angew. Chemie - Int. Ed.* **47,** 9681–9684 (2008).

131. Corradini, V. *et al.* Successful grafting of isolated molecular Cr7 Ni rings on Au(111) surface. *Phys. Rev. B* **79,** 1–8 (2009).

132. Collauto, A. *et al.* A slow relaxing species for molecular spin devices: EPR characterization of static and dynamic magnetic properties of a nitronyl nitroxide radical. *J. Mater. Chem.* **22,** 22272–22281 (2012).

133. Warner, M. *et al.* Potential for spin-based information processing in a thin-film molecular semiconductor. *Nature* **503,** 504–508 (2013).

134. Zadrozny, J. M., Niklas, J., Poluektov, O. G. & Freedman, D. E. Multiple Quantum Coherences from Hyper fi ne Transitions in a Vanadium(IV) Complex. *J. Am. Chem. Soc.* **136,** 15841–15844 (2014).

135. Bader, K. *et al.* Room temperature quantum coherence in a potential molecular qubit. *Nat. Commun.* **5,** 5304 (2014).

136. Zadrozny, J. M., Niklas, J., Poluektov, O. G. & Freedman, D. E. Millisecond Coherence Time in a Tunable Molecular Electronic Spin Qubit. *ACS Cent. Sci.* **1,** (2015).

137. Klofta, T. J. *et al.* Photoelectrochemical and spectroscopic characterization of thin films of titanyl phthalocyanine: comparisons with vanadyl phthalocyanine. *J. Phys. Chem.* **91,** 5646–5651 (1987).

138. Johnson, D. a. & Waugh, a. B. Vapour phase chemistry of oxovanadium iv β-diketonates. *Polyhedron* **2,** 1323–1328 (1983).

139. Maurya, M. R. Development of the coordination chemistry of vanadium through bis(acetylacetonato)oxovanadium(IV): Synthesis, reactivity and structural aspects. *Coord. Chem. Rev.* **237,** 163–181 (2003).

140. Tesi, L. *et al.* Quantum Coherence in a processable vanadyl complex: new tools for the search of molecular spin qubits. *Chem. Sci.* **7,** 2074–2083 (2016).

141. Biesinger, M. C. *et al.* Resolving surface chemical states in XPS analysis of first row transition metals, oxides and hydroxides: Sc, Ti, Cu and Zn. *Appl.*

Surf. Sci. **257,** 887–898 (2010).

142. Eguchi, K., Nakagawa, T., Takagi, Y. & Yokoyama, T. Direct Synthesis of Vanadium Phthalocyanine and Its Electronic and Magnetic States in Monolayers and Multilayers on Ag(111). *J. Phys. Chem. C* **119,** 9805–9815 (2015).

143. Eguchi, K., Takagi, Y., Nakagawa, T. & Yokoyama, T. Molecular orientation and electronic states of vanadyl phthalocyanine on Si(111) and Ag(111) surfaces. *J. Phys. Chem. C* **117,** 22843–22851 (2013).

144. Stepanow, S. *et al.* Giant spin and orbital moment anisotropies of a Cu-phthalocyanine monolayer. *Phys. Rev. B* **82,** 1–8 (2010).

145. Zhang, Y. *et al.* Electronic structure of the organic semiconductor vanadyl phthalocyanine (VO-Pc). *J. Mater. Chem.* **17,** 1276 (2007).

146. Atzori, M. *et al.* Room-Temperature Quantum Coherence and Rabi Oscillations in Vanadyl Phthalocyanine: Toward Multifunctional Molecular Spin Qubits. *J. Am. Chem. Soc.* **138,** 2154–2157 (2016).

147. Donati, F. *et al.* Magnetic remanence in single atoms. *Science* **352,** 318–321 (2016).

148. Loth, S. *et al.* Controlling the state of quantum spins with electric currents. *Nat. Phys.* **6,** 340–344 (2010).

149. Loth, S., Etzkorn, M., Lutz, C. P., Eigler, D. M. & Heinrich, A. J. Measurement of fast electron spin relaxation times with atomic resolution. *Science* **329,** 1628–30 (2010).

150. Heinrich, B. W., Braun, L., Pascual, J. I. & Franke, K. J. Protection of excited spin states by a superconducting energy gap. *Nat. Phys.* **9,** 765–768 (2013).

151. Loth, S., Etzkorn, M., Lutz, C. P., Eigler, D. M. & Heinrich, A. J. Measurement of fast electron spin relaxation times with atomic resolution. *Science* **329,** 1628–30 (2010).

152. Yoshida, S. *et al.* Probing ultrafast spin dynamics with optical pump – probe scanning tunnelling microscopy. *Nat. Nanotechnol.* **9,** 588–593 (2014).

153. Baumann, S. *et al.* Electron Spin Resonance of Individual Atoms on a Surface. *Science* **350,** 417–420 Science (2015).

154. Ziolo, R. F., Griffiths, C. H. & Troup, J. M. Crystal structure of vanadyl phthalocyanine, phase II. *J. Chem. Soc. Dalt. Trans.* **575,** 2300 (1980).

155. Adler, H. *et al.* Interface Properties of VOPc on Ni(111) and Graphene/Ni(111): Orientation Dependent Charge Transfer. *J. Phys. Chem. C* **119,** 8755–8762 (2015).

156. Niu, T., Zhang, J. & Chen, W. Molecular ordering and dipole alignment of vanadyl phthalocyanine monolayer on metals: The effects of interfacial interactions. *J. Phys. Chem. C* **118,** 4151–4159 (2014).

157. Zhang, J., Wang, Z., Niu, T., Li, Z. & Chen, W. Single molecule tunneling spectroscopy investigation of reversibly switched dipolar vanadyl phthalocyanine on graphite. *Appl. Phys. Lett.* **104,** (2014).

158. Ouerghi, A. *et al.* Large-Area and High-Quality Epitaxial Graphene on O ff -Axis SiC Wafers. *ACS Nano* **6** 6075–6082 (2012).

159. Lalmi, B. *et al.* Flower-shaped domains and wrinkles in trilayer epitaxial graphene on silicon carbide. *Sci. Rep.* **4,** 4066 (2014).

160. Velez-Fort, E. *et al.* Epitaxial Graphene on 4H-SiC (0001) Grown under Nitrogen Flux : Evidence of Low Nitrogen Doping and High. *ACS Nano* **6,** 10893–10900 (2012).

161. Lalmi, B. *et al.* Flower-shaped domains and wrinkles in trilayer epitaxial graphene on silicon carbide. *Sci. Rep.* **4,** 4066 (2014).

162. Heinrich, A. J. Single-Atom Spin-Flip Spectroscopy. *Science* **306,** 466–469 (2004).

163. Hirjibehedin, C. F. *et al.* Large Magnetic Anisotropy of a Single Atomic Spin Embedded in a Surface Molecular Network. *Science* **317,** 1199–1203 (2007).

164. Burgess, J. A. J. *et al.* Magnetic fingerprint of individual Fe4 molecular magnets under compression by a scanning tunnelling microscope. *Nat. Commun.* **6,** 8216 (2015).

165. Loth, S., Lutz, C. P. & Heinrich, A. J. Spin-polarized spin excitation spectroscopy. *New J. Phys.* **12,** (2010).

166. Miller, D. L. *et al.* Observing the Quantization of Zero Mass Carriers in Graphene. *Science* **324,** 924–927 (2009).

167. Casimir, H. B. J. & Du Pré, F. K. *Physica V*. (1938).

168. Cole, K. S. & H., C. R. Dispersion and Absorption in Dielectrics I. Alternating Current Characteristics. *J. Chem. Phys* **9,** 341 (1941).

169. Einstein, A. NoÜber einen die Erzeugung und Verwandlung des Lichtes betreffenden heuristischen Gesichtspunkt. *Ann. Phys.* **17,** 132–148 (1905).

170. Yeh, J. J. *Atomic Calculation of Photoionization Cross-Sections and Asymmetry Parameters*. (1993).

171. Yeh, J. J. & Lindau, I. Atomic subshell photoionization cross sections and asymmetry parameters: $1 \leqslant Z \leqslant 103$. *At. Data Nucl. Data Tables* **32,** 1–155 (1985).

172. Bardeen, J. Tunneling from a many-particle point of view. *Phys. Rev. Lett.* **6,** 57–59 (1961).

173. Tersoff, J. & Hamann, D. Theory of the scanning tunneling microscope. *Phys. Rev. B* **31,** 805–813 (1985).

174. Tersoff, J. & Hamann, D. Theory and Application for the Scanning Tunneling

Microscope. *Phys. Rev. Lett.* **50,** 1998–2001 (1983).

175. Letard, I. *et al.* Remnant magnetization of Fe8 high-spin molecules: X-ray magnetic circular dichroism at 300 mK. *J. Appl. Phys.* **101,** (2007).

176. Sainctavit, P. & Kappler, J. in *Magnetism and Synchrotron Radiation Proceedings, Mittelwihr 2000* 235–253 (2001).

177. Nakajima, R., Stöhr, J. & Idzerda, Y. Electron-yield saturation effects in L-edge x-ray magnetic circular dichroism spectra of Fe, Co, and Ni. *Phys. Rev. B* **59,** 6421–6429 (1999).

178. Stohr, J. & Siegmann, H. C. *Magnetism From Fundamentals to Nanoscale Dynamics*. (2006).

Publications list

UHV deposition and characterization of a mononuclear iron(III) β-diketonate complex on Au(111)
I. Cimatti, S. Ninova, V. Lanzilotto, L. Malavolti, L. Rigamonti, B. Cortigiani, M. Mannini, E. Magnano, F. Bondino, F. Totti, A. Cornia and R. Sessoli *Beilstein J Nanotechnol.*, **2014**, *5*, 2139-48.

Magnetic Bistability in a Submonolayer of Sublimated Fe_4 Single Molecule Magnets
L. Malavolti, V. Lanzilotto, S. Ninova, L. Poggini, I. Cimatti, B. Cortigiani, L. Margheriti, D. Chiappe, E. Otero, P. Sainctavit, F. Totti, A. Cornia, M. Mannini and R. Sessoli. *Nano Lett.*, **2015,** *15* (1), 535–541.

Quantum Coherence in a processable vanadyl complex: new tools for the search of molecular spin qubits
L. Tesi, E. Lucaccini, I. Cimatti, M. Perfetti, M. Mannini, E. Morra, M. Chiesa, A. Caneschi, L. Sorace, R. Sessoli *Chem. Sci*, .**2016**, *7*, 2074-2083.

The Challenge of Thermal Deposition of Coordination Compounds: Insight into the Case of an Fe_4 Single Molecule Magnet
V. Lanzilotto, L. Malavolti, S. Ninova, I. Cimatti, L. Poggini, B. Cortigiani, M. Mannini, F. Totti, A. Cornia, R. Sessoli *Chem. Mat.*, **2016,** *28*, 7693-7702.

Ringraziamenti

Tante persone sono da ringraziare per aver reso possibile questo dottorato. Innanzitutto la Prof. Roberta Sessoli che con il suo entusiasmo e la sua competenza mi ha guidato in questi ultimi tre anni. Ringrazio il Dr. Matteo Mannini, fonte inesauribile di idee e esempio di perseveranza.

Ringrazio il Dr. Kevin Bernot per la sintesi di diversi Single Molecule Magnet che ho studiato nel corso della mia tesi, per la pazienza e la precisione nel rispondere alle mie domande e per aver letto questo scritto. Ringrazio il Prof. Andrea Cornia e i suoi collaboratori per la sintesi del Fe_4 che ho utilizzato durante la mia tesi e il Dr. Fabrice Pointillart per avermi fornito interessanti SMM. Voglio ringraziare la Prof.ssa Agnese Magnani che mi ha permesso di effettuare le misure ToF-SIMS. Ringrazio il Dr. Alessandro Vindigni che ha effettuato i calcoli del contributo dipolare nel rilassamento del Fe_4. Ringrazio il Prof. Guido Condorelli per aver accettato di leggere questa tesi.

I want to thank Dr. Sebastian Loth who gave me the possibility to pass two months in his lab and all the members of his group for their hospitality.

Je veux remercier Prof. Philippe Sainctavit, Dr. Edwige Otero et Dr. Loic Joly qui m'ont beaucoup appris sur le XAS, le synchrotron et la TBT et avec lesquelles on a partagé plusieurs plaisent week-end en Suisse.

Ringrazio Federico e Silviya per il fruttuoso ma complicato confronto tra teoria e esperimento. Ringrazio i superficiali con cui ho condiviso lunghe giornate, in primis Brunetto, senza il quale il CeTeCS non sarebbe tale, Poggio e Gigi che hanno pazientemente risposto alle mie domande più o meno filosofiche in tutto il corso della mia tesi, anche da lontano, Mr. Serri, Valeria e Giulia, l'ultima arrivata. Ringrazio tutti i Lammers passati e presenti: Manne, Beppe, Michele, Eva, Alessandro, Guglielmo, Lorenzo etc..

Un ringraziamento particolare va alla mia famiglia che mi ha sempre supportato in tutte le mie scelte e in particolare a Marco che, oltre a supportarmi, mi ha anche sopportato in tutto il periodo (di scrittura) della tesi.